TECHNISCHE UNIVERSITÄT WIEN
Vienna University of Technology

PhD Thesis

Fatigue investigations of metallic biomaterials based on Ti-Nb and Co-Cr

accomplished to attend the academic degree of a doctor

under the supervisions of

Dr.techn. Golta Khatibi

Ao. Univ. Prof. i.R. Dr. Michael Zehetbauer

Univ.Prof. Dipl.-Ing. Dr.techn. Dr.h.c.mult. Herbert Danninger

at the Institute of Chemical Technologies and Analytics,

Vienna University of Technology,

Faculty of Technical Chemistry

by

MSc. Mitra Delshadmanesh

Matr.-Nr. e1148726

Getreidemarkt 9/E164

A-1060 Wien

Vienna, November 2018

Zusammenfassung

Hochfeste metallische, biocompatible Werkstoffe werden häufig für die Herstellung von Implantaten verwendet. Die mechanische Ermüdung wurde bei gewichtsbelasteten Implantaten als klinische Hauptausfallsursache ermittelt. Die biokompatiblen β-Phase Ti-45Nb (Gew.-%)-Legierungen, mit einem niedrigen Elastizitätsmodul von etwa 65 GPa, wurden als geeigneter Kandidat, für den Einsatz in tragenden Implantaten unter Ermüdungsbedingungen, orgeschlagen. Im Rahmen dieser Arbeit wurde der Einfluss der Mikrostruktur auf die mechanischen Eigenschaften und das Ermüdungsverhalten der Ti-45Nb-Legierung bei hohen Lastspielzahlen untersucht. Ermüdungsuntersuchungen wurden mittels eines Ultraschall-Resonanz-Prüfstands bei 20 kHz durchgeführt. Eine starke plastische Verformung wurde mit Hilfe der Hochdruck-Torsionstechnik (HPT) aufgebracht, um eine ultrafeinkörnige (UFG) Ti-45Nb-Legierung mit verbesserten mechanischen Eigenschaften zu erhalten, ohne den E-Modul zu erhöhen. Aufgrund der begrenzten Größe der HPT-verarbeiteten Proben wurden Zug- und Ermüdungsversuche am UFG und dem anfänglich konventionell körnigen (CG) Material mit kleinskaligen Proben und speziell adaptiertem Versuchsaufbau durchgeführt. Zur Berechnung der Spannungs- und Dehnungsbedingungen in den miniaturisierten, dynamisch beanspruchten Proben wurden Finite-Elemente-Simulationen durchgeführt. Die Kornverfeinerung führte zu einer mechanisch stabilen Struktur mit einer erheblichen Verbesserung der Zugeigenschaften, wobei jedoch eine signifikante Verbesserung der Ermüdungsfestigkeit bei hohen Lastwechselzahlen im Vergleich zur CG-Legierung nicht beobachtet werden konnte. Um dieses Verhalten zu erklären, wurden die Veränderungen der Nanohärte, Subkorngröße und Versetzungsdichte des UFG-Materials vor und nach der SPD-Verarbeitung bewertet und diskutiert. TEM-Untersuchungen bestätigten, dass die Kornvergröberung bis zu den sehr hohen Zyklenzahlen nicht stattgefunden hat. Jedoch deutete die graduelle Verringerung der Härte und Versetzungsdichte im Bereich von 1e6 bis 1e9 Zyklen auf eine zyklische Entfestigung des UFG Ti45Nb-Materials hin. Mikrostrukturuntersuchungen und Bruchflächenanalysen wurden durchgeführt, um Informationen über die Mechanismen der Materialermüdung im Bereich der hohen Zyklen zu erhalten. Zusätzlich zu den kleinskaligen Proben, wurde der Einfluss der Kerbengeometrie auf das Ermüdungsverhalten der Ti-45Nb-Legierung an Großproben (Bulk) mit unterschiedlichen Umfangskerben untersucht. Die

experimentellen Ergebnisse bei den Bulk-Proben der Ti-45Nb-Legierung zeigten eine Abnahme der Empfindlichkeit der Ermüdungskerbe bei abnehmendem Kerbenradius. Die Finite-Elemente-Analyse (FEA) wurde zur Berechnung der Spannungsverteilung in den Bulkproben und zur Interpretation der experimentellen Ergebnisse durchgeführt. Darüber hinaus zeigte sich bei der Lebensdauer der Legierung eine starke Abhängigkeit von der Lage der Defekte und mikrostrukturellen Inhomogenitäten. Es wurde beobachtet, dass bei gleicher pannungsamplitude ein frühzeitiges Versagen durch Oberflächenfehler verursacht wurde, während solche mit einer längeren Lebensdauer aufgrund von Rissen, die durch innere Fehler verursacht wurden, versagten. Um die erhaltenen Ergebnisse der Bulk-Ti-45Nb-Proben mit einem konventionell eingesetzten metallischen Biomaterial zu vergleichen, wurden zusätzlich auch Ermüdungstests an glatten und gekerbten Bulk-Proben aus der hochfesten Co-Cr-Legierung L605 durchgeführt. Die Auswirkungen der Oberflächeneigenschaften auf die Rissausbreitung und die Ermüdungslebensdauer der Co-Cr-Legierung L605 wurden unter Verwendung von mechanischen (MP) und elektropolierten (EP) Proben untersucht. Die Ergebnisse zeigten, dass elektropolierte, glatte L605-Proben eine geringere Dauerfestigkeit aufweisen als ihre mechanisch polierten Gegenstücke. Basierend auf den bisherigen Studien wurde dieses Verhalten mit dem positiven Einfluss von Eigenspannungen auf das Ermüdungsverhalten metallischer Werkstoffe in Verbindung gebracht. Typische Ermüdungsbruchflächen der grobkörnigen L605-Proben zeigten, dass, unabhängig von der Spannungsamplitude und der Anzahl der Lastwechsel, beinahe alle Brüche initiiert wurden aufgrund des Vorhandenseins von groben Körnern oder einer Ansammlung von kleinen, benachbarten Körnern mit weicher Orientierung auf oder nahe der Oberfläche. Die Untersuchung der Lebensdauer von gekerbten Proben ergab, dass L605-Legierungen im Vergleich zu Ti45Nb-Legierungen, weniger kerbsensitive Materialien sind.

Abstract

High strength metallic biomaterials are commonly used for fabrication of surgical implants. Mechanical fatigue has been recognized as one of the main causes of clinical failure in load-bearing implants. Biocompatible β-phase Ti-45Nb (wt.%) alloy with a low elastic modulus of about 65 GPa has been proposed as a suitable candidate for use in load bearing implants under fatigue conditions. In this work the influence of grain size on the mechanical properties and high cycle fatigue response of Ti-45Nb alloy has been studied. High cycle fatigue experiments were conducted by using an ultrasonic resonance testing system operating at 20 kHz. Severe plastic deformation was applied by using the high pressure torsion (HPT) technique in order to obtain an ultrafine grained (UFG) Ti-45Nb alloy with enhanced mechanical properties without increasing the elastic modulus. Due to limited size of the HPT processed samples, tensile and fatigue tests on the UFG and the initial conventional grained (CG) material were performed using small-scaled specimens and specially adapted testing set-ups. Finite element simulations were conducted for calculation of the stress and strain conditions in the miniaturized samples subjected to dynamic loading. Grain refinement resulted in a mechanically stable structure with a considerable improvement of the tensile properties. However, a significant improvement of the high cycle fatigue performance in comparison with the CG alloy was not observed. In order to explain this behavior, the changes in the nanohardness, subgrain size and dislocation density of the UFG material before and after SPD processing were evaluated and discussed. While absence of grain coarsening up to the very high cycle regime was confirmed by TEM investigations, the gradual reduction of hardness and dislocation density with increasing the loading cycles up to 1e9 cycles indicated a cyclic softening of the UFG Ti45Nb material. Microstructural investigations and fracture surface analyses were performed to gain information about the mechanisms of fatigue of the material in the high cycle regime. In addition to the small-scaled specimens, the effect of notch geometry on the fatigue response of Ti-45Nb alloy was studied on bulk samples with different circumferential grooves. The experimental results concerning the bulk samples of Ti-45Nb alloy showed a decrease of fatigue notch sensitivity with decreasing

notch radius. Finite element analysis (FEA) was conducted for calculation of the stress distribution in the bulk samples and interpretation of the experimental results. Further, the lifetime of the alloy showed a strong dependency on the location of the defects and microstructural inhomogeneities. It was observed that at the same stress amplitude, early failure was caused by surface defects, while those with a longer lifetime failed due to cracks originating from internal flaws. In order to compare the high cycle fatigue behaviour of Ti45Nb alloy with a conventionally used biomaterial, additional experiments were performed on bulk samples of Co-Cr alloy L605 high strength material. The effects of surface finish characteristics and notches on the fatigue life of Co-Cr alloy L605 was also studied. The results revealed a lower fatigue strength for the electropolished smooth L605 specimens in comparison with their mechanically polished counterparts. Based on the previous studies, this behaviour was related to the positive effect of residual stresses on the fatigue response of metallic materials. Typical fatigue fracture surfaces of the bulk coarse grained L605 specimens showed that independent of the stress amplitude and the number of loading cycles almost all the cracks were initiated at or near the surface due to the existence of large grains or a number of smaller neighbouring grains with a soft orientation. Furthermore, the notch sensitivity of the L605 materials was found to be lower than that of Ti45Nb alloy.

Contents

To

the soul of my dear father. Today I feel your absence more than ever,
I wished to see your joyful face on this day. Rest in Peace
my compassionate and kind mother
my dear, supportive and encouraging husband
my son, endless enthusiasm of my life.

تقدیم به روح آسمانی پدر عزیزم،

امروز نبودنت را بیشتر از همیشه احساس می کنم، دیدن چهره غرق در شادی ات در این روز آرزویم بود. روحت شاد و یادت گرامی

تقدیم به مادر دلسوز و مهربانم

تقدیم به همسر عزیزم، حامی و مشوق همیشگی ام

تقدیم به پسرم، شور و شوق بی پایان زندگی ام.

Chapter 1: Introduction

Biocompatible metallic alloys are broadly used for fabrication of medical implants. The basic requirements for their applications are high mechanical strength, long-term reliability and corrosion resistance. The frequently used alloys include e.g. austenitic stainless steels, cobalt-chromium based alloys, and titanium and its alloys. In most application fields the surgical implants which commonly display complex structures with different geometries and sizes are subjected to severe fatigue loading. As an example, cardiovascular stents which are composed of a tubular lattice structure of thin struts with thickness in the range of 100 µm should endure 4e8 loading cycles without failure under radial cyclic loading conditions. The endurance limit of surgical implants is currently determined by using the final products and is conducted in the frame of extensive long-term bench tests according to the respective standards (e.g. fatigue test conditions according to ASTM E466 standard requirements). Considering the high requirements for the market release, detailed knowledge of the high cycle fatigue properties of the implant materials and their susceptibility to crack initiation and propagation with respect to the size and geometrical effects is a prerequisite for optimization of these high-quality products during the stages of design and fabrication.

In the present PhD thesis, mechanical properties, deformation behavior and high cycle fatigue response of two types of metallic implant materials were investigated. The materials used for this study include conventional and ultrafine grained Ti-45%Nb alloy, a high strength alloy with a low Young's Modulus, which has been recently proposed for bone implant applications, and high strength Co-Cr-based (L-605) alloy used for cardiovascular stents with thin struts. The focus was to study the influence of microstructure, specimen size and geometry on the lifetime and crack growth behaviour of these biocompatible alloys. Small sized nanostructured fatigue samples of βTi-45Nb alloy were prepared by means of high pressure torsion at WG Physics of Nanostructured Materials at the University of Vienna. The fatigue response of the nanostructured alloy was compared with the conventional grained alloy at the same size scale as well as with bulk samples.

Fatigue samples of L605 Co-Cr alloy were prepared by mechanical polishing (MP) and electropolishing (EP), in order to investigate the effects of surface finish characteristics, crack propagation and the fatigue life. In addition to the smooth samples, circumferential notches were introduced in the midsection of the samples to investigate the influence of notches on the lifetime of L605 Co-Cr alloy and Ti45Nb alloy.

Mechanical properties were investigated by tensile experiments, microhardness and nanoindentation measurements. Fatigue response in the range of 1E+05 to 1E+09 loading cycles (very high cycle regime) was studied by using an ultrasonic resonance fatigue testing system working at 20 kHz. Microstructural characterization was conducted by means of optical microscopy (OM) and electron microscopy techniques (SEM-EBSD, TEM, etc.). For a better understanding and interpretation of the fatigue response, surface damage, crack path morphology and microstructural evolution of the fatigued specimens were examined. All these works were done by the advisory help of Dr. Golta Khatibi. Additionally, Finite Element Method (FEM) simulation was conducted by Dr. Martin Lederer for interpretation of the experimental results and establishment of lifetime prediction curves.

To achieve the aims of the thesis, the present study has been divided into eight chapters. After the introduction in Chapter **1**, a brief overview concerning the fatigue characteristics of titanium based alloys and L605 Co-Cr alloys is given in Chapter **2**. Chapter **3** concerns the fundamentals of the cyclic mechanical properties of metallic materials. In chapter **4** the principals of ultrafine grained and nanostructured materials are presented. The next chapter, **5**, covers used materials and describes the experimental details and methods. Chapter **6** is a presentation and discussion of the obtained results including published experimental data of the papers related to the miniaturized and bulk Ti-45Nb samples and unpublished experimental data concerning the L605 Co-Cr samples. The last chapter, **7**, presents a detailed summary of all the obtained results, conclusions and an outlook comprising some remarks for future research. Parts of the chapters 5,6 and 7 have been already published under the titles; Influence of microstructure on fatigue of biocompatible β-phase Ti-45Nb [1] and Influence of Defects on High Cycle Fatigue Response of Ti45Nb Biocompatible Alloy [2].

Chapter 2: Biocompatible metallic materials

The following chapter gives an overview concerning the fatigue characteristics of titanium based alloys and L605 Co-Cr alloy used for biomedical applications. The definition of biomaterial used in vivo to interact with biological systems was suggested by the National Institutes of Health Consensus Development Conference as following:

‘‘any substance (other than a drug) or combination of substances, synthetic or natural in origin, which can be used for any period of time, as a whole or as a part of a system which treats, augments, or replaces any tissue, organ, or function of the body’’ [3].

Metals are used as biomedical materials because of their excellent mechanical properties, such as strength and resistance to fracture (fatigue durability) and biocompatibility which are of great importance and crucial for the medical applications requiring load bearing. Metallic biomaterials are mainly used for replacing failed hard tissue such as artificial hip joints, bone plates and screws, knee prostheses, fracture fixation wires, pins, spinal instruments, parts of artificial heart valves, vascular stents, and dental implants being under severe cyclic loading conditions. Noble metals, such as gold, silver, palladium and platinum, which possess excellent corrosion resistant, are not suitable for most load-bearing applications (orthopaedic utilization) due to their insufficient strength, high density, high flexibility and their considerable expense. Therefore, noble metals are only used in dental applications such as fillings, or for flexible non-load-bearing applications [4], [5]. The main metallic biomaterials which are titanium alloys, stainless steels and cobalt-chromium (Co-Cr) alloys with biomechanical and biochemical compatibility are used for fabrication of a large variety of medical implants [6]–[8]. Vanadium steel was the first structural metal applied in orthopedic implants, such as bone plates and screws. Nowadays, 316L stainless steel is used due to its superior corrosion resistance to vanadium steel, which is just appropriate for temporary fracture fixation devices, due to its relatively high modulus which can cause bone resorption and loss of bone density in the vicinity of implant leading to implant loosening in the long period of time [5]. The most common alloys used in permanent stenting applications are 316L stainless steel, nitinol (NiTi), and cobalt chromium molybdenum (Co-Cr-Mo) alloys. Nitinol is a particularly attractive alloy for the applications of expanding blood vessels (vascular stents) due to its unusual mechanical properties including superelasticity and shape memory effects.

Commonly, expansion of the conventional stents is done by balloon angioplasty (balloon expandable), whereas nitinol stents are self-expanding, due to their shape memory properties [9]. After exposing nitinol stents to higher temperature in the human body, phase transformation from martensite to austenite occurs, in other words, they return to their original shape in the fully expanded form [10]. However, the long-term contact of nickel with human body has adverse effects (such as allergic reactions) [11]. Other biomaterials such as magnesium (Mg), tantalum (Ta) and niobium (Nb) are also important, although their contribution to this field is small. The biocompatibility of pure titanium and its alloys is higher than that of other basic biomaterials, such as stainless steel and cobalt-chromium alloys. Titanium alloys exhibit a high ratio tensile strength / density and a good corrosion resistance. Therefore, titanium alloys have attracted a lot of attention in medical applications. Especially α+β type titanium alloys such as Ti-6Al-7Nb with a combination of mechanical properties and biocompatibility have been recognized as suitable candidates for bone implants. Table 1 shows typical applications of common metallic biomaterials in surgery [12], [13].

Table 1. Applications of main metallic biomaterials.

Applications	Metals
Craniofacial (plate and screw)	316L Stainless steel, Co-Cr-Mo alloy, Ti, Ti-6Al-4V alloy
Dental implants	Ti, Ti-6Al-4V, Ti-6Al-7Nb alloy, Co-Cr-Mo based alloys
Arch wire	Stainless steels, Ti-Ni alloy
Crown, Bridge	Au-Cu-Ag alloy, Au-Cu-Ag-Pt-Pd alloy, Ti, Ti-6Al-4V
Cardiac pacemaker	Electrode: Pt-Ir alloy, Ti
Vascular stent	316L Stainless steel, Cobalt-based alloys, Ti-Ni alloy
Artificial heart valve	Cobalt based alloys, Stainless steel, Ti-6Al-4V alloy
Spinal fixation	Ti-6Al-4V alloy, 316L Stainless steel, Ti-6Al-7Nb alloy
Hip implant	Ti-6Al-7Nb alloy, Co-Cr alloy, 316L Stainless steel
Artificial joints	316L Stainless steel, Ti-6Al-7Nb alloy
Bone fixation (plate, screw, pin)	316L Stainless steel, Ti-6Al-7Nb alloy

Before introducing (release) a new biomaterial into the market, it must meet the biocompatibility criteria by the international organizations, such as the US Food and Drug Administration (FDA), the International Standards Organization (ISO), the American Society for Testing and Materials (ASTM) and etc. [14]. For example, during a day, a human being makes several thousand steps with the frequency of 1 Hz, with the average being around 2000 steps. Therefore, the total number of steps over 20 years can be approximated as: 2000 steps $\times$ 365 $\times$ day $\times$ 20 years = 10^7 steps (cycles). Such cyclic loading can lead to the fatigue failure in various bone implants (hip and knee joints, spinal instruments, nails, plates, screws, wires etc.) [15]. Cyclic stress also happens in dental implants due to chewing as well as in cardiovascular implants (coronary stents) exposed to cyclic radial loading as response to the myocardial activity [16]. Therefore, determination of the fatigue strength of biomaterials, which is considered as one of the most important mechanical biocompatibility factors, is essential and vital. So, biomaterials must be subjected to strict fatigue strength tests based on the standards of international organizations (FDA, ISO, ASTM, …) for the long-term safe usage in vivo before introducing to the market. Typical fatigue mechanical working conditions of some implants are summarized in Table 2.

Table 2. Typical fatigue mechanical working conditions of some implants [16], [17].

Implant	Frequency of load (Hz)	Expected total number of loading over the life time of a 65 years old patient (i.e. 20 years)
Joints	1	10^7
Pacemaker	1	10^9
Stent	1	4×10^8
Tooth fillings	1	10^7

As seen in Table 2 the expected total number of loading cycles of some important implants over the life time of a 65 years old patient should be in the range of high-cycle fatigue regime, 10^7–10^9. Therefore, accurate and detailed information about the high-cycle fatigue behavior of the basic materials provides a precious basis for reliable and valid design [17].

In the following a brief overview concerning the high cycle fatigue behavior of titanium based alloys is given. Ultrasonic fatigue experiments with a cyclic frequency of 20 kHz under fully reversed tension-compression loading (R = -1) were performed by M. Papakyriacou et al. [18] with polycrystalline annealed commercially pure b.c.c. niobium (c.p. Nb ann.), c.p. b.c.c. niobium cold worked condition (c.p. Nb cw), h.c.p. annealed c.p. titanium (c.p. Ti ann.), and Ti–6Al–7Nb alloy. Ultrasonic fatigue tests were performed using specimens with a circular cross-section and diameters of 4 mm (niobium and tantalum) and 3 mm (titanium and Ti–6Al–7Nb alloy), respectively. Their investigations were concentrated on the high cycle fatigue regime up to 2×10^8 cycles. At a cyclic frequency of 20 kHz, the mean endurance limits of c.p. Nb c.w. and c.p. Nb ann. are 255±15 MPa and 240±10 MPa respectively. According to the obtained results cold working of c.p. Nb increases the ultimate tensile strength and yield stress; however, the high cycle fatigue properties are not influenced significantly. This means that cold working is an appropriate method to increase the static strength of pure bcc Nb metal, but the increase of the cyclic properties in the high cycle regime is less pronounced. The mean endurance limit of c.p. Ti ann. was found to be 345±15 MPa while that of Ti–6Al–7Nb alloy is 540±40 MPa in ultrasonic fatigue experiments. The mean endurance limit of Ti–6Al–7Nb alloy at 10^7 cycles was measured by Mitsuo Niinomi at cyclic stresses of 580–710 MPa [19]. Their results show that Ti–6Al–7Nb alloy has the best fatigue properties among the materials investigated, while the lowest mean endurance limits were found for c.p. Nb ann. and c.p. Nb cw. The very high cycle fatigue properties of the titanium alloy Ti-6Al-4V with a duplex microstructure were investigated at room temperature on electropolished hourglass-shaped specimens with a diameter of 4 mm by M. Janecek et al. [20]. They found that in the very high cycle fatigue regime, with increasing N in the range from 10^7 to 10^{10} cycles, the stress amplitude remains constant, and unlike other structural materials, Ti-6Al-4V exhibits a distinct fatigue strength of approximately 460 MPa.

Although Ti-6Al-4V exhibits a high fatigue strength, recently aluminium and vanadium-free titanium alloys have been developed and investigated for medical applications. The main reason is that the use of aluminium in alloys applied in the human body is intensively under discussion due to susceptibility to cause Alzheimer's disease and breast cancer. There is also evidence of neonatal toxicity by aluminium. On the other hand, vanadium toxicity has almost been proved [21], [22]. Young's moduli of α+β type titanium alloys such as Ti-6Al-4V (∼110 GPa) are, however, higher compared with that of the cortical bone (10-30 GPa) [6]. For structural biomaterials used in implants that replace hard tissue, a combination of enhanced tensile, fatigue and wear properties with low elastic moduli is desired. If the Young's modulus of a load bearing implant made of metallic biomaterials is higher than that of the cortical bone, bone atrophy may occur because of the stress shielding between the implant and bone [23]. Stress shielding causes loosening of the implants such as artificial joints or bone re-fracture after extraction of the implants [24]. Theoretical studies on the effect of alloying elements on the strength and modulus of β-type bio-Ti alloys suggests that non-toxic and non-allergenic elements like Nb, Mo, Zr and Ta promote formation of β-type Ti alloys with enhanced strength and reduced Young's modulus [25]. These alloys are especially suitable for use in load bearing implants under fatigue conditions such as artificial hip joints, bone plates and screws, spinal instruments, and dental implants [8], [19], [26]. Some mechanical properties of metallic biomaterials are listed in Table

3, in which the mentioned values of the fatigue endurance strength are regardless of fatigue test conditions. It should be considered that the range of these mechanical properties depends on the conditions of manufacturing processes (thermal and mechanical processing conditions, cold working etc.). As seen in Table 3, it is obvious that the titanium based Ti-Nb alloys with a single β-phase (bcc lattice structure) have significantly lower elastic moduli.

Table 3. Mechanical properties of common metallic biomaterials [27], [28], [29], [30].

Material	Young's Modulus, E (GPa)	Yield Strength, σ_y (MPa)	Tensile Strength, σ_{UTS} (MPa)	Fatigue Endurance Strength, (MPa)
Stainless steel	190	221–1213	586–1351	241–820
Co-Cr alloys	210–253	448–1606	655–1896	207–793
c.p. Ti	100-110	400-485	520-760	200-430
Ti-6Al-4V	110-114	896–1050	965–1103	620-725
Ti–6Al–7Nb	110-126	800-840	1020-1060	580-710
Ti-Ni alloys	75-83	190-690	860	-
CG Ti-45Nb (present study)	**65**	**430**	**446**	**186-260**
UFG Ti-45Nb (present study)	**67**	**864**	**940**	**200**
Co-Cr L605 (present study)	**242**	**424**	**1021**	**343-397**
Cortical bone	15–30	30–70	70–150	27

Figs. 1a and b show a composition dependency of the Young's modulus of different stable and metastable phases and the phase diagram for Ti-Nb binary alloys [31]. A minimum in Young's modulus of 62 GPa was observed at around the composition of Ti-45 mass %Nb in the single β-phase region [31], [32].

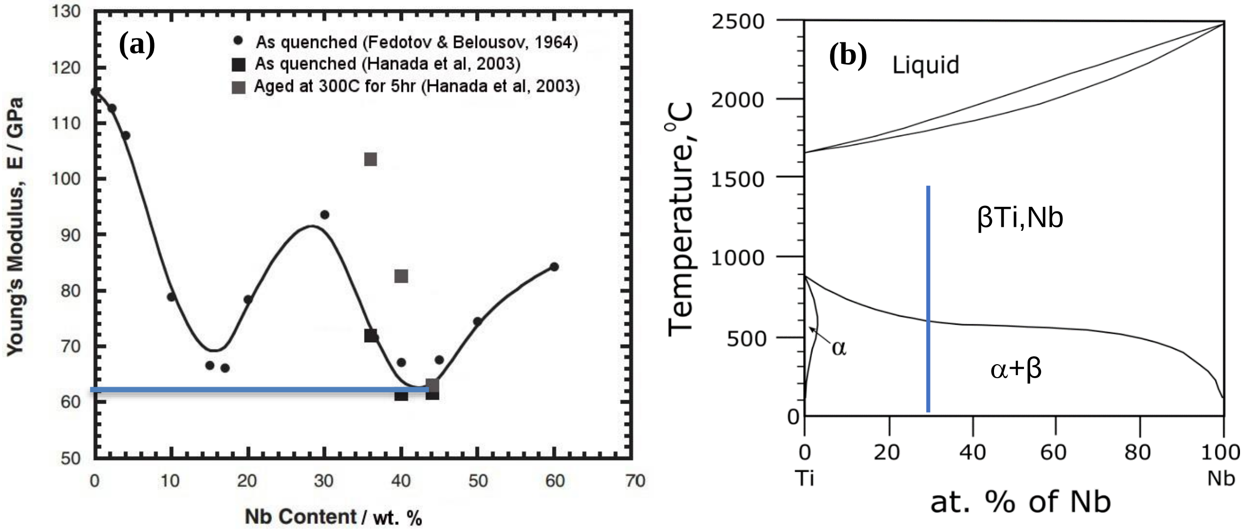

Fig. 1: (a) Nb content dependence of Young's modulus in quenched Ti-Nb binary alloys [31] , (b) Phase equilibrium diagram for Ti-Nb binary alloys [33].

Ti-45Nb alloy allows stabilizing a single ß-type phase with low Young´s modulus at room temperature. The Ti-Nb phase equilibrium diagram shown in Fig. 1b is calculated [30] using regular solution model of Gibb's free energy by method of CALPHAD, since there is no possibility to construct the experimental Ti-Nb phase equilibrium diagram below 600 °C due to the low diffusion rates. The experimental β/ (β+α) phase boundary matches with that of calculation above 600°C. The Ti-Nb system is a well-established thermodynamic system, since it is of interest for a variety of applications. Earlier studies refer to an application of these alloys as superconducting material [34]. For the long-term usage of metallic implants, biomechanical properties should be enhanced. Improvements in the static strength of biomaterials such as the tensile strength can be achieved by employing strengthening mechanisms including work hardening, grain refinement, precipitation and dispersion hardening. Severe plastic deformation (SPD) processes are defined as metal forming processes to fabricate ultrafine-grained (UFG) materials, via introducing extremely high plastic strains into a bulk metal [35]–[38]. Within the available techniques high pressure torsion (HPT) is an efficient SPD technique which usually requires considerably smaller total strain to achieve the desired submicron grain sizes [39], [40]. From a technological point of view, the structural application of HPT processed materials should be based on understanding and knowledge of their fatigue performance. Due to the grain refinement and increased tensile properties of UFG metallic materials, an enhanced fatigue life in comparison with their equivalent conventional grained (CG) materials might be expected. Previous investigations have shown that the anticipated improvement in fatigue life is highly dependent on the used starting material [41]–[44].

Co-Cr-based alloys have a long clinical background of applications in surgical and medical devices (like orthopedic implants, dental implants and stents) because of their excellent combination of strength, corrosion resistance, biocompatibility, non-ferromagnetism, and high resistance to fatigue. Among the various Co-Cr-based alloys, L605 being a non-magnetic superalloy also provides a high X-ray visibility due to the high density and a good corrosion resistance as well as high tensile strength and is suitable for stents designed with thinner struts. Conventional coronary stents are made from either medical-grade stainless steel 316L or NiTi. However, recently L605 Co-Cr alloy due to its prominent mechanical properties has attracted special attention for biomedical utilizations and has been introduced in cardiovascular applications such as heart valves and coronary stents. L605 Co-Cr alloy exhibits higher mechanical properties in comparison to stainless steel 316L. While mechanical properties of common Co-Cr-based alloys used for medical implants have been investigated to a large extent, the fatigue response of L605 Co-Cr alloy especially in the high-cycle regime has been rarely surveyed. Therefore, the fatigue characteristics of L605 Co-Cr should be investigated and determined for the long-term utilization in the body. High-cycle fatigue response of thin-walled tubes of Co-Cr L605 stent material, which contained holes as stress concentration sites, was investigated by **Khatibi** et al. [17]. Fatigue life curves, up to one Giga loading cycles, were determined using an ultrasonic resonance fatigue testing system. The fatigue strength of the L605 stent was reported to be 480 MPa at 4e8 number of cycles. They investigated the influence of the surface treatment on the fatigue performances of the stent material using tubes containing holes in as-laser cut condition, after electropolishing and coating. The results showed a clear influence of stent surface finishing procedures on the improvement of fatigue performance of the material leading to an increase of about 40% of stress level at specified range of loading cycle to failure.

Ritchie et al. [45] studied Co-Cr L605 stent material to determine the fatigue endurance strength under conditions of zero mean stress, i.e., at a load ratio of R = -1. They investigated fracture mechanics using finite-element computations and experimental fatigue testing to failure, including stress/life and crack propagation rate measurements, with special consideration made of the role of physically small cracks. The endurance strength was experimentally measured as the stress amplitude to yield a life of 4e8 number of cycles or greater (Operating in displacement control by using a rotating bending machine at a frequency of 60 Hz under stress amplitudes ranging from 200 to 625MPa). From these results, the 4E8 cycle endurance strength of the Co–Cr alloy was determined to be 207MPa. **Sweeney** et al. [46] carried out high cycle fatigue tests on L605 foil micro-specimens manufactured via laser-cutting and electro-polishing. These tests were performed under tensile–tensile loading conditions (R > 0). The resulting fatigue life in the range of 1E+05 and 1E+07 loading cycles is within 315-270 MPa. Their results based on the experimental fatigue tests demonstrated a clear trend following the Basquin-Goodman relation, where scatter in data is due to the dependence on microstructural inhomogeneity in the HCF loading regime, especially for micro-scale specimens. Slip lines were observed in a large number of grains, i.e. grains favourably oriented for slip. increasing stress range led to increased surface roughness and slip lines due to increased plasticity. Co-26Cr-9Ni superalloy was studied by **Jiang** et al. [47] to examine its fatigue behavior at the high-frequency (1,000 Hz) high-cycle fatigue tests (R= 0.05). The resulting fatigue endurance strength in the range of 1E+05 and 1E+09 loading cycles is within 700-470 MPa. Their microstructural investigations showed that the evolution of stacking faults have an important role on fatigue damage process and the number of stacking faults increases as cycling progressed. The fracture surface analysis exhibited that the crack-initiation site changes from the surface to subsurface, depending on the applied maximum stress and environment (e.g. oxygen and moisture). Samples with a long fatigue life failed due to the subsurface crack initiation. **Mishra** et al. [48] determined the endurance strength of the porous-coated and mock-sintered cast CoCr specimens reported to be about 207 MPa and 345 MPa at 1E+07 cycles, respectively, based on force controlled constant amplitude axial fatigue tests (R = 0.1) at 60 Hz in air at room temperature. Therefore, mock-sintered cast CoCr fatigue specimens showed a fatigue strength improvement of about 60% over the porous-coated cast CoCr specimens. The fatigue response of Co-Cr L605 alloy especially in the high-cycle regime and particularly on the bulk specimens has been rarely investigated. A summary of the available fatigue data of L605 and other Co-Cr alloys tested under different conditions is summarized in Table 4. It should be noted that a direct comparison of the fatigue results is only possible if different parameters such as sample size and geometry, fatigue testing methods (rotary bending, uniaxial), alloying elements, effect of mean stress, stress ratio and frequency on the fatigue strength are considered. Since the fatigue performance of Co-Cr based alloys in the very high cycle regime has not been investigated to date, therefore, high strength Co-Cr-based (L-605) alloy used for cardiovascular stents was considered in order to compare the fatigue properties of the bulk Ti-45Nb samples with another metallic biomaterial at the same conditions.

Table 4. A comparison of high cycle fatigue life of L605 alloy (present study) with published values of lifetime of Co-Cr-based alloys.

Material	Fatigue tests conditions	Fatigue life [MPa]	Source
Co-Cr L605 thin tube	push–pull (R = -1; 20 kHz)	480 (4×10^8 cycles)	**Khatibi** et al. [17]
Co-Cr L605 stent	Rotating bending (R = -1; 60 Hz)	207 (4×10^8 cycles)	**Ritchie** et al. [45]
Co-Cr L605 foil micro-specimens	pull–pull (R > 0; 50 Hz)	315-270 (10^5 - 10^7 cycles)	**Sweeny** et al. [46]
Co-26Cr-9Ni	Uniaxial (R= 0.05; 1k Hz)	700-470 (10^5 - 10^9 cycles)	**Jiang** et al. [47]
Porous-coated cast Co-Cr	Axial (R = 0.1; 60 Hz)	207 (10^7 cycles)	**Mishra** et al. [48]
Mock-sintered cast Co-Cr	Axial (R = 0.1; 60 Hz)	345 (10^7 cycles)	**Mishra** et al. [48]
Co-Cr L605 mechanical polished bulk samples	push–pull (R = -1; 20 kHz)	475-397 (10^5 - 10^9 cycles)	**Present study**
Co-Cr L605 electropolished bulk samples	push–pull (R = -1; 20 kHz)	343 (10^9 cycles)	

Chapter 3: Fatigue (fundamentals)

3.1. Fatigue failure

In 1837 William Albert published the first article on fatigue which described a correlation between cyclic load and durability of the metal [49]. In 1839, Poncelet, used the term fatigue for the first time in a book on industrial mechanics describing fatigue failure due to the cyclic loading in the form of tension and compression. In 1842 Rankine showed the role of stress concentrations on crack initiation and also stated that the fatigue crack growth in railroad axle was an important aspect of the fatigue failure [49], [50]. In 1870 Wöhler exhibited that amplitude of cyclic stress is more important than maximum stress and introduced the implication of fatigue limit (endurance limit) in his work on railroad axles. In 1903 Ewing shows that the microscopic cracks are the origin of fatigue failure.

After the brief historical review of the fatigue phenomenon, some fundamental aspects and concepts of fatigue failures will be explained. A fatigue failure occurs due to the application of fluctuating or cyclic stresses which are often below the static load such as the tensile or yield strength of the material and causes failure of function of the material. In the high cycle fatigue, plastic deformation is negligible and a linear elastic behaviour can be assumed. Although the applied stress is low enough to be elastic, plastic deformation can take place at the crack tip (even though the overall applied stress may remain below the yield stress, at a local length scale, the stress intensity exceeds the tensile strength). The significant importance of fatigue is related to cause the catastrophic failure which occurs without any prior warning [51]. Approximately 90% of all metal failure is due to the fatigue failure. It is an usual event in load-bearing components in all mechanical services such as automobiles, aircrafts, ships, nuclear reactors, jet engines, turbine blades and other machinery, biomedical implants, and consumer products, which are subjected constantly to repetitive stresses in the form of tension, compression, bending, vibration, thermal expansion and contraction, or other stresses [52].

There are different types of fatigue failures including, creep fatigue; cyclic loads at high temperatures, thermal fatigue; cyclic changes in material's temperature, corrosion fatigue; cyclic loads applied in chemically aggressive or embrittling environment, fretting fatigue; cyclic stresses together with the oscillation motion and frictional sliding between surfaces, mechanical fatigue which is the focus of this study, involves cyclic mechanical loads defined as the variation of load from the mean value to the maximum and the minimum value and back to the mean value and thermo-mechanical fatigue; a combination of mechanical and thermal fatigue [53][54]. Fatigue failure has a typical structure and can be identified by the appearance of the fracture surface, which is typically smooth near the origin of the crack initiation and reflects the sequence of fatigue processes. The surface becomes rougher as the original crack increases in size during final crack propagation [52].

The progression of fatigue failures can be classified into three stages:

Crack initiation; failure starts frequently on or near the surface locally in the other words it usually happens at external surfaces but also internal surfaces, in places of the high stress concentration like notches or surface imperfections including rough surface, dents, scratches or corrosion pits, sharp corners, inclusions, grain boundaries, or dislocation concentrations, known as the initial zone of failure (the zone of nucleation of micro cracks) which has small size and smooth surface. Crack propagation; the cracks gradually develop and coalesce to a single main crack, where is called the fatigue zone. Final failure; a sudden catastrophic fracture occurs after the crack reaches a critical size which forms the final or fast failure zone.

Generally, fatigue properties of a material can be affected by many factors which describe the influence of a specific condition on fatigue life. The following factors play an important role in fatigue failure [55].

Surface quality or surface condition (e.g. rough surface, scratches, dents, identification marks, corrosion pits, inclusions, polished, ground, machined, as-forged, corroded, etc.) is one of the main factor influencing on the fatigue behaviour.

Temperature factor accounts for reductions in fatigue properties.

Residual stresses are caused by manufacturing processes and may adversely or positively affect the fatigue behaviour.

Stress concentrations such as keyways, holes, sharp corners and notches act as stress raisers and can easily lead to a fatigue failure.

Microstructure including alloy composition and its grain size can affect its fatigue properties.

Heat treatment reduces residual stresses within a metal and improves fatigue properties. If the residual stresses are compressive at the surface, removal of residual stress leads to a reduction of the fatigue performance.

3.2. Fatigue life

Fatigue life is the total number of loading cycles of a material withstanding a specified stress level before failure occurs, denoted by N. Fatigue life is a function of the magnitude of the fluctuating stress, geometry of the specimen and test conditions [55]. The original approach to fatigue design involved characterizing the total fatigue life to failure of initially uncracked test pieces in terms of the number of loading cycles at an applied strain range (low-cycle fatigue) or stress range (the S–N curve in high-cycle and very high cycle fatigue). Low cycle fatigue (LCF) tests conducted in strain-based approaches are characterized by high stress amplitudes and plastic strains for lifetimes smaller than 10^5 cycles to failure; high cycle fatigue (HCF) tests are usually stress controlled and characterized by low stress amplitude and elastic strains for lifetimes between 10^5 and 10^8 cycles to failure and ultra-high cycle fatigue (UHCF) regime above 10^9 cycles to failure. Technical testing methods are very important for minimizing costs and maximizing safety and reliability, since it needs predicting how long a product will survive under a certain number of loading cycles before fatigue failure happens, in other words, when fatigue failure of a product is imminent. Conventional fatigue test is not only time consuming but also costly. With the conventional fatigue testing equipment, operating at loading cycle (frequency) of 10-100 Hz, the testing times required to set up the fatigue failure at the very high cycle regime are very long (3 years). While, the ultrasonic fatigue testing system, operating at a typical frequency of 20 kHz, can obtain fatigue testing data (S-N curve) for fatigue life greater than 10^9 loading cycles in a remarkable reduction of testing time in about 14 hours. So, the ultrasonic fatigue testing system is a suitable practical technique giving the possibility to perform testing of materials in a sensible time [56].

Cyclic Stresses

Fatigue failure can occur at loads considerably lower than tensile or yield strengths of a material by applying a axial, torsional or flexural loads under fluctuating or cyclic stresses [57]–[59]. Cyclic stresses are characterized by using parameters such as stress range, stress amplitude, mean stress, and stress ratio defined using maximum and minimum applied stresses (σ_{max} and σ_{min}) as;

Cyclic stress range: $\Delta\sigma = \sigma_{max} - \sigma_{min}$, **Cyclic stress amplitude:** $\sigma_a = (\sigma_{max} - \sigma_{min})/2$,

Mean stress: $\sigma_m = (\sigma_{max} + \sigma_{min})/2$, **Stress ratio:** $R = \sigma_{min}/\sigma_{max}$,

Amplitude ratio: $A = \sigma_a / \sigma_m = (1-R) / (1+R)$.

The different types of fatigue loadings and corresponding cyclic stresses are shown in Fig. 2.

Fig. 2a shows the simplest type of cyclic stress (sinusoidal stress) as a function of time, where the stress amplitude is equal to the maximum stress and the mean stress is zero in other words maximum and minimum applied stresses are of equal magnitude. Fig. 2b shows similar characteristic but with the non-zero mean stress in this case, the maximum and minimum applied stresses are not equal. Fig. 2c shows a complicated stress cycle with random stress fluctuations.

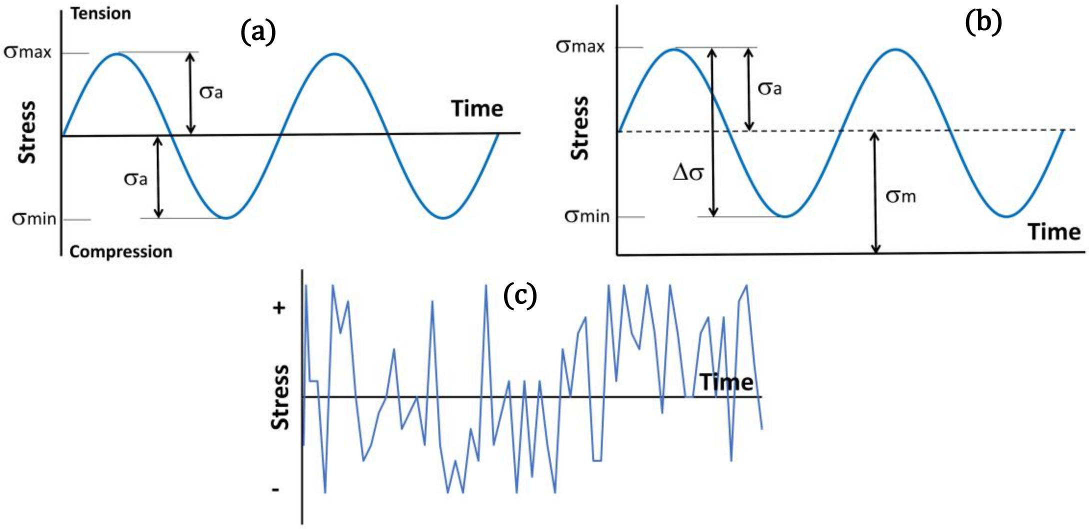

Fig. 2: Cyclic Stresses of fatigue testing; (a) Periodic and symmetrical with zero mean stress (b) Periodic and symmetrical with none zero mean stress (c) Random stress fluctuations.

3.3. The S–N Curve (Wöhler Curve) and fatigue parameters

Most fatigue data such as HCF and VHCF are usually presented in a plot with the cyclic stress amplitude ($S = \sigma_a$) versus the logarithmic scale of the number of cycles to failure (N). This plot is called the S-N curve also known as a Wöhler diagram [50]. In most alloys, such as aluminium alloys as seen in Fig. 3, cyclic stress decreases continuously with increasing number of cycles. In these cases, the fatigue properties are described by fatigue strength defined as stress at which fracture occurs after a specified number of cycles (usually 10^7 cycles). Normally, the fatigue strength increases as the static tensile strength increases. However, under constant amplitude loading conditions, low-carbon steel alloys and other materials which harden by strain-ageing (Fig. 3) exhibit a limiting stress level in the S-N plot typically beyond about 10^7 fatigue cycles. In this case the curve becomes asymptotic to horizontal line [60]. Below this horizontal level known as the fatigue limit or endurance limit, it is assumed that the specimen does not fail even after very long number of cycles [50], [55].

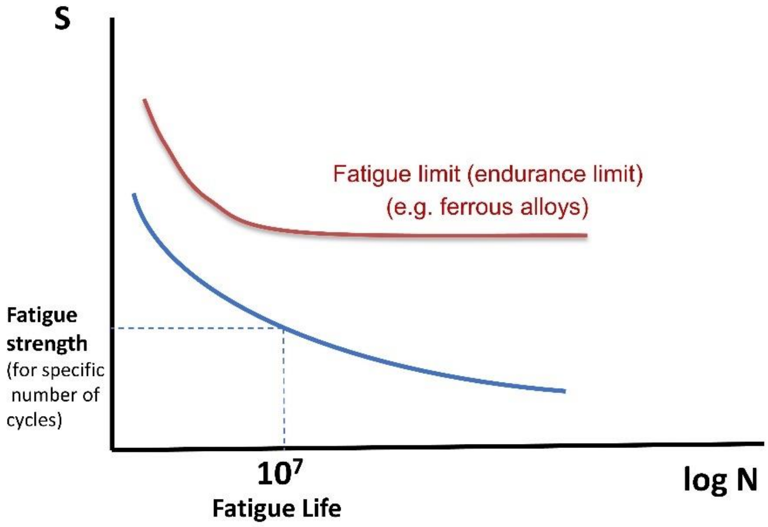

Fig. 3: Typical S-N curve showing fatigue limit and fatigue strength.

3.4. Multi-stage fatigue life curve

The entire fatigue life of a metallic material including LCF, HCF and UHCF may exhibit a multi-stage behaviour with a transition of the location of fatigue crack initiation from the surface to subsurface. Mughrabi [61], [62] suggested to distinguish between the different types of materials in ultrahigh cycle fatigue (UHCF) regime (the number of cycle to failure exceeds 10^9) by classifying: (a) type-I materials which are ductile defect free single phase materials (e.g. fcc metals and alloys), (b) type-II materials which are brittle high strength materials with internal defects such as inclusions or pores (e.g. steels and cast materials) [63], [64]. Fig. 4 shows a multi-stage fatigue life curve for type-II materials. Sakai et al. [65] and Mughrabi [64] state that such a type of curve has been found in particular for rotating bending. In the LCF and HCF ranges (failure at $<10^5$ and 10^5–10^8 loading cycles) the crack initiation sites are usually found at the surface whereas they are subsurface in the UHCF range. In contrast, there are also literatures reported fatigue failures of the specimens due to near-surface crack origin in UHCF regime [66], [67].

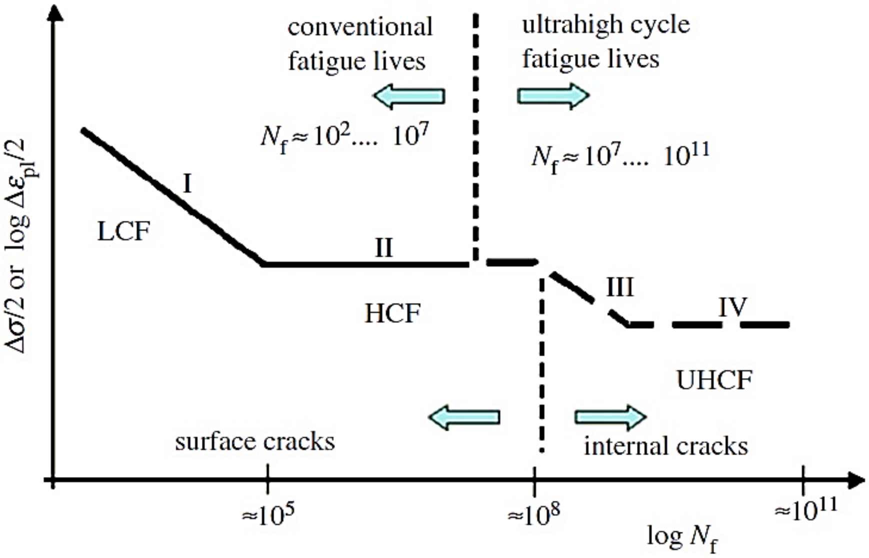

Fig. 4: Schematic multi-stage stress-fatigue life (S–N_f) curves according to Mughrabi [63], [64] for type II materials, showing LCF, HCF and UHCF fatigue ranges and transition from surface to subsurface cracks.

3.5. Mechanism of fatigue failure

Fatigue mechanism is essential for the analysis and investigation of fatigue properties such as fatigue life and fatigue crack growth. If fatigue mechanism is comprehended fatigue prediction methods can be evaluated [68]. The mechanism of metallic fatigue failure is usually related to the growth and accumulation of microplastic deformations in the surface layer of the material which is based on dislocation motion. In other words, slip lines are caused by fatigue crack initiation and crack growth and lead to the local cyclic microplastic deformation, which is a consequence of dislocation activities. In desirable crystallographic orientations according to the Schmid's law, in which the critical resolved shear stress has been overcome, local plastic deformation in the material occurs due to the slip bands formation [53]. Dislocations can move at stresses below the yield stress due to the anisotropy and random orientation of crystals in the metal structure occurring in a small number of grains preferably at the material surface, leading to the limited dislocation movements, since slip lines can move more easily at the material surface [69], [70].

With continuing cyclic loading on the metallic material, a crack will finally be formed and begin to grow through the grains, because in most materials, fatigue cracks grow in a transgranular manner, which is the microscopic feature of a fatigue fracture surface [53], [71]. A stress concentration created by the crack causes a new local microplastic deformation and this process is repeated until the crack becomes large enough to generate a larger amount of plasticity and in the case of a uniaxial tensile stress, the crack has started to grow perpendicular to the loading direction. Therefore, the density of slip lines is increased and shows themselves as slip bands. The back and forth fine/local slip movements of fatigue can cause the slip band to form intrusions (notches) and extrusions (ridges) at the surface [72] shown in Fig. 5. Extrusions and intrusions being the consequence of the persistent slip bands form a rough surface. Strain concentration in intrusion zones is rather high therefore, density of vacancies and dislocations would be high, resulting in the formation of voids which join together to form submicrocracks. The coalescence of submicrocracks leads to the microcrack formation [54], [73].

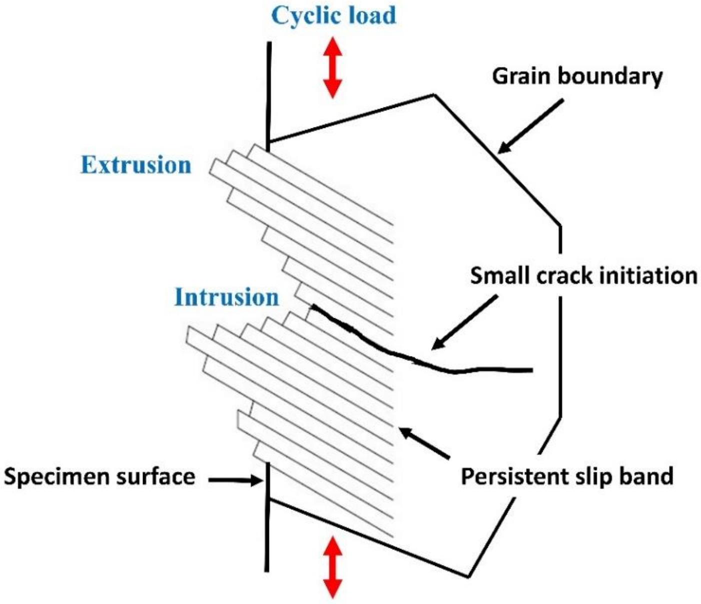

Fig. 5: Cycle slip caused by cycle stress leading to the arrangement change of slip band to form extrusion and intrusion at the surface [53].

3.6. Comparison of different crack initiation modes in LCF, HCF and UHCF

As shown in Fig. 6 three different modes depending on frequency and sites of crack initiation have been proposed in a cylindrical sample with a polished surface varying from LCF to HCF and then UHCF. In the LCF range, failures are often due to the multiple crack initiation sites arising at the surface. In the HCF regime, crack initiation normally originates from one site caused by the surface defects. Finally, in the UHCF range, surface defects do not play dominant role than internal defects. So, in this case the crack initiation is rather located at an internal zone [74], [75]. In contrast, there are also literatures reported fatigue failures of the specimens due to near-surface crack origin in UHCF regime [66], [67].

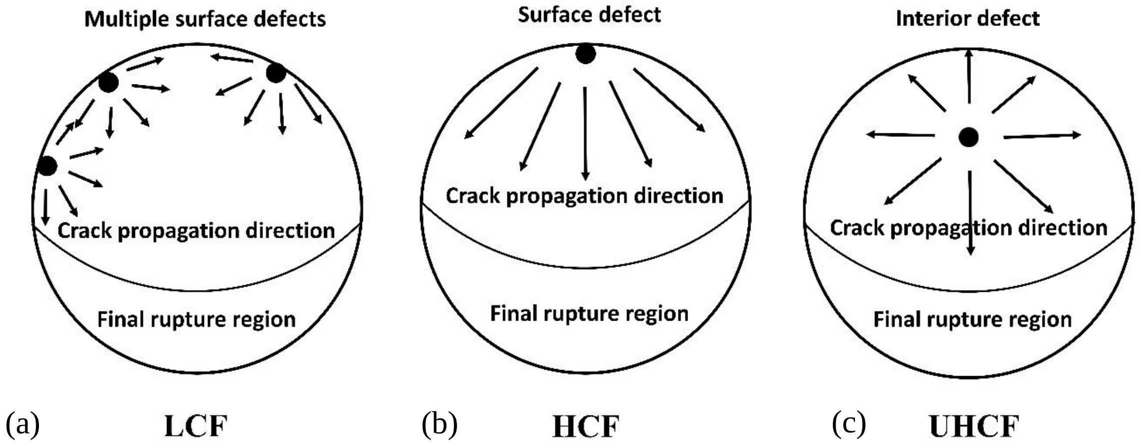

Fig. 6: Schematic of different crack initiation modes in LCF, HCF and UHCF showing shift of fatigue crack initiation sites from surface to interior: (a) fatigue crack initiation from multiple surface defects in LCF fatigue regime (b) fatigue crack initiation from surface defect in HCF fatigue regime (c) fatigue crack initiation from interior defect in UHCF fatigue regime [74]–[76].

3.7. Fatigue fracture surface

The fracture surface of a metallic material after fatigue failure, which is a brittle fracture, has a characteristic appearance (Fig. 7), including smooth and rough regions which is due to the different stages of damage process under cyclic loading related to the crack growth and final rupture, occurring in a ductile manner, respectively [52], [77]. Usually, the fatigue fracture surface examinations reveal the most characteristic pattern consists of concentric rings spread over the fracture surface in the smooth region, known as beach marks (or clamshell, conchoidal, and arrest marks) being macroscopic dimensions (may be observed with the naked eye), diverging outward from a central point which is the nucleation of the failure. In which each beach mark band shows a period of time over which crack growth occurred [78], [79]. Another characteristic of a fatigue fracture surface being microscopic feature is termed striations. The orientation of fatigue striations is perpendicular to the microscopic direction of crack propagation [80]. Striation width increases with increasing stress range. Within a single beach mark, thousands of striations may be found [71]. The relatively widely spaced striations are caused by variations in the stress amplitude during the life of the component.

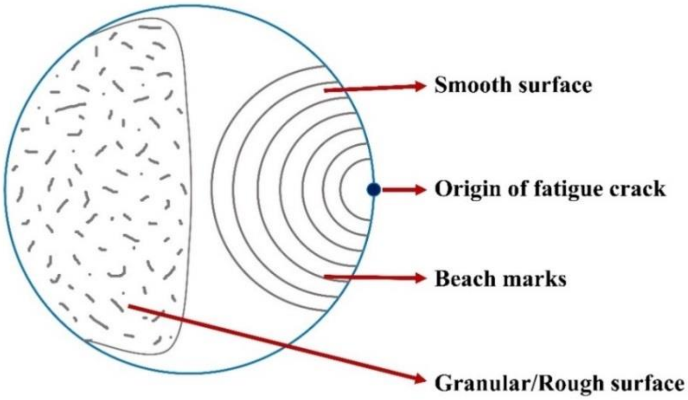

Fig. 7: A typical fatigue-fracture surface.

3.8. Notch effect and notch sensitivity

The existence of geometrical notches leading to an inhomogeneous stress distribution contains a stress concentration at the root of the notch acting as a stress raiser. Theoretical stress concentration factor, K_t, for normal stress (tension or bending) which is based on the assumption of the elastic behaviour of a material, is defined as the ratio of the maximum stress in the element to the nominal stress (Eq. 3.1) [81]

$$K_t = \sigma_{max} / \sigma_0 \tag{3.1}$$

The stress concentration intensity depends on the shape of the notch. With respect to the definition of K_t, which is dimensionless, it is dependent on dimensionless geometrical ratios. Fatigue phenomenon usually occurs at stresses below the yield stress, therefore, elasticity theory can be applicable. The fatigue notch sensitivity factor can be determined, in order to estimate the influence of stress concentration on the fatigue performance. The fatigue notch factor K_f is defined as

$$K_f = \sigma_{smooth} / \sigma_{notch} \tag{3.2}$$

where σ_{smooth} being the fatigue limit of unnotched bodies and σ_{notch} being the fatigue limit of notched bodies. The fatigue notch sensitivity factor q, is obtained [82][83] according to the equation

$$q = \frac{K_f - 1}{K_t - 1} \tag{3.3}$$

where $0 \leq q \leq 1$. The full notch sensitivity is given by q=1 ($K_f = K_t$) and complete notch insensitivity is given by q=0 ($K_f = 1$). In the present study, the fatigue notch factor was determined based on the measured and calculated stress amplitudes at 10^9 loading cycles.

Chapter 4: Ultrafine grained and nanostructured materials

For the long-term usage of metallic implants, biomechanical properties should be enhanced. Improvements in the static strength of biomaterials such as the tensile strength can be achieved by employing strengthening mechanisms including work hardening, grain refinement, precipitation and dispersion hardening, leading to the nanocrystalline (grain sizes below 100 nm) and ultrafine-grained (UFG) materials (grain sizes between 100 nm to 1000 nm). In general, two different approaches can be used to produce nanocrystalline and ultrafine grained materials which are termed bottom-up and top-down [84]–[88].

Assembling of individual atoms or atom cluster or nanoscale particles to construction of nanocrystalline materials is known as the bottom-up approach, such as; inert gas condensation, electrodeposition, chemical and physical deposition and cryomilling with hot isostatic pressing [84]–[89]. Grain sizes reported by this approach are in a range of 1 to 100 nm. Nanocrystalline materials produced by this approach are of relatively small sizes. Since this approach is not the subject of this study it will not be explained more.

The top-down approach can be usually performed by ball milling method, in which nanoparticles are produced from bulk solid materials by mechanical devices and methods, or SPD techniques, at which the coarse grained bulk metallic materials are converted to materials with the ultrafine grained structure by means of ultra-high straining deformation processes [90]. By SPD techniques explained in more details larger samples can be produced.

4.1. Severe plastic deformation (SPD) techniques

SPD processes are defined as metal deformation processes to fabricate ultrafine-grained materials, via introducing extremely high plastic strains into a bulk metal [91], [92]. Severe plastic deformation (SPD) techniques increase the strength of material by generation of dislocations and grain refinement based on Taylor relation and Hall Petch equation, respectively [92], [93], as described below.

Strengthening by increase of dislocation density

If the ductile metals are deformed plastically at temperatures below the melting point they become stronger. This process is called strain hardening (or work hardening or cold working).

In fact, the increase of dislocation density by plastic deformation is the reason for increasing the strength. During plastic deformation, the average distance between dislocations decreases and dislocations start blocking the motion of each other. For an estimation of dislocation density connected with the flow stress, the Taylor relation can be used [88], which correlates the dislocation density ρ with the shear stress τ as

$$\tau = \tau_0 + \alpha G b \sqrt{\rho} \tag{4.1}$$

Where, τ_0 is the shear stress resistance to dislocation motion in the absence of dislocations.
G is the shear modulus, b is the Burgers vector and α is a dimensionless parameter which varies with;$\alpha=1/8\pi(1-\nu)$ where ν is Poisson's ratio [94].

Strengthening by grain-size reduction

The finer grains result in a larger area of grain boundaries that lead to impede the dislocation motion. In fact, the strength of a material increases due to the accumulation of the dislocations which are hindered by grain boundaries. Grain-size reduction usually improves toughness as well. **Hall-Petch equation** [85], [87] indicates the effect of grain size on the stress required to move the dislocation in a polycrystalline metals which relates the yield stress, σ_y, to the grain size (grain diameter), D, is expressed as:

$$\sigma_y = \sigma_{\mathbf{0}} + k_y D^{-1/2} \tag{4.2}$$

where σ_0 and k_y are material constants known as the frictional stress opposing the dislocation motion which is the yield stress with an infinitely large grain size and the Hall-Petch slope (or the Hall-Petch parameter), respectively. This relationship shows that yield stress will increase linearly with the inverse square root of the grain size through the nanoscale regime. For fcc materials, k_y values are generally less than 0.3 MN/m$^{3/2}$ while those for bcc materials are higher by a factor of 2 to 3 [95].

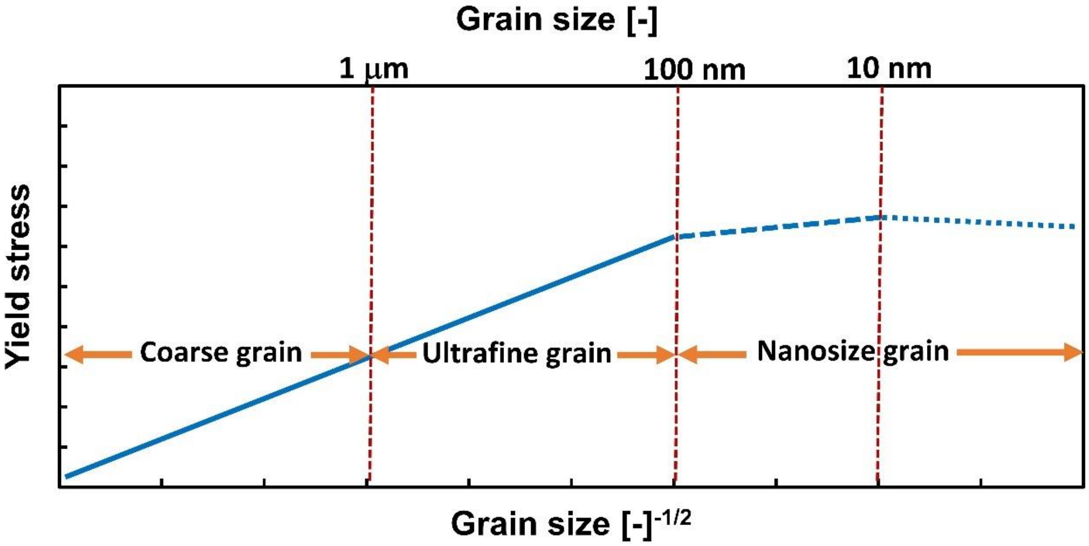

Fig. 8: Typical representation of yield stress as a function of grain size in the (a) ultrafine grain size range (b) nano grain size range showing Hall-Petch characteristics [96].

Hall-Petch equation has been confirmed for large-grained materials at which grain sizes, d, are greater than 100 nm (ultrafine grain size range) [96], [97]. The experimental results show that in the nano grain size range, there is the same relationship between the yield stress and the grain size but different material constants, σ_0 and k_y, as shown in Fig. 8. In other words, in the 100 nm - 10 nm range with the decreasing grain size the yield stress also increases, but not so much as in the ultrafine grain size range. For some materials, the Hall-Petch relationship breaks down when the grain size is reduced less than 10 nm and it has been suggested that an inverse Hall-Petch relationship exists with a negative slope [98].

Usually, SPD techniques do not change the young's modulus significantly. Fabricating ultrafine grained and nanostructured materials processed by SPD has grown significantly in the recent decades due to the desirable mechanical properties, therefore, various SPD techniques are now available such as equal-channel angular pressing (ECAP), accumulative rolling bonding (ARB), high pressure torsion (HPT), hydrostatic extrusion (HE), cyclic extrusion compression (CEC), repetitive corrugation and straightening (RCS), torsion extrusion, severe torsion straining (STS), cyclic closed-die forging (CCDF), super short multi-pass rolling (SSMR), etc. [90], [99], [100].

Within the mentioned available techniques equal-channel angular pressing (ECAP) and high pressure torsion (HPT) are efficient SPD techniques, both methods induce deformation by shear, which usually require considerably smaller total strain to achieve the desired submicron grain sizes [85], [87], [101], [99].

4.1.1. Equal-Channel Angular Pressing (ECAP)

In ECAP method the rod-shaped billet is severely shear strained by pressing through a die that has two channels which intersect at a certain angle φ, often equal to 90°. The most ECAP dies have a channel with a quadratic cross-section. Since the outer dimensions of the billet remain constant after passing the channel, the procedure can be repeated many times and get a large accumulated strain. The equivalent strain, ε, during each ECAP pass is given by the following equation:

$$\varepsilon_{ECAP} = \frac{N}{\sqrt{3}}.2\left(\cot\left(\frac{\varphi}{2}+\frac{\psi}{2}\right)+\psi\cos ec\left(\frac{\varphi}{2}+\frac{\psi}{2}\right)\right) \tag{4.3}$$

where φ and ψ are the channel angle and curvature of the outer corner, respectively, and N is the number of passes. Fig. 9 shows schematically the principle of ECAP procedure.

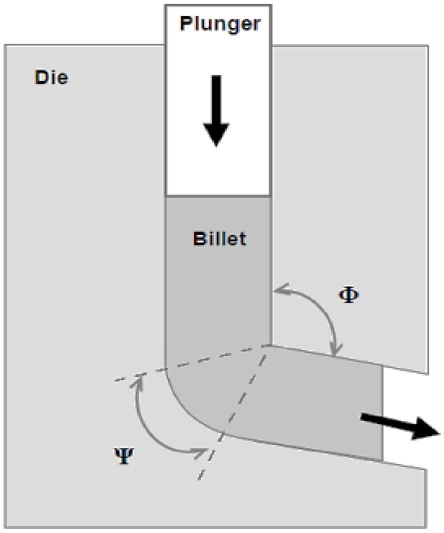

Fig. 9: Principle of ECAP procedure.

The billets can be rotated relative to the die between the passes leading to four different ECAP routes including route A, route Ba, route Bc and route C. ECAP method is capable to produce large scale specimens and can be applied to most commercial alloys [102]–[104].

4.1.2. High Pressure Torsion (HPT)

HPT is preferable in comparison to other SPD methods since it is possible to **a)** form a nanometric grain size (smaller than 100 nm) **b)** adjust cumulative strain and achieve very high strain **c)** select hydrostatic pressure and deformation speed **d)** obtain UFG materials with a fairly uniform structure if samples are deformed to saturation. However, this SPD method as of yet can only be implemented for small samples. In the present study, high pressure torsion (HPT) was applied to enhance the tensile properties of the alloy without increasing the Young's modulus. Therefore, HPT will be explained in the following. The disc which is located in a closed die is compressed by a very high pressure, and plastic torsional straining is achieved by rotation of one of the anvils. The equivalent strain according to the von Misses yield criterion is given by [62]

$$\varepsilon = 2\pi N r / h\sqrt{3} \tag{4.4}$$

where r is the radius of the disc, N the number of rotations and h the final thickness of the disc after HPT deformation [105], [106]–[108]. The principle of HPT is illustrated schematically in Fig. 10.

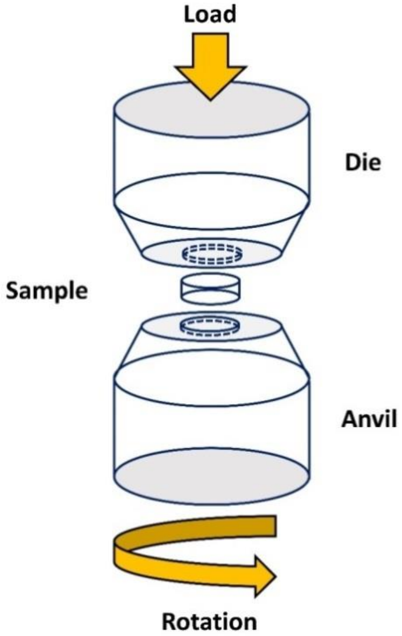

Fig. 10: The principle of HPT deformation processing (schematic).

The disk located in a closed die is compressed by a very high pressure, and plastic torsional straining is achieved by rotation of one of the anvils.

In the present study, high pressure torsion (HPT) technique was applied to enhance the tensile properties of the Ti-45Nb alloy. More details on deformation conditions and sample geometry are given in the next chapter.

Chapter 5: Materials, experimental details and methods

5.1. Materials

The studies were performed on the samples prepared from the conventional grained original Ti-45Nb alloy, ultrafine grained HPT processed Ti-45Nb alloy denoted by CG and UFG, respectively and Co-20Cr-15W-10Ni (L605) which compositions are represented in weight percent (wt.%). The Ti-45Nb alloy investigated in the present work was a hot hydrostatic extruded (HHE) β-type Ti-45Nb (wt.%) alloy provided as bars with a diameter of 42 mm and chemical composition as given in Table 5 received from ATI Wah Chang, Alabama, USA.

Table 5. Chemical composition of HHE bar of Ti–45 Nb (wt.%).

Composition	Nb	Fe	Cr	Mn	Mg	Si	K	Na	O	N	Ti
	44.94	<0.03	<0.01	<0.01	<0.01	<0.1	<0.01	<0.01	0.095	0.007	BAL

The composition of the L605 used in this study is Co–20Cr–15W–10Ni with max 3 wt.% Fe, 1.5 wt.% Mn, 0.1 wt.% C and traces of Si, P and S as given in Table 6. The material was provided as bars with a diameter of 12.7 mm which was purchased from Robemetal GmbH, Rockenberg-Oppershofen, Germany. The microstructure of L605 superalloy consists of a solid solution fcc γ phase -cobalt matrix, in which Cr and W carbides (M23C6 and M6C precipitates) are distributed.

Table 6. Chemical composition of bar of L605 (wt.%).

Composition	Cr	Ni	W	C	Fe	Mn	Si	P	S	Co
	19.88	10.07	14.84	0.12	0.99	1.49	0.06	0.03	<0.00003	BAL

5.2. Experimental details and methods

The influences of microstructure, specimen size and geometry on the fatigue life and crack growth behaviour of these biocompatible alloys were investigated. Fatigue response in the very high cycle regime was studied by using an ultrasonic resonance fatigue testing system working at 20 kHz. High pressure torsion (HPT) was applied to enhance the mechanical properties of the Ti–45Nb alloy without increasing the Young's modulus. Mechanical properties were investigated by tensile experiments, microhardness and nanoindentation measurements. Microstructural characterization was conducted by means of optical and electron microscopy techniques (SEM-EBSD, TEM, etc.). For a better understanding and interpretation of the fatigue response, surface damage, crack path morphology and microstructural evolution of the fatigued specimens were studied. Additionally, Finite Element Method (FEM) simulation was conducted for interpretation of the experimental results and establishment of lifetime prediction curves.

5.2.1. High Pressure Torsion (HPT)

The UFG Ti-45Nb specimens processed by HPT for micro tensile tests, microhardness measurements and miniaturized fatigue experiments were cut at the radius of about 2 mm from the centre of the HPT discs to assure a similar microstructure at the gauge section as indicated with blue color in the disc illustrated in Fig. 11.

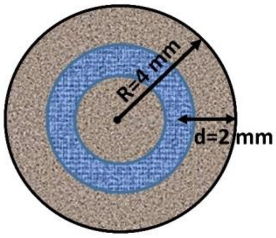

Fig. 11: All the required samples were prepared from the blue area indicated on the HPT disc (ε= 82).

In this work, slices with a thickness of about 1 mm and diameter of 8 mm were cut by electro discharge machining (EDM) from the conventional grained original Ti-45Nb material normal to the axis of the bars. Then, all samples were mechanically thinned to the thickness of 0.8 mm and were sandblasted in order to provide enough friction needed for the continuous torsion of the samples. Finally, the Ti-45Nb discs were deformed by HPT under a hydrostatic pressure of 4 GPa and the number of rotations N = 1, 5 and 10 at room temperature (RT) leading to an equivalent strain (ε) of 16, 82 and 170 at a radius of 2 mm from the centre of the specimen. In all the cases the rotation speed was maintained to 0.2 rpm (revolutions per minute). Thickness of the samples after doing HPT processing of different number of rotations of N = 1, 5, 10 was in the range of 0.43–0.45 mm. Table 7 shows summary of data related to the HPT processed Ti–45Nb samples at RT. From a technological point of view, the structural application of HPT processed materials should be based on understanding and knowledge of their fatigue performance. Due to grain refinement and increased tensile properties of UFG metallic materials, an enhanced fatigue life in comparison with their equivalent conventional grained (CG) materials might be expected.

Table 7. Summary of data related to the HPT processed Ti–45Nb samples at RT. The equivalent strain (ε) is calculated at a radius of 2 mm from the center of the HPT disc.

Sample	Initial thickness (mm)	Final thickness (mm)	equivalent strain (ε)
CG.Ti-45Nb	0.80	0.80	0
HPT-4-1	0.81	0.45	16
HPT-4-5	0.82	0.44	82
HPT-4-10	0.80	0.43	170

5.2.2. X-ray diffraction (XRD)

The X-ray diffraction is a common and nondestructive technique which is usually used for identification of the structure and morphology of the materials, crystalline phase analysis, dislocation density, determination of the orientations (texture), lattice dimensions, stacking faults and so on [109]. In this study, Wide angle x-ray scattering (WAXS) experiments were used to determine the crystal phases as well the density of dislocations.

5.2.2.1. X-ray line profile analysis (XLPA)

Williamson Hall analysis was used for evaluating the X-ray line profiles. This method is based on the fact that the Full Width at Half Maximum, FWHM, is influenced by two broadening effects; the crystallite-size and lattice distortion which is described below [110]–[112].

$$\Delta K_{FWHM} = \alpha K + \frac{0.9}{L} \qquad (5.1)$$

In which, L is the crystallite size, K is the diffraction vector, ΔK_{FWHM} , α and K are defined as

$$\Delta K_{FWHM} = \frac{\beta_{tot} \cos\theta}{\lambda} \quad , \quad \alpha = \frac{C_{\varepsilon}}{2} \quad , \quad K = \frac{2\sin\theta}{\lambda} \qquad (5.2)$$

αK is the strain contribution to the peak broadening resulting from lattice distortions which depend on the crystallite size. Therefore, by plotting ΔK_{FWHM} versus the diffraction vector K , the broadenings caused by the size and strain can be separated and y-intercept of the plot gives $\frac{0.9}{L}$ and the slope of the plot gives the density of dislocations.

For the present study, a Bruker-AXS Discovery 8 X-ray diffractometer with a 2D detector using Cu Kα source with an accelerating voltage of 40 kV and a current of 30 mA was used for the analyses of composition of phases. The Fityk program was used for data processing and nonlinear curve fitting in order to analyze data from X-ray diffraction. The Voigt function was used for fitting the peaks. The intensity profiles obtained from the X-ray diffraction experiment were normalized after removing the background. The obtained results will be presented in chapter 6.

5.2.2.2. CMWP method

The dislocation density of the initial and HPT Ti-45Nb samples before and after fatigue processing was measured by high-resolution diffraction peak-profile analysis [113], [114]. The X-ray data were recorded using a highly monochromatic X-ray beam (with $d\lambda/\lambda=10^{-4}$) with a Curved Position Sensitive Detector INEL CPS-590 positioned at a distance of 480 mm from the specimen and Cu anode generator at 45 kV and 80 mA with a Ge single crystal monochromator. The line profiles were evaluated using the extended convolutional multiple whole profile (CMWP) procedure [115], [116]. In the CMWP-fit method, all the measured peaks are fitted by the sum of a background spline and the convolution of the instrumental profiles and the theoretical line profiles related to the crystallite size, dislocations and twin faults [113], [115]–[117]. The distances between the specimen and detector were selected such that the instrumental effect was always <10% of the physical broadening. The photon energy used was 8 keV, which corresponds to a wave length of Cu Kα2 radiation of 0.154 nm. The incident beam size was about 100 μm × 500 μm on the sample and the photon flux amounted to 5×10^{11} photons mm^{-2} s^{-1}. In case of fatigued and failed specimens, the X-ray beam was positioned on the middle of the plane surface of one of the broken parts.

5.2.3. Nanoindentation measurements

Nanoindentation technique was performed for characterization of the mechanical properties of the CG and UFG Ti-45Nb samples and initial L605 alloy. Nanoindentation measurements were conducted to study the effect of HPT processing parameters on the values of nanohardness and Young's modulus of the Ti-45Nb alloy. The measurements were carried out at room temperature by an ASMEC-Universal Nanomechanical Tester UNAT and using a Vickers indenter. The device was calibrated in terms of indenter stiffness and contact area using fused silica and sapphire standards. The measurements were carried out on the HPT discs on an area with the radius ranging from 2/5R to 3/5R as shown in Fig. 11 (marked with blue colour). About 50 single measurements were performed on each material from which an average value was obtained. Young's modulus was determined according to the methods given by Oliver and Pharr [118].

5.2.4. Micro tensile test

Micro tensile tests were carried out by a miniaturized tensile machine in order to measure the mechanical properties (e.g. Young's modulus, ultimate tensile strength, yield stress) of CG and UFG Ti-45Nb specimens. Due to the small specimen size of the HPT processed discs the strain measurement is not possible using techniques such as the strain gauge, extensometer or crosshead motion. The best way is to use the non-contact optical strain measurement technique with high local resolution by using laser speckle strain sensor (Fig. 12). The principle of the laser speckle method is based on the geometric optics approach introduced by Yamaguchi [119] where the strain is measured with high accuracy, using the observation and tracking of the speckles that are moving due to an applied load and straining. Speckle patterns can be produced by coherent laser beam which interfere with itself due to the reflecting off an optically rough surface. Indeed, when the coherent light hits the slightly rough surface (optically) the phase of all the rays is altered randomly and this leads to either constructive or destructive interference, therefore cause the bright and dark pattern. Yamaguchi showed that the speckle displacement observed at a given point e.g. at angle θ_0 due to the straining sample illuminated at angle θ_s can be represented by

$$A_x(\Theta) = a_x\left[\frac{L\cos^2\Theta_s}{L_S\cos\Theta}+\cos\Theta\right] - a_z\left[\frac{L\cos\Theta_s\sin\Theta_s}{L_S\cos\Theta}+\sin\Theta\right] - L\left[\varepsilon_{xx}\left(\frac{\sin\Theta_s}{\cos\Theta}+\tan\Theta\right)-\Omega_y\left(\frac{\cos\Theta_s}{\cos\Theta}+1\right)\right] \tag{5.3}$$

Where, a_x and a_z are the rigid body displacements along x- and z-axis respectively, θ called the observation angle which is the angle between the camera and the surface normal (z-axis), the angle θ_s is the angle between the laser beam and the surface normal (z-axis) which can be zero if the laser beam place along z-axis, L is the distance between sample surface and the camera, L_S is the distance between sample surface and laser source, Ω_y is the rigid body rotation around the y-axis and ε_{xx} is the strain along the x-axis [120]–[122]. In order to isolate the strain term ε_{xx} from the rigid body motions, two equal, but opposite, illumination angles (two cameras under angles $\pm\theta$) are used, and the difference between the two speckle displacements (ΔA_x) during tension can be estimated by

$$\Delta A_x = A_x(-\Theta) - A_x(\Theta) = 2L\varepsilon_{xx}\tan\Theta + 2a_z\sin\Theta \tag{5.4}$$

Which shows that it is only depends to ε_{xx} and a_z.

In micro tensile test displacement along z-axis, a_z, is approximately zero, so the true strain on the sample along the x-axis can be calculated by

$$\varepsilon_{xx} = \frac{\Delta A_x}{2L \tan \Theta} \tag{5.5}$$

It should be noted that the true strain obtained by this method is valid until the UTS.

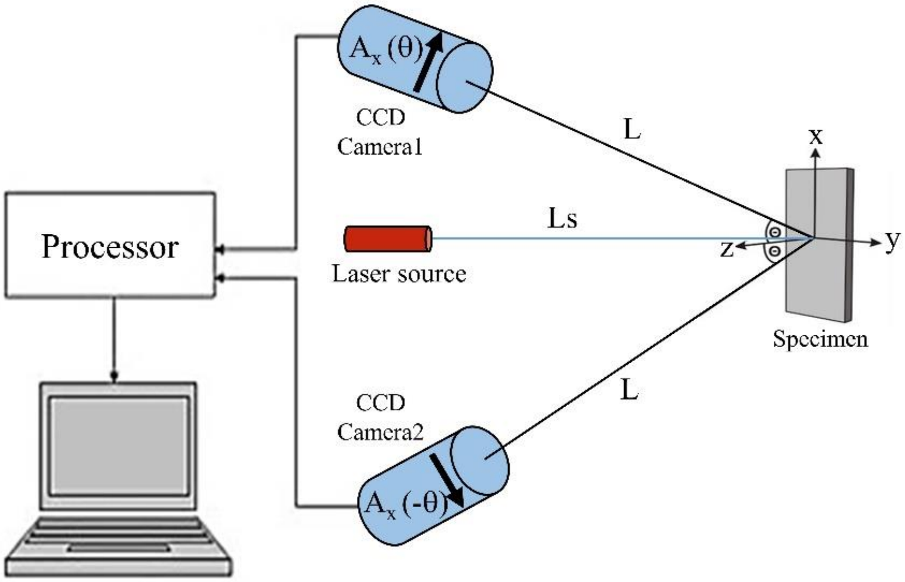

Fig. 12: Experimental set-up for evaluation of the strain measurement by using laser speckle method.

Tensile tests were performed with a strain rate of 10^{-3}/s using a miniaturized tensile machine with a load cell capacity of 2 kN equipped with non-contacting laser speckle sensors based on the correlation technique (Fig. 13a) [119]. Due to the limited size of the HPT processed discs (diameter of 8 mm), miniaturized tensile samples were prepared by using special cutting tools of electro discharge machining. Dumbbell shaped samples with a cross section of 0.75 mm × 0.45 mm and a gauge length of 2.5 mm were used for tensile tests (Fig. 13b).

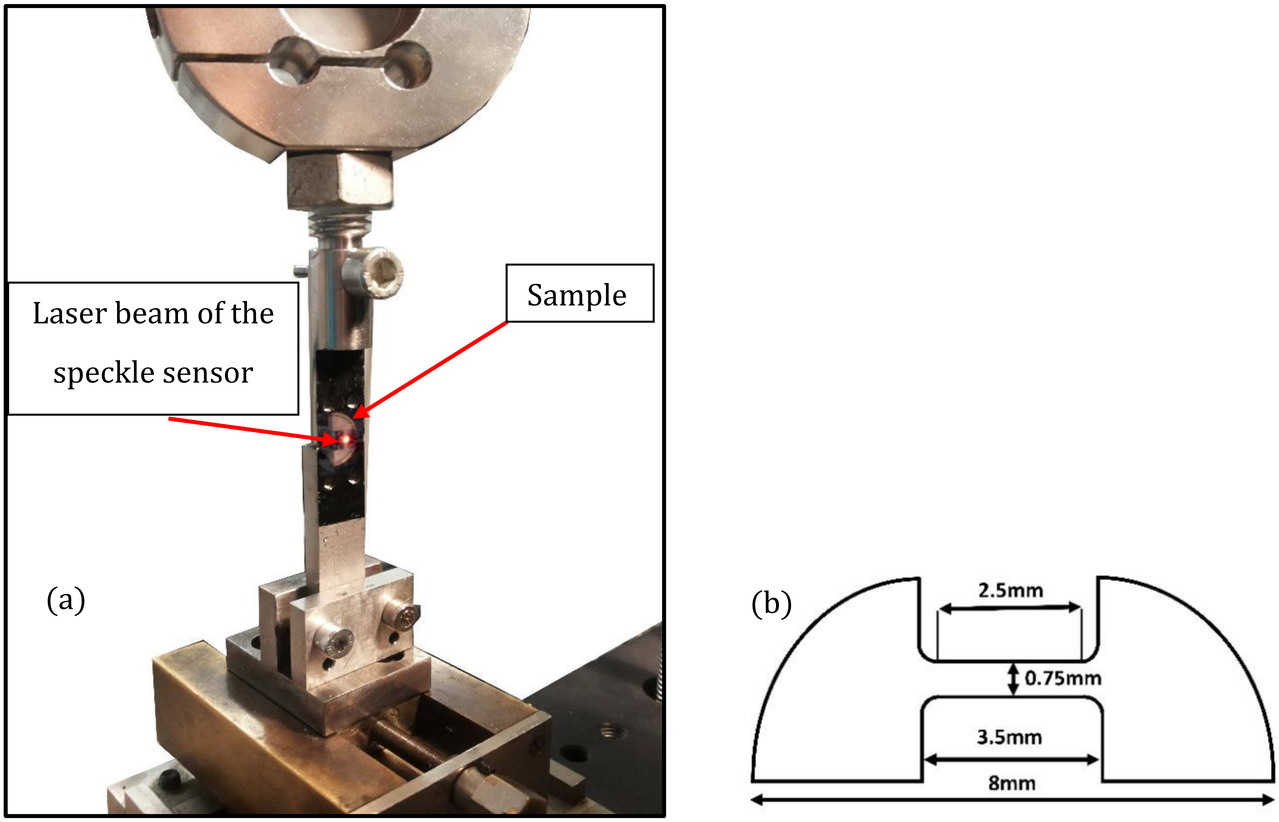

Fig. 13: (a) Experimental set-up of micro tensile test: the dumbbell shaped sample mounted by four pins and incident laser beam of the speckle sensor, (b) Schematic of tensile samples.

5.2.5. Microhardness Vickers test

The microhardness Vickers test can be used for all metals and the hardness Vickers number (HV) is determined by the ratio of the load applied to the surface area of the indentation (F/A), where the load is in kilograms-force and the surface area of the indentation is in square millimeters. Therefore, the unit of the microhardness Vickers will be kilograms-force per square millimeter (kgf/mm^2). It should be noted that this area is not the area normal to the force, so is not pressure. The indenter tip used for the microhardness Vickers test is usually made of a diamond in the form of a square-based pyramid and an angle of 136 degrees between opposite faces [123], [124], as seen in Fig. 14.

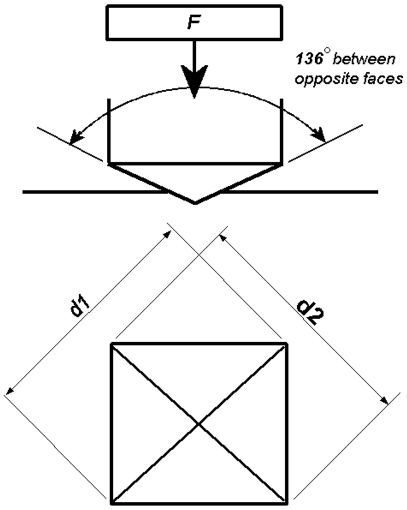

Fig. 14: Schematic of Vickers hardness test.

As already mentioned the hardness Vickers number (HV) is defined as

$$HV = \frac{F}{A} \tag{5.6}$$

Where, the surface area of the indentation is calculated by using following relation

$$A = \frac{d^2}{2sin\ (\theta/2)} = \frac{d^2}{2sin\ (136/2)} \tag{5.7}$$

Finally, the hardness Vickers number can be approximated as

$$HV = \frac{2Fsin\ (136/2)}{d^2} \approx \frac{1.8544F}{d^2} \tag{5.8}$$

Where, F is load applied in Kgf and d is the average length of the two diagonals (d1 and d2) in mm, which the length of the d1 and d2 of the impression made on the surface of the material after removal of the indenter can be measured by the light microscope. For converting a Vickers hardness number to SI units the obtained value is multiplied by 9.807 (which is the standard gravity).

In the present work, microhardness tests were carried out by Vickers indenter seen in Fig. 15 with a load of 0.2 Kgf and a hold time of 10 s on the CG and UFG Ti-45Nb samples as well L605 alloy.

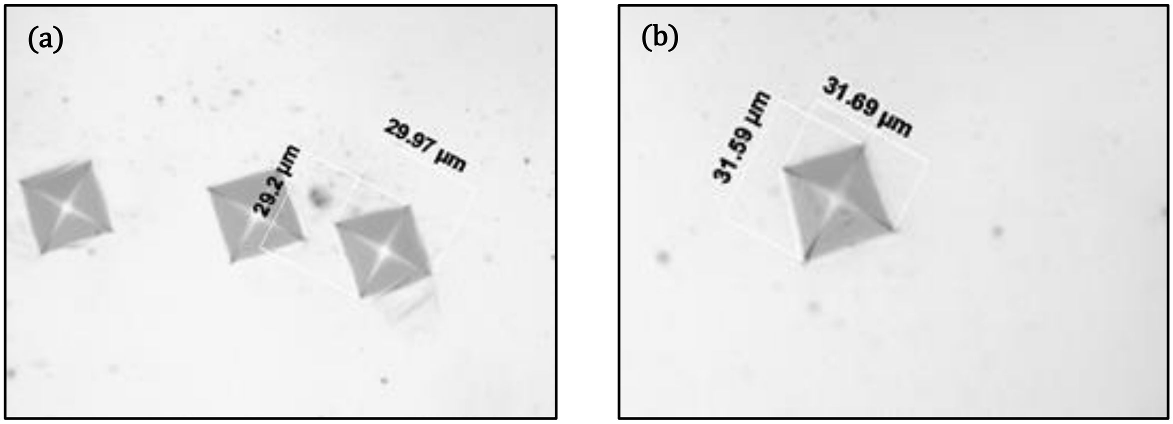

Fig. 15: Optical microscopy images of indents made by Vickers indenter on (a) longitudinal and (b) transversal cross sections of L605 samples.

5.2.6. Microstructural investigations by OM, TEM and SEM

In the present work, optical, scanning and transmission electron microscopy methods (OM, SEM, TEM) were used for microstructural investigations of the initial and HPT Ti-45Nb as well as L605 samples. TEM investigations were conducted by using a transmission electron microscope type FEI Technai F 20. SEM method was used to reveal the microstructure and grain size distribution of transversal and longitudinal cross sections of the Ti45Nb and L605 alloys with a scanning electron microscope type FEI Quanta 200 FEG by using Electron backscatter diffraction (EBSD) technique.

5.2.7. Principles of ultrasonic fatigue

Ultrasound wave with frequencies of above 20 kHz which is considered as the limit of human hearing, can be generated by piezoelectric materials, converting an electric field to a stress field. In ultrasonic fatigue test, usually, a wave with the large displacement amplitude is generated in a resonant mode, which is needed to cause fatigue in materials [125], [126]. In this testing system a sound wave is generated, using an ultrasonic transducer and amplify by horn and finally emitted into the bulk specimen or specimen holder and travels from one side to the other at a specific velocity corresponding to the Young's modulus and density of the material, and the geometry of specimen. The ultrasound waves entering the bulk specimen, or specimen holder in case of miniaturized sample, in the opposite direction are reflected from the end of the specimen with the phase changes by π (180 degree). These two waves have equal amplitude and construct a standing wave (stationary wave) causing the resonance in the specimen on condition that the bulk specimen or specimen holder length is exactly half of the wavelength of the ultrasound wave. In the following an example of the uniform resonant bar is given providing the basic concepts of ultrasonic fatigue test.

When a disturbance on the surface of a body occurs, this disturbance will be propagated through the body and follows the following wave equation. With considering a straight bar having a uniform diameter the simplified wave equation will be as:

$$\frac{\partial^2 u_{(x)}}{\partial t^2} = \frac{4\pi f^2 E}{\rho} \frac{\partial^2 u_{(x)}}{\partial x^2} \tag{5.9}$$

Where, u(x) is the displacement amplitude distribution along the specimen length which can be determined by solving this differential equation; f is resonance frequency; ρ is density of the specimen; E is the dynamic Young's modulus of the material.

The boundary conditions are as below

$$u_{(0)} = u_0 \quad , \quad \frac{\partial u_{(0)}}{\partial x} = 0 \tag{5.10}$$

Finally, by solving differential equation (5.9), the displacement amplitude distribution at a point *x*, *u(x)*, can be obtained:

$$u_{(x)} = u_0 \cos(2\pi f \sqrt{\frac{\rho}{E}}\,\mathrm{x}) \tag{5.11}$$

The strain distribution, *ε(x)*, along the bar will be the derivative of the displacement amplitude with respect to distance:

$$\varepsilon_{(x)} = \frac{du_{(x)}}{dx} = -u_0 2\pi f \sqrt{\frac{\rho}{E}} \sin(2\pi f \sqrt{\frac{\rho}{E}}\,\mathrm{x}) \tag{5.12}$$

The resonance length, *L*, is determined by the first point of *x*, where ε (*x*) =0, i.e.

$$\varepsilon_{(L)} = \frac{du_{(x)}}{dx} = -u_0 2\pi f \sqrt{\frac{\rho}{E}} \sin(2\pi f \sqrt{\frac{\rho}{E}} L) = 0 \tag{5.13}$$

Consequently

$$L = \frac{1}{2f} \sqrt{\frac{E}{\rho}} \tag{5.14}$$

Usually, the resonance length is determined by this equation. In this study a bar shaped specimen holder of high strength Ti-alloy with a resonance length of 128 mm was used for fatigue testing. Above relations show that the distribution of displacement and strain vary sinusoidally along the system with the maximum strain being in the midsection of the specimen holder (Fig. 16).

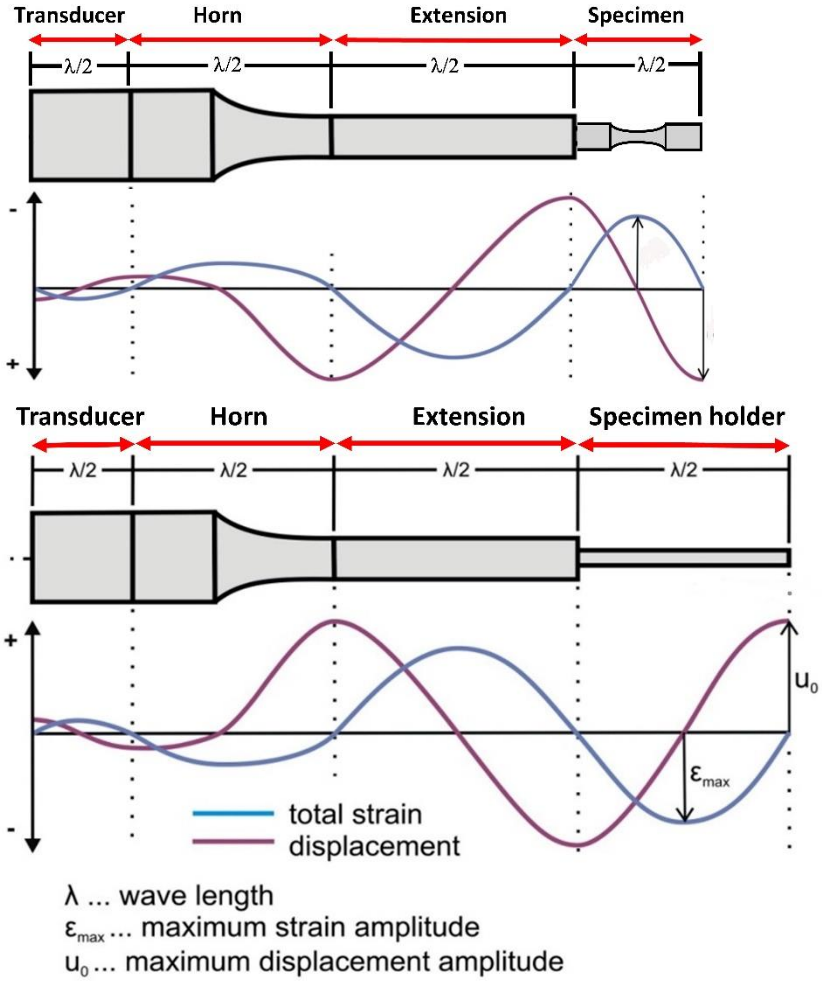

Fig. 16: Schematic of principle of ultrasonic fatigue technique and distribution of strain and displacement for bulk and miniaturized specimen.

The stress (σ) distribution along the bar is obtained by an elastic conversion of the strain distribution:

$$\sigma_{(x)} = E \, . \, \varepsilon_{(x)} \tag{5.15}$$

The distribution of displacement and strain varies sinusoidally along the system with the maximum strain being in the midsection of the specimen holder.

5.2.8. Ultrasonic resonance fatigue testing system for miniaturized specimens made of CG and UFG Ti45Nb alloy

Since skeletal implants are frequently exposed to long-term cyclic loading [18], our investigations were concentrated on the high cycle fatigue regime up to 10^9 cycles. A special testing system composed of an ultrasonic resonance fatigue testing system working at 20 kHz in combination with a special experimental set up developed for testing of miniaturized specimens [41], was used to perform fatigue tests on CG and UFG Ti45Nb alloy (Fig. 17). In this set-up, a bar shaped specimen holder of high strength Ti-alloy with a cross section of 20 mm × 8 mm and a resonance length of 128 mm containing a through hole with a diameter of 2 mm in the midsection was used for fatigue testing. The miniaturized specimens were aligned and glued carefully over the notch of the holder parallel to the loading direction by using a cyanide-acrylate adhesive. The gauge section of the miniaturized specimen across the hole is freestanding in this location. Strain measurements were performed by using miniature strain gauges. The velocity of vibration at the end of the sample holder was measured by using a laser Doppler Vibrometry (LDV) during the loading. During testing, a video camera attached to a light microscope was used to monitor the plane surface of the specimens (Fig. 18). This allowed recording the entire fatigue process and determination of the number of loading cycles (N_f) to failure. The magnification of the microscope and the video system could be set up to 1000× with a resolution of about ±5 µm. Tests were performed at room temperature with additional cooling of the specimen by pressurized dry air. Control temperature measurements were performed using an infrared thermometer with a spot size of about 0.6 mm on the surface of specimens to ensure the room temperature testing conditions.

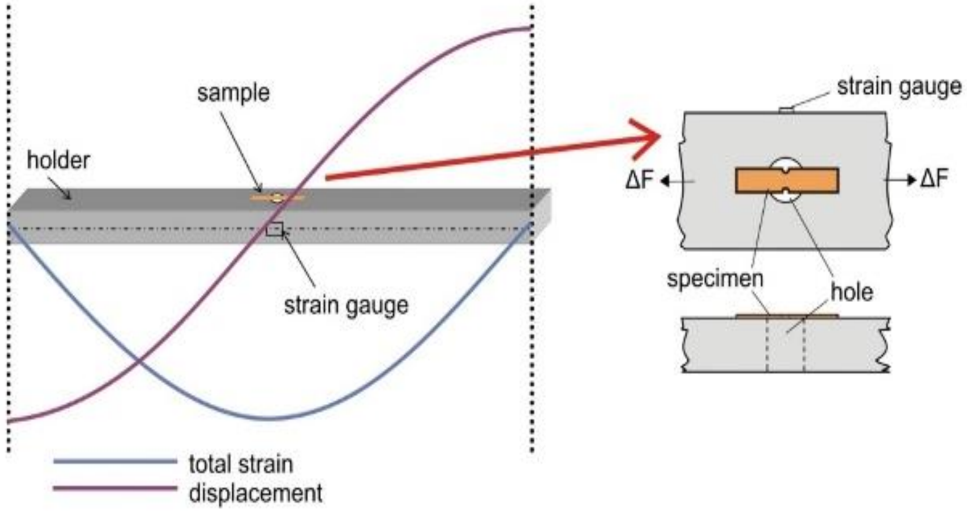

Fig. 17: Schematic of principal of ultrasonic fatigue technique and experimental set up for miniaturized specimens under fully reversed loading condition (R=-1), frequency 20 kHz.

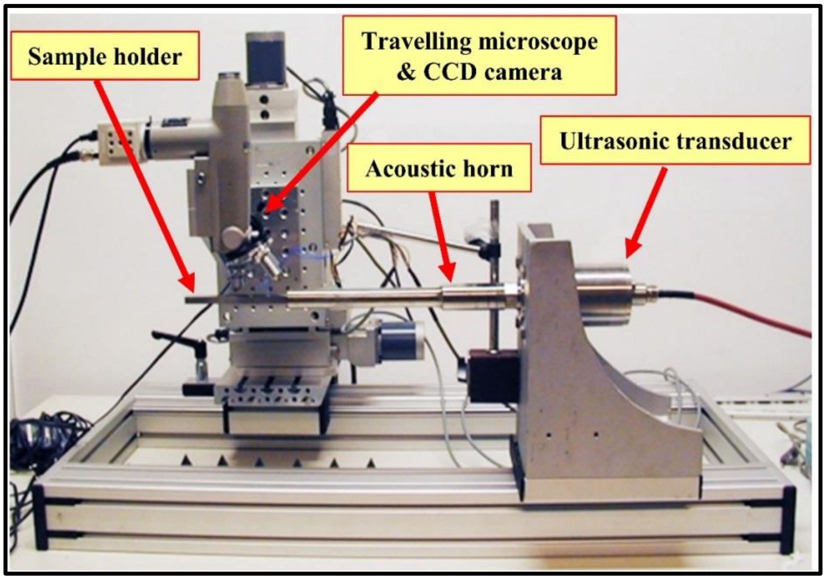

Fig. 18: Ultrasonic resonance fatigue testing set-up for miniaturized specimens.

5.2.8.1. Geometries of miniaturized double-edge notched and hourglass fatigue specimens

Due to the limited size of the HPT processed discs (diameter of 8 mm), miniaturized fatigue samples were prepared by using special cutting tools of electro discharge machining. Fatigue experiments on the CG material were conducted by using hourglass and double-edge notched specimens and the UFG material was tested by using the hourglass sample geometry with the dimensions given in Figs. 19a and b. Both sample series had a gauge section of about 350 µm and a thickness of 0.2 mm. The UFG samples were cut at the radius of about 2 mm from the center of the HPT discs to assure a similar microstructure at the gauge section as indicated with blue color in the disc illustrated in Fig. 11. All samples were mechanically thinned and fine polished with diamond paste to remove possible damages and to obtain smooth surfaces.

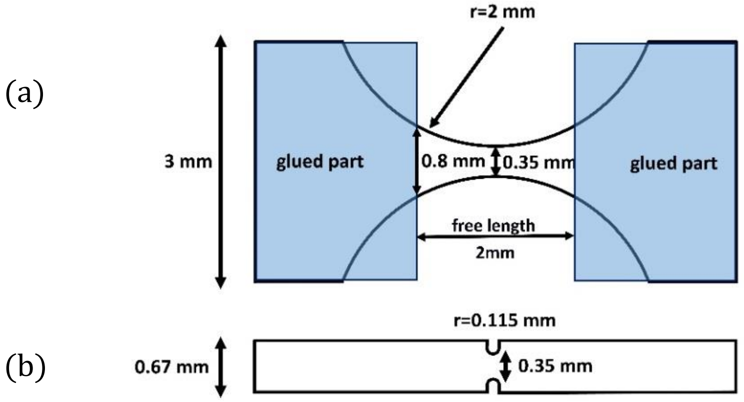

Fig. 19: Schematic of fatigue samples (a) hourglass, (b) double-edge notched.

5.2.8.2. Strain and stress calibration

Strain and displacement measurements were used for the calibration of the fatigue experimental set-up and determination of the relationship between the strain values at the plane surface of the test specimens to that of the specimen holder. Strain gauges were attached to the gauge section of the specimen and to the site of maximum strain on the side face of the specimen holder. Due to the small geometries of the notched and hourglass shaped samples with thickness of 200 µm and gauge section of about 350 µm direct strain measurements by application of commercially available strain gauges was not possible. Therefore, strain measurements were performed by using calibration hourglass samples with the same thickness and a width of about 600 µm in the gauge section. The displacement /strain amplitude was increased stepwise and the ratio of the strain value at midsections of the miniaturized sample to the holder was determined. The experimental strain ratio ($R_E = \varepsilon_{sample}/\varepsilon_{holder}$) was determined by linear regression as shown in Fig. 20. The obtained value of 2 which is lower than the theoretical $K_t = 2.73$ (for a rectangular bar of 20 mm with a through hole of 2 mm) corresponds to the actual increase of stress on the free standing samples glued to the holder across the hole.

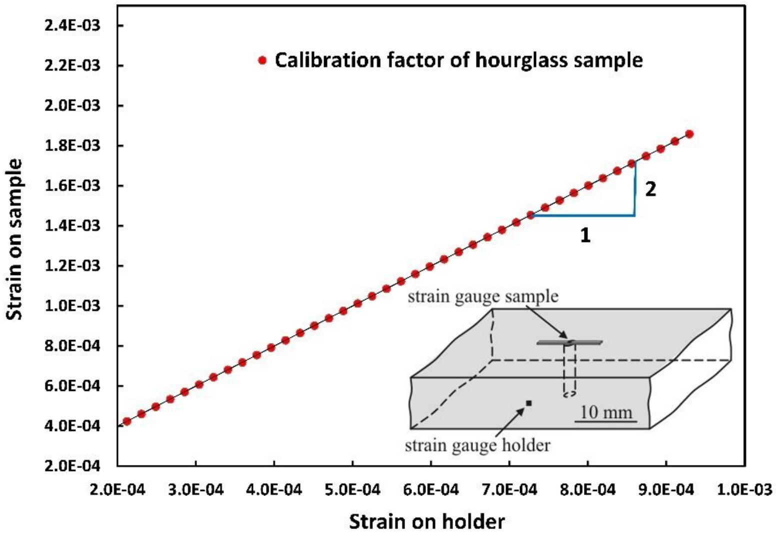

Fig. 20: Calibration curves for determination of strain in the miniaturized samples.

The corresponding stress amplitude of the specimens was calculated based on the experimental calibrations and Finite Element Analysis (FEA). The experimental stress value was determined by using the strain measured at the mid-section of the holder at each stress amplitude, the obtained strain calibration factor and the theoretical stress concentration factors for each sample geometry. Under the assumption of preliminarily elastic deformation of the specimen at HCF region Hooke's equation was used:

$$\frac{\Delta\sigma}{2} = R_E . K_t . E . \left(\frac{\Delta\varepsilon}{2}\right)_{holder} \tag{5.16}$$

where E is the elastic modulus of the Ti-45Nb alloy, $\left(\frac{\Delta\varepsilon}{2}\right)_{holder}$ is the strain at the side face of the specimen holder, K_t is theoretical net stress concentration factor according to Peterson [127] and R_E is the calibration factor measured by the strain gauges.

5.2.8.3. Finite Element Analysis of the miniaturized specimens

Finite element analysis (FEA) was performed by using ANSYS software in order to calculate the distribution of strain and stress in the miniaturized samples. The mesh size and geometry of the models was selected in a manner to define the contours of the miniaturized samples properly. Thereby, the mesh was refined in the region around a notch wherever this was necessary. FE models were constructed for three geometries including the **calibration sample**, **hourglass shaped** and **double edge notched samples** with details listed in Table 16 and Figs. 19a and b. Harmonic analyses were conducted by adjusting the sinusoidal loads in order to fit the measured displacement amplitude at the end of the sample holder which corresponds to the strain amplitude at the midsections of the holder.

5.2.9. Ultrasonic resonance fatigue testing system for bulk specimens

To study the effect of sample size on the fatigue response and to determine the notch sensitivity of the Ti-45Nb and L605 alloys, bulk samples with different notch geometries were prepared.

Fatigue tests on the bulk Ti-45Nb and L605 samples were performed using the ultrasonic resonance fatigue testing system described before. The strain amplitude was measured by the strain gauges placed in the midsection of the smooth samples and the acoustic horn from which stress/strain calibration curves were obtained. The displacement at the end of the samples was also measured by means of laser vibrometry. The stress amplitude was determined based on validation of Hooke's law in the high cycle fatigue regime assuming a Young's Modulus of 65.4 GPa for Ti45Nb and 242 GPa for L605.

The experimental set-up of the ultrasonic resonance fatigue testing system shown in Fig. 21 was used for testing of bulk samples. An essential feature of this testing system is using water cooling besides compressed air cooling to keep the testing temperature constant and prevent heating of samples especially at high stress amplitude applied to high strength materials.

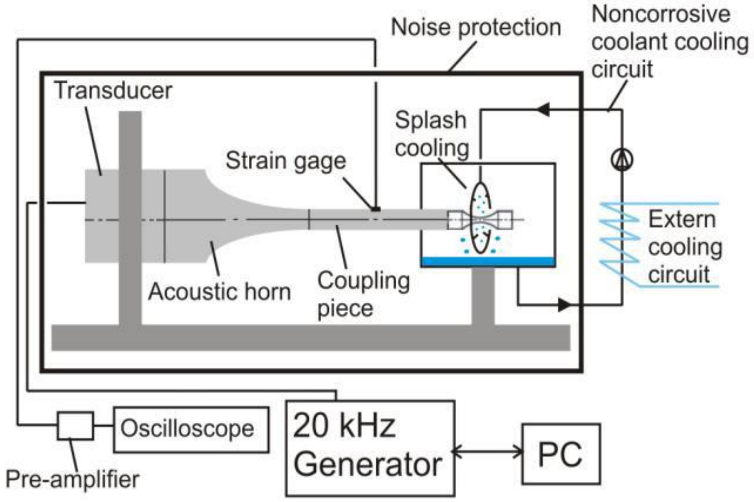

Fig. 21: Ultrasonic resonance fatigue testing set-up for bulk specimens.

5.2.9.1. Sample geometries with different shapes of circumferential notches

The resonance dog-bone Ti-45Nb and L605 samples had a total length of 43 mm and 59.60 mm, respectively, shoulder diameter of 11 mm and a midsection diameter of 4 mm (Fig. 22a). The geometry of the dog-bone shaped samples with the total length of the sample corresponds to the longitudinal half-wave of Ti-45Nb and L605 materials at 20 kHz and is presented in Figs. 22b and c. In addition to the smooth samples, two types of circumferential blunt and sharp notches were introduced in the midsection of the samples in order to investigate the fatigue notche sensitivity of the alloy as presented in Figs. 23a and b.

Fig. 24 shows the profile pictures of U-shaped and V-shaped circumferential notches. The dimensions of the notches are given in Table 8. L605 specimens were finished up by two different types of surface treatment processes including mechanical polishing and electropolishing. Mechanically polished samples were ground by P600, P800, P1200 and P2500 grit sandpapers for about 5 minutes and finally in the last step polished by premium SiC abrasive P4000 for at least 10 minutes. Samples were cooled and polished with a minimum force and velocity to reduce surface effects due to polishing. The electro-polished L605 samples were prepared by Cortronik GmbH, Rostock-Warnemünde, Germany. The electrolyte used for electropolishing process was made by mixing 60% Ethylene Glycol and 40% Phosphoric Acid (85%). Table 9 shows different parameters used for the electropolishing.

Table 8. Dimensions of the U-shaped and V- shaped circumferential notches.

Notch shape	Depth (d) [mm]	Radius (r) [mm]	Angle [°]
U	**3.63**	**0.55**	**-**
V	**3.5**	**0.15**	**60**

Table 9. Different parameters used for the electropolishing process.

Electropolishing Parameters	
Temperature (°C)	25 °C
EP Time (min.)	3 min.
Cathode	Ti
Anode	L605
Electrode Distance (cm)	2.54 cm
Surface Preparation	600 grit
Current (A)	0.35 A

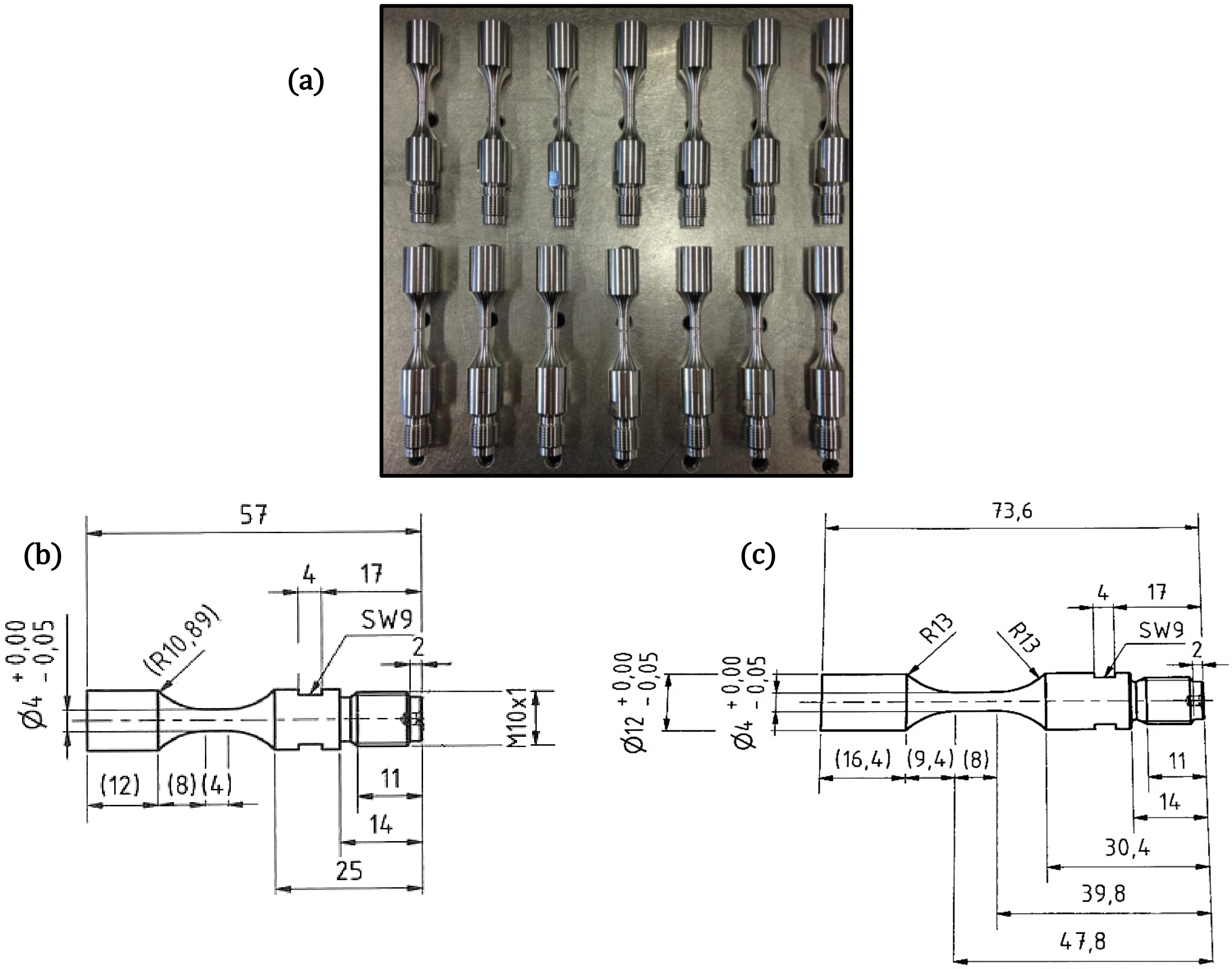

Fig. 22: (a) Bulk fatigue samples, Geometry of the smooth bulk resonance (b) Ti-45Nb, (c) L605 samples.

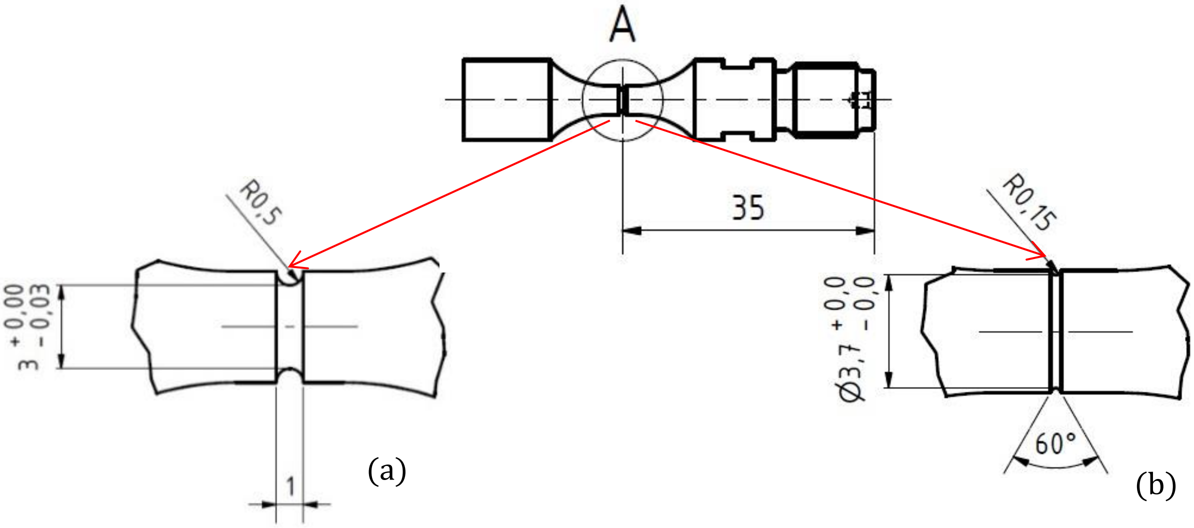

Fig. 23: Geometries of the (a) U-shaped and (b) V- shaped circumferential notches.

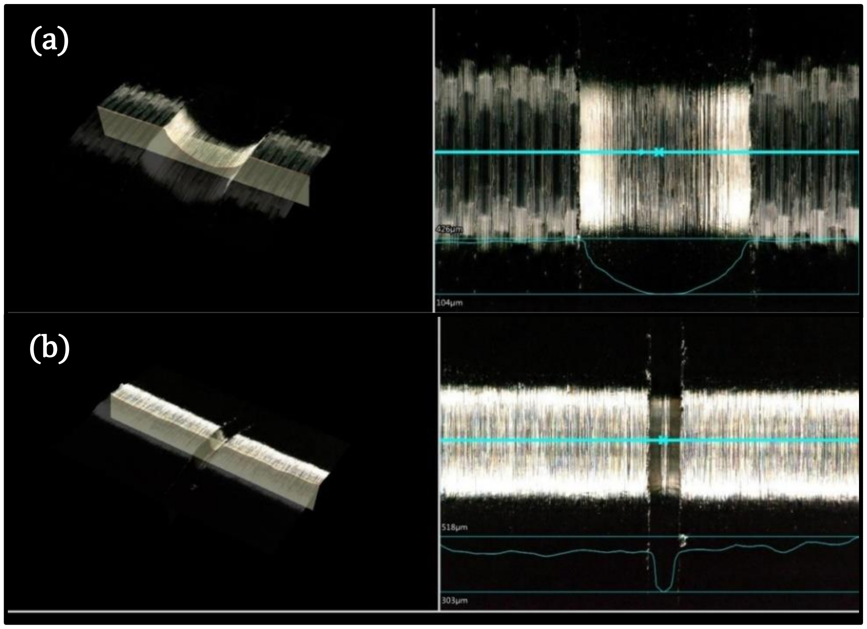

Fig. 24: Profile pictures of (a) U-shaped and (b) V- shaped circumferential notches.

5.2.9.2. Finite Element Analysis of the bulk Ti45Nb specimens

Harmonic analyses were performed for bulk Ti-45Nb specimens with and without notch in order to determine the stress concentration factors. Thereby, the displacement amplitudes were adjusted to fit the values measured by laser Doppler vibrometry and by strain gauges.

Chapter 6: Results and Discussion

In this chapter, the results related to the investigations of microstructural and static mechanical properties of the initial and HPT Ti-45Nb as well as L605 samples will be presented. Furthermore, the relevant parameters that describe the fatigue behaviour of the Ti-45Nb and Co-Cr L605 alloys are identified, discussed and compared with previous works.

6.1. Microstructure and texture

Fig. 25 presents the phase compositions of the Ti-45Nb samples at the initial state and after HPT deformation at 4 GPa hydrostatic pressure and by 5 rotations. The XRD results confirm that both initial CG and UFG Ti-45Nb samples consist of a single β-phase and no phase transformation occurred during HPT processing (Fig. 25).

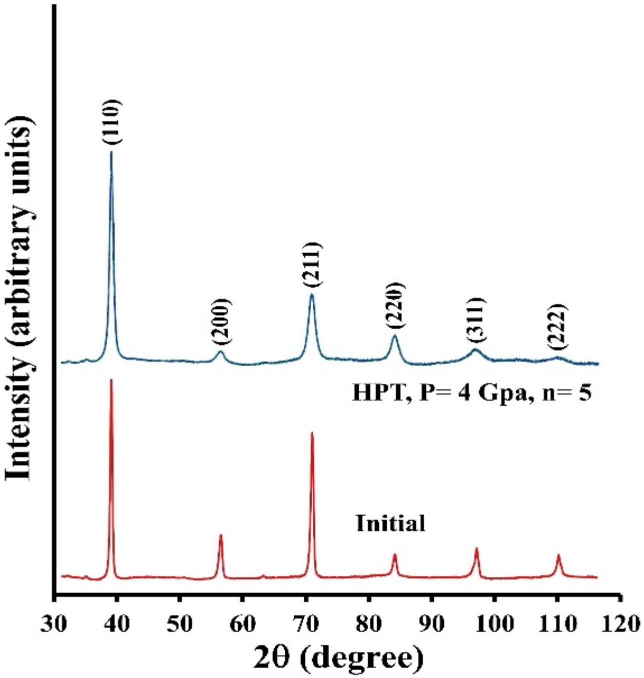

Fig. 25: XRD diffraction patterns for the initial state and HPT (n=5, p=4 GPa) samples.

Fig. 26 presents the phase compositions of L605 alloy which consists of a single γ- face-centered cubic (fcc) phase.

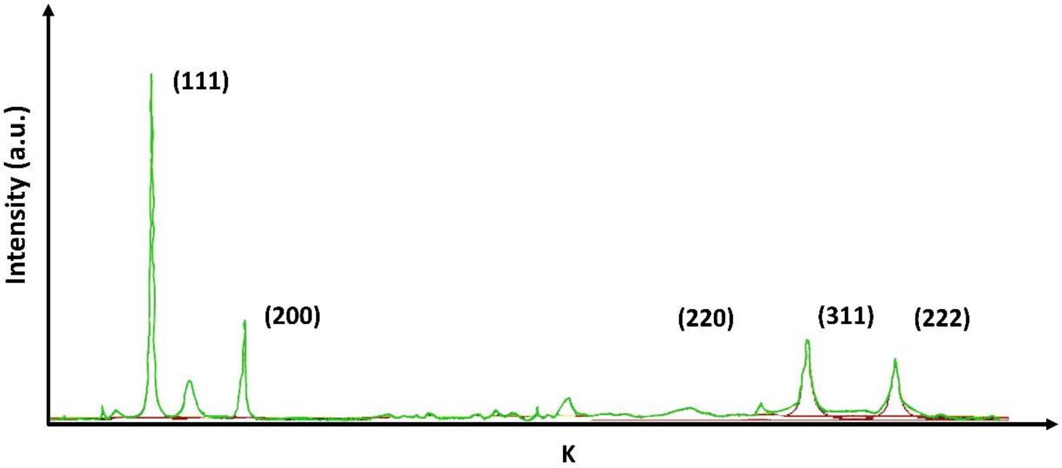

Fig. 26: XRD diffraction patterns (intensity as a function of diffraction vector, K) for the L605 sample.

To measure the dislocation densities of Ti-45Nb samples before and after HPT processing, X-ray line profiles were also evaluated using the convolutional multiple whole profile (CMWP) procedure. The obtained results are presented in Table 10.

Table 10. The measured dislocation density for the CG and UFG Ti-45Nb samples.

Ti-45Nb Samples	**Dislocation density [1/m^2]**
CG	**1.35E+15**
UFG	**3.30E+15**

Fig. 27a shows the grain size distribution and the texture of the initial Ti-45Nb alloy normal to the axis of the bar (OM). TEM dark and bright field images of the microstructure of Ti-45Nb after HPT deformation and the corresponding selected area electron diffraction (SAD) pattern are shown in the Figs. 27b, c and d. HPT deformation of the initial sample with an average grain size of about 20 µm resulted in an ultrafine grained microstructure with grain size of less than 100 nm. The continual diffraction rings of the β-phase shown in Fig. 27c confirm the results of XRD measurements.

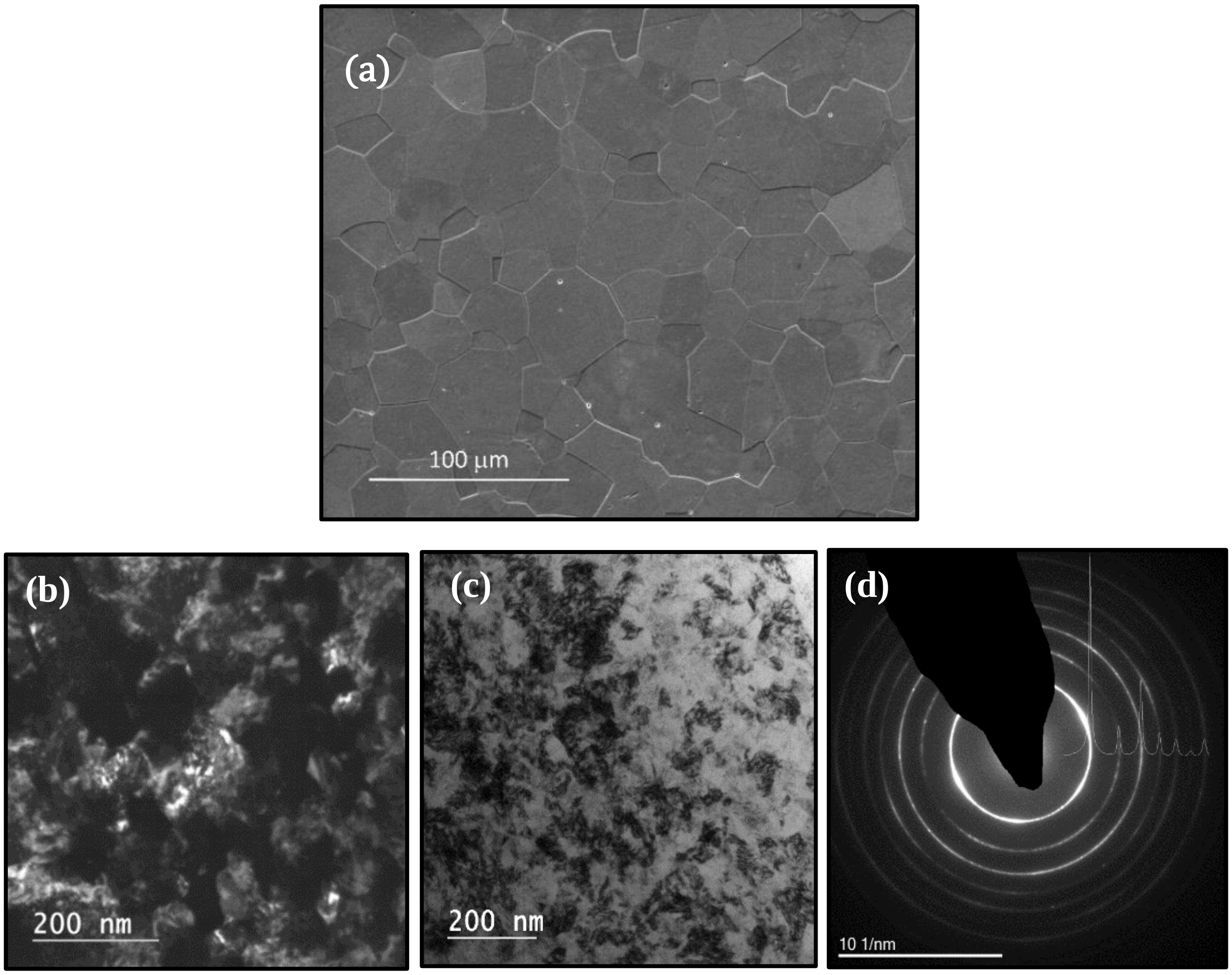

Fig. 27: Microstructure of Ti-45Nb material, (a) conventional grained initial alloy, b, c and d Ultrafine grained material (UFG) processed by HPT with P = 4 GPa, n= 5; (b, c) dark and bright field TEM images and the (d) corresponding selected area electron diffraction (SAD) pattern of the beta phase.

SEM method was used to reveal the microstructure and grain size distribution of the Ti45Nb and L605 alloys. The microstructures of the transversal and longitudinal cross sections of the Ti45Nb and L605 samples are presented in the electron backscatter diffraction (EBSD) images in Figs. 28, 29.

Fig. 28a shows a dominant 101 texture in the transversal direction of the rod Ti45Nb material.

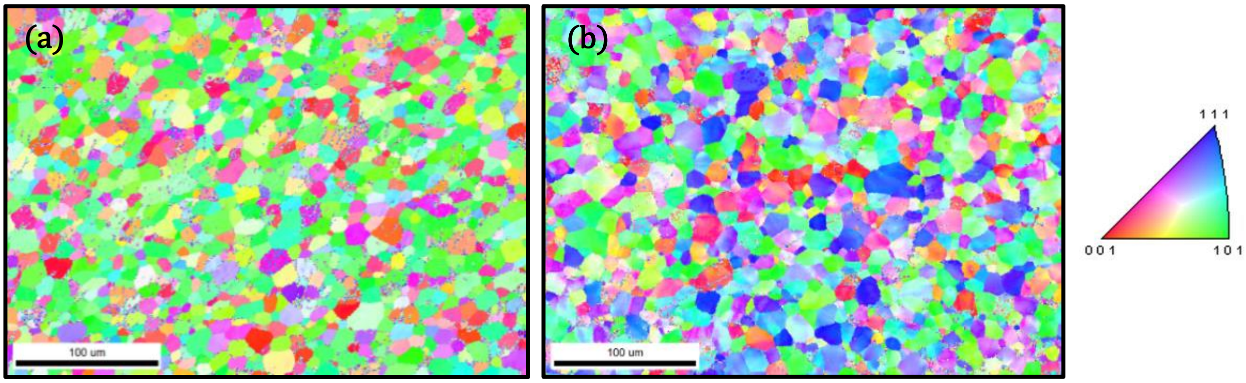

Fig. 28: EBSD analysis: IPF maps of Ti45Nb rod (a) transversal (b) longitudinal views.

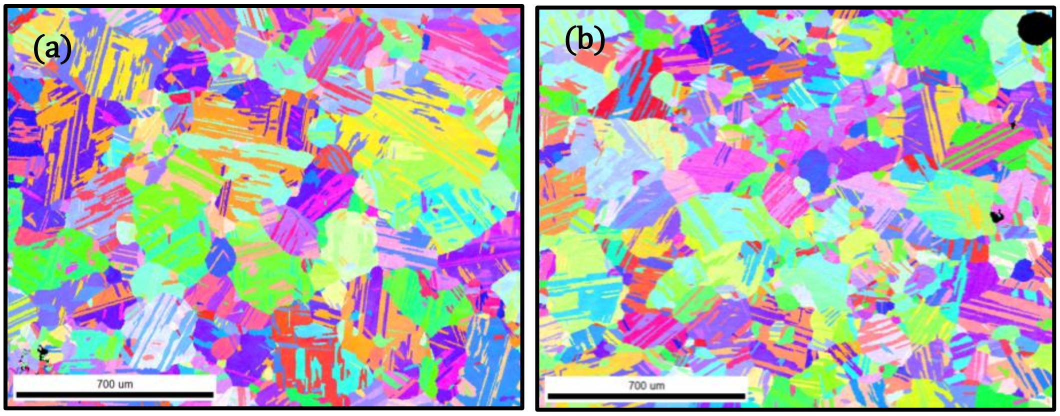

Fig. 29: EBSD analysis: IPF maps of L605 rod (a) transversal (b) longitudinal views.

The grain and grain boundary maps of L605 alloy without and with twins, respectively, as well the plots of grain size (diameter) distribution are presented in Figs. 30, 31.

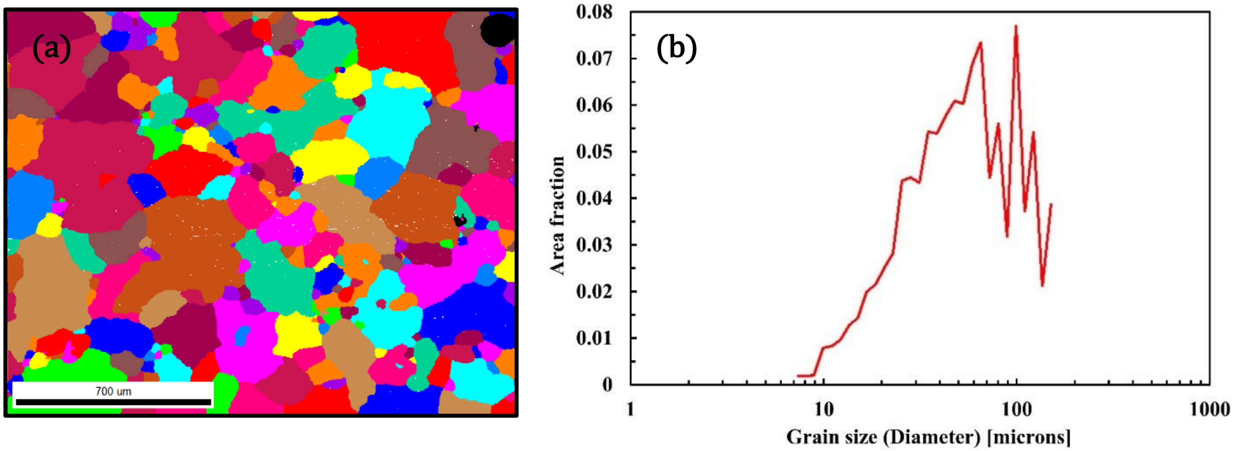

Fig. 30: (a) Grain map of L605 alloy without twins, (b) grain size distribution.

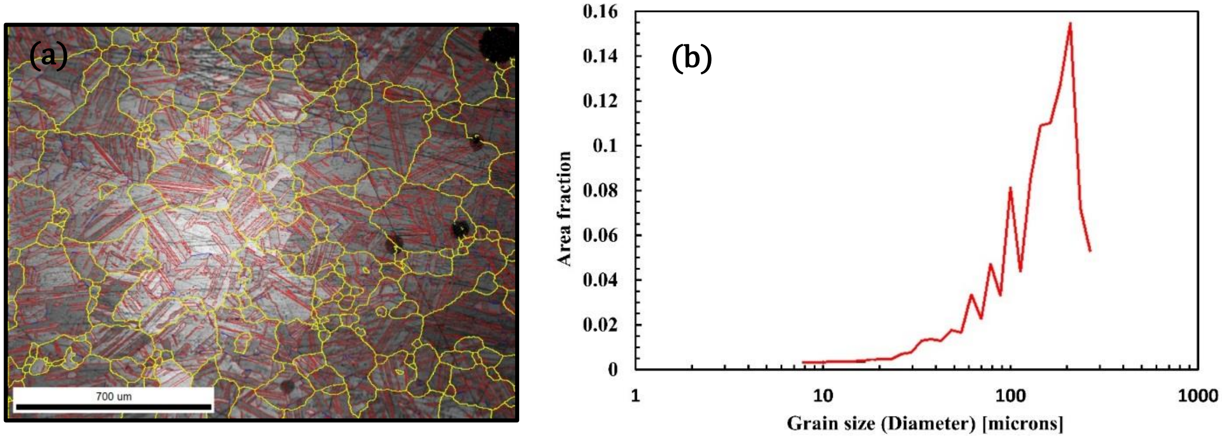

Fig. 31: (a) Grain boundary map of L605 alloy with twins, (b) grain size distribution.

As seen in Figs.30 b and 31 b, the area fraction as a function of the grain size diameter is depicted in a semi logarithmic plot. The average grain size of L605 alloy based on the grain map without twins and grain boundary map with twins is between 75 µm - 203 µm.

6.2. Mechanical properties

Typical nanoindentation load displacement curves for Ti-45Nb alloy obtained for the CG and UFG materials after different stages of HPT processing are presented in Fig. 32. The corresponding values of elastic modulus and nanohardness are demonstrated in Figs. 33 a and b showing the evolution of these values with increasing degree of shear deformation. The results show that the value of Young’s modulus after HPT deformation is only slightly higher than the value measured for the CG samples, while a considerable increase of nanohardness from 1.42 for CG sample to 2.42 for UFG material after 5 rotations is observed.

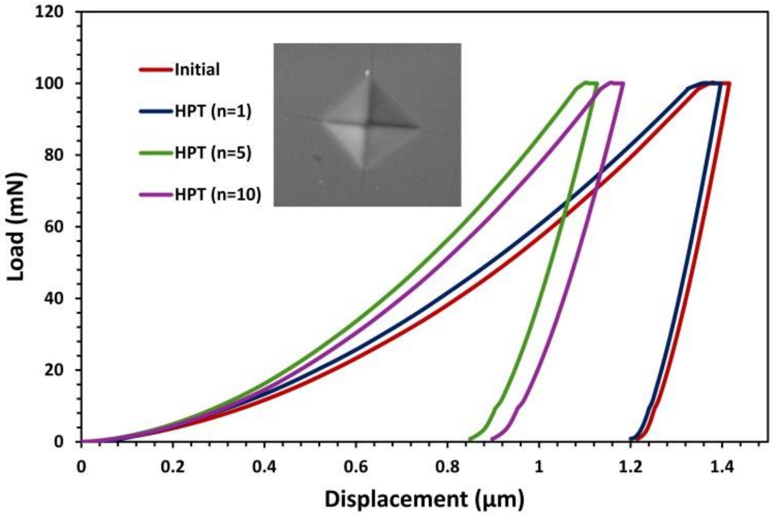

Fig. 32: The plot of load versus displacement curves with F_{max} =100 mN and Vickers indenter. Inset Fig. shows typical indent made by Vickers indenter.

The results show that HPT processing induced a significant increase in the strength of the Ti-45Nb alloy while maintaining the Young's modulus at the low level of the initial material. With regard to the obtained values of Young's modulus and nanohardness for the HPT processed alloy at three different number of rotations (N = 1, 5, 10) and 4 GPa hydrostatic pressure and since the increasing of the tensile strength and nanohardness are rather saturated after HPT of 5 rotations (Fig. 33a and b) for this study the HPT Ti-45Nb material processed under 5 rotations was selected for the fatigue investigations. A summary of the nanoindentation results including the values of Young's modulus and nanohardness of the Ti-45Nb samples are also presented in Table 11.

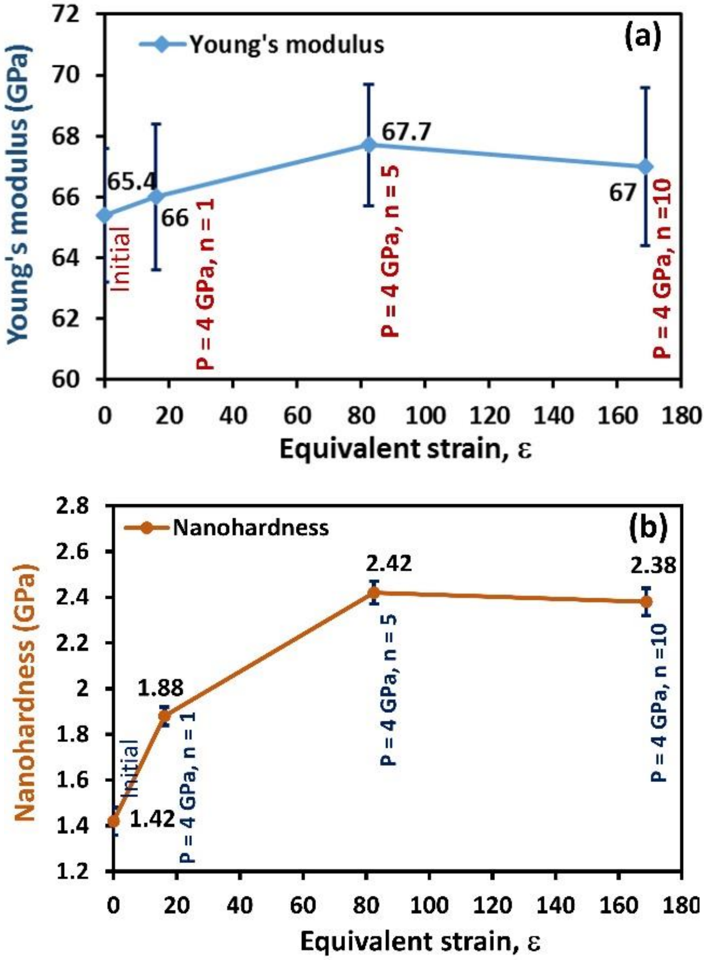

Fig. 33: Nanoindentation results of initial and HPT Ti-45Nb; (a) Young’s modules and (b) Nanohardness values vs. equivalent strain.

Table 11. Summary of the nanoindentation results.

Sample	Young’s modulus [GPa]	Nanohardness [GPa]
Initial	65.4±2.1	1.42±0.02
HPT(n=1)	66±2.2	1.88±0.01
HPT(n=5)	67.7±1.9	2.42±0.02
HPT(n=10)	67±2.9	2.34±0.05

Nanoindentation measurements related to the longitudinal and transversal cross sections of L605 samples were performed with twenty indentations separated by a distance of 50 μm. The indentations were performed on the smooth surface of the polished samples. The average load-displacement curves obtained from the indentation test on L605 alloy for the longitudinal and transversal cross sections are presented in Fig. 34. The corresponding values of elastic modulus and nanohardness are demonstrated in Table 12.

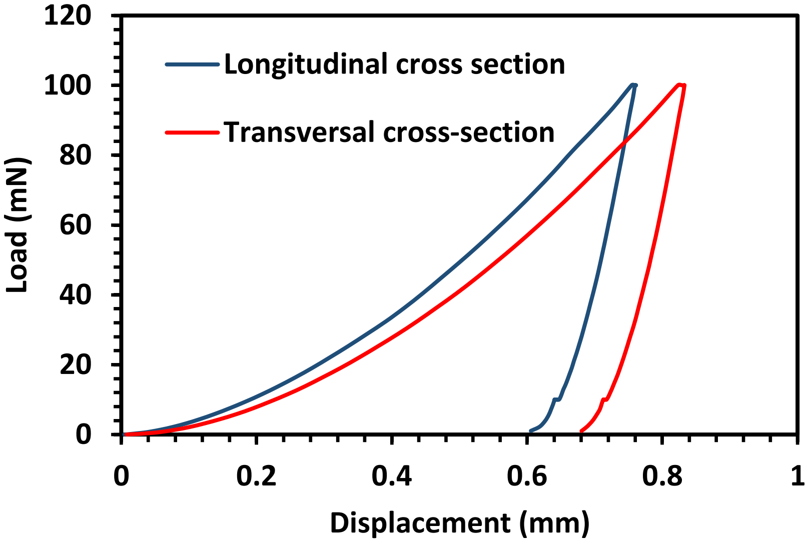

Fig. 34: The plot of load versus displacement curves of longitudinal and transversal cross sections of L605 alloy with F_{max} =100 mN.

Table 12. Nanoindentation results of the L605 samples.

Sample	Young's modulus [GPa]	Nanohardness [GPa]
Transversal cross section	**242.2±2.9**	**3.83±0.14**
Longitudinal cross-section	**243.2±3.7**	**4.75±0.10**

Typical stress-strain curves of the initial and UFG Ti-45Nb samples are presented in Fig. 35 (a).

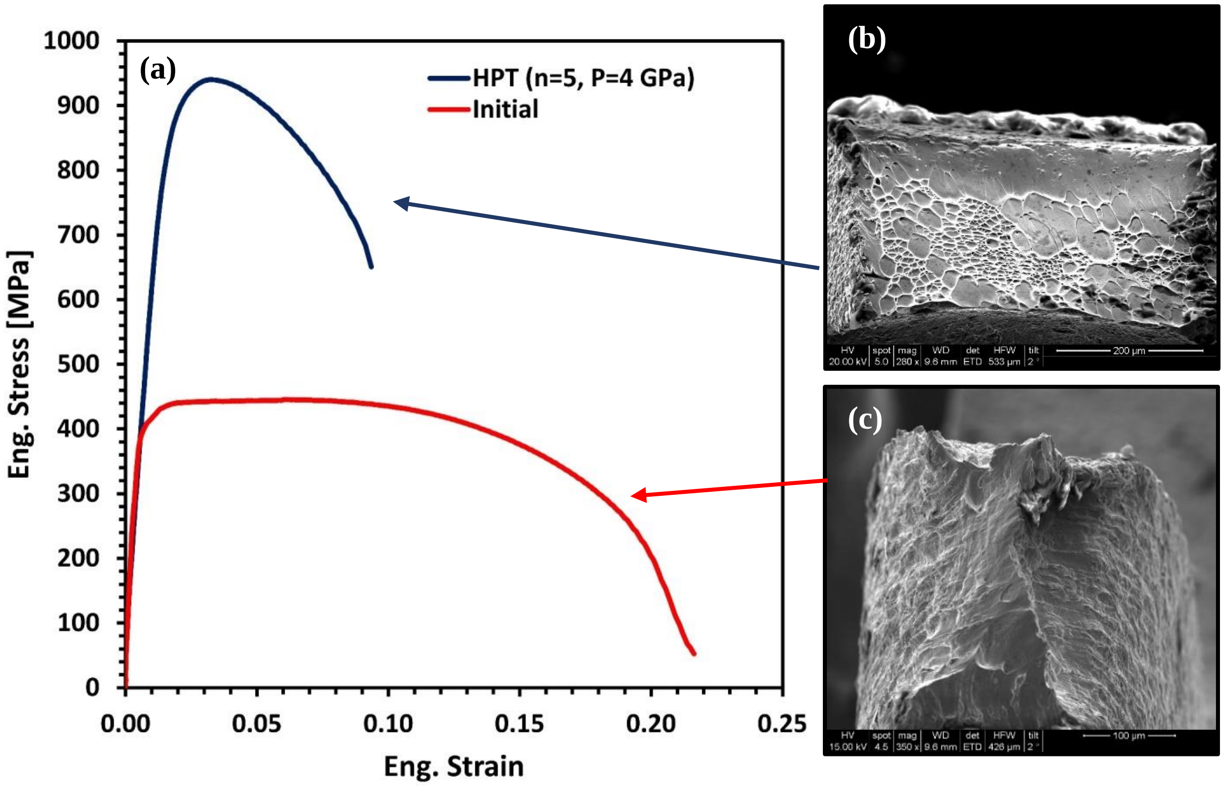

Fig. 35: (a) Stress-strain curves of initial and HPT Ti-45Nb specimens. SEM images of tensile fracture surfaces of (b) HPT and (c) Initial Ti-45Nb specimens.

It can be seen that HPT deformation leads to a strong increase in the ultimate tensile strength about 100 % from 446 MPa for the CG to 940 MPa for the UFG sample. The tensile tests also show a reduction of the fracture strain from above 20% to about 10% after HPT deformation. Reduced gage section of the initial Ti-45Nb tensile test specimen caused by necking can be seen in Fig.35(c).

The results concerning the Ti-45Nb alloy show a significant increase in microhardness from 1.32 GPa for CG sample to 2.04 GPa for UFG material after 5 rotations. Microhardness values on transversal and longitudinal cross sections of L605 alloy were measured as 3.52 GPa and

4.32GPa respectively. Results of microhardness Vickers test of theTi-45Nb and L605 samples are summarized in Table 13.

Table 13. Results of microhardness Vickers test of theTi-45Nb and L605 samples.

Sample	Microhardness[GPa]
CGTi-45Nb	**1.32±0.02**
UFG Ti-45Nb	**2.04±0.05**
transversal cross section of L605	**3.52±0.04**
longitudinal cross section of L605	**4.32±0.05**

A summary of the microstructural and mechanical properties of the initial CG and UFG Ti-45Nb samples and the L605 alloy is presented in Tables 14 and 15.

Table 14. Mechanical properties of the CG and UFG (HPT P=4, N=5) Ti-45Nb specimens.

Sample	Dislocation density [1/m^2]	Young's modulus [GPa]	UTS [MPa]	Yield strength [MPa]	Average grain size [μm]	Nanohardness [GPa]	Fracture strain %
CG	**1.35E+15**	**65.4±2.1**	**446±12**	**430±21**	**20 μm**	**1.42±0.02**	**21.8**
UFG	**3.30E+15**	**67.7±2.1**	**940±14**	**864±25**	**<0.100**	**2.42±0.04**	**9.4**

Table 15. Mechanical properties of the transversal and longitudinal cross sections of L605 alloy.

Sample	Young's modulus [GPa]	Micro Vickers hardness[GPa]	Nanohardness [GPa]	Average grain size [mm]
Transversal cross section	**242.2±2.9**	**3.52±0.3**	**3.83±0.14**	**75-200**
Longitudinal cross section	**243.2±3.7**	**4.32±0.26**	**4.75±0.10**	**75-200**

6.3. Miniaturized Ti-45Nb specimens

6.3.1. Finite element analysis

The ratio of the calculated strains of the sample at different locations to the strain measured in the midsection of the side face of the holder was determined. The calculated strain in the miniaturized samples is also influenced by the geometry of the experimental set-up. In particular, stress concentrations are introduced by the hole in the midsection of the holder across which the samples are stretched due to attachment to the ambient periphery of the hole. Since the direction of loading is along the y-axis of sample and holder, particular interest was devoted to the strain component $\boldsymbol{\varepsilon}_{\mathbf{yy}}$ which was also measured by strain gauges. Furthermore, the simulations revealed that the value of the strain component $\boldsymbol{\varepsilon}_{\mathbf{yy}}$ was nearly identical with the value of von Mises strain which may be used as failure criterion. The calculated values include the ratios of ***i)*** the strain at the location of highest stress concentration which is found at the side faces of the samples (denoted as $K_{t\text{-dyn}}$) ***ii)*** the volume averaged strain in the gauge section of the samples (denoted as R_{FA}) to the calculated strain in the midsection of the side face of the holder (Fig. 36).

The strain distribution plots of the hourglass and double-edge notched miniaturized fatigue samples attached across the hole in the midsection of the holder are presented in Figs. 36a, c, e and 36b, d and f, respectively. The simulations show that the chosen experimental set-up results in a gradient of strain across the thickness of the samples (t=200 µm), with the highest values being in the midsection of their lower surface as shown for the hourglass (Fig. 36c) and notched samples (Fig. 36d). The strain distribution in the plane normal to the loading direction shows the proportional contribution of the stress values in the gauge section of the samples (Figs. 36e, f) from which the volume averaged strain was determined.

A summary of the experimental and theoretical strain ratios and stress concentration factors are given in Table 16. The results show that $K_{t\text{-Dyn}}$ for the notched samples at the location of the highest stress concentration is ~7.5 which is larger than the value of $R_E \times K_t$ (see also Eq. 6. 1) by a factor of two. On the other hand, the values of R_E x K_t show a better compliance with R_{FA}

(calculated volume averaged strain ratio) for all sample geometries. It is known that analytical or numerical methods based on the theory of elasticity may result to an overestimation of the stress concentration especially in the case of sharp notches due to neglecting the strain gradient effects. Therefore, in the present study the S-N curves were plotted by using the R_{Fave} factor for calculation of the volume averaged stress and the following formula:

$$\frac{\Delta\sigma}{2} = R_{FA}.E.\left(\frac{\Delta\varepsilon}{2}\right)_{holder} \tag{6.1}$$

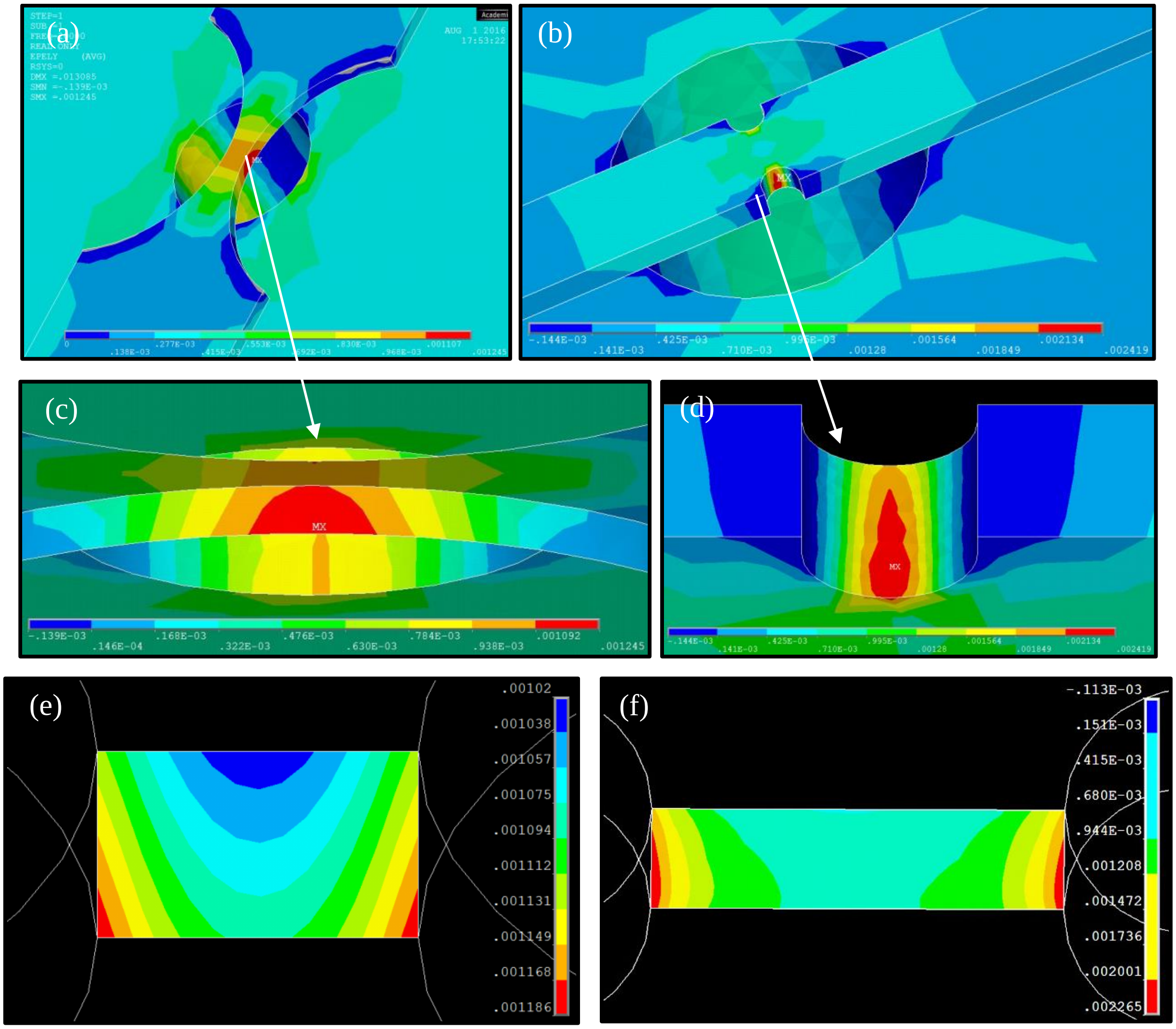

Fig. 36: Plots of strain distribution for (a, c) hourglass sample related to 845 µstrain on holder. Max. Strain: 0.33%. (K_t=3.90) (b, d) notched sample related to 321 µstrain on holder. Max. Strain: 0.33 %; (e and f) strain distribution in the gauge section of (e) hourglass and (f) notched samples in the plane normal to the loading direction.

Table 16. Summary of strain calibration measurements.

Sample shape and width	K_{tn}	R_E x K_{tn}	$K_{t\text{-}Dyn}$	R_{FA}
Hour-glass, 0.6 mm	**1.18**	**2.36**	**3.44**	**2.80**
Hour-glass, 0.35 mm	**1.05**	**2.10**	**3.91**	**3.42**
Double-edge notched, 0.35 mm	**1.83**	**3.66**	**7.53**	**3.32**

R_E : experimentally determined strain ratio ($\varepsilon_{sample} / \varepsilon_{holder} = 2$)

R_{FA} : volume averaged strain ratio calculated by FEM ($\varepsilon_{yy\ sample} / \varepsilon_{yy\ holder}$)

K_t : analytical net stress concentration factor

$K_{t\text{-}Dyn}$: stress concentration factor calculated by FEM (max. v.Mises strain)

6.3.2. Fatigue life curves

S-N curves of miniaturized notched and hourglass shaped CG Ti-45Nb samples are shown in Figs. 37a and b. The plot displayed in Fig. 37a shows the raw experimental fatigue data without taking the stress concentration factors of the samples (K_t) into account compared with those calculated on the basis of volume averaged stress (Eq. 6.1). The stress amplitude given in the fatigue life curves presented in Fig. 37b is based on the maximum stress concentration in the gauge section of the notched and hourglass-shaped samples. S-N curves of CG samples of both geometries show a rather flat trend in the region of HCF (N>1E+05-1E+09). As expected, the fatigue life curves based on volume averaged stress (VAS) lie above the raw experimental curves and the notched specimens demonstrate a fatigue strength of about 45% lower than their hourglass shaped counterparts (Fig. 37a) for stress values determined by both methods. On the other hand, using the $K_{t\text{-}Dyn}$ for estimation of the stress amplitude of the samples results in a higher lifetime for the notched samples than that of hourglass shaped ones with a considerable scattering of the fatigue data (Fig. 37b). Both trends are consistent with Weibull statistics considering the very small sample volume subjected to elevated stress in notched samples. In fact, the volume exposed to stress concentrations in miniaturized samples is so small that a variance of fatigue strength can be observed for the Ti-45Nb alloy.

In order to estimate the influence of stress concentration on the fatigue performance of the Ti-45Nb alloy it was attempted to determine the fatigue notch sensitivity factor of the CG material. The fatigue notch factor K_f is defined as

$$K_f = \sigma_{smooth}/\sigma_{notch} \tag{6.2}$$

with σ_{smooth} being the fatigue limit of unnotched bodies (hour glass shaped samples) and σ_{notch} being the fatigue limit of notched bodies. The fatigue notch sensitivity factor q, is obtained [82], [128] according to the below equation

$$q = \frac{K_f - 1}{K_t - 1}, \qquad \text{where} \qquad 0 \leq q \leq 1 \tag{6.3}$$

The full notch sensitivity is given by q=1 ($K_f = K_t$) and complete notch insensitivity is given by q = 0 ($K_f = 1$). The fatigue notch factor was determined based on the measured and calculated stress amplitudes at 1e9 loading cycles with the values of $K_{f,}$ = 1.74 (experimental stress amplitude ratio of 110/63) and $K_{f,}$ = 1.74 (calculated stress amplitude (VAS) ratio of 186/107) presented in Fig. 36a. Considering the value of K_t = 1.83 for the double edge notched samples after Peterson formula and the obtained experimental K_f value of ~ 1.7 of this study the notch sensitivity factor is determined to be q = 0.89. Consequently, the Ti-45Nb alloy with the given geometry and grain size of about 20 µm can be considered as notch sensitive [18].

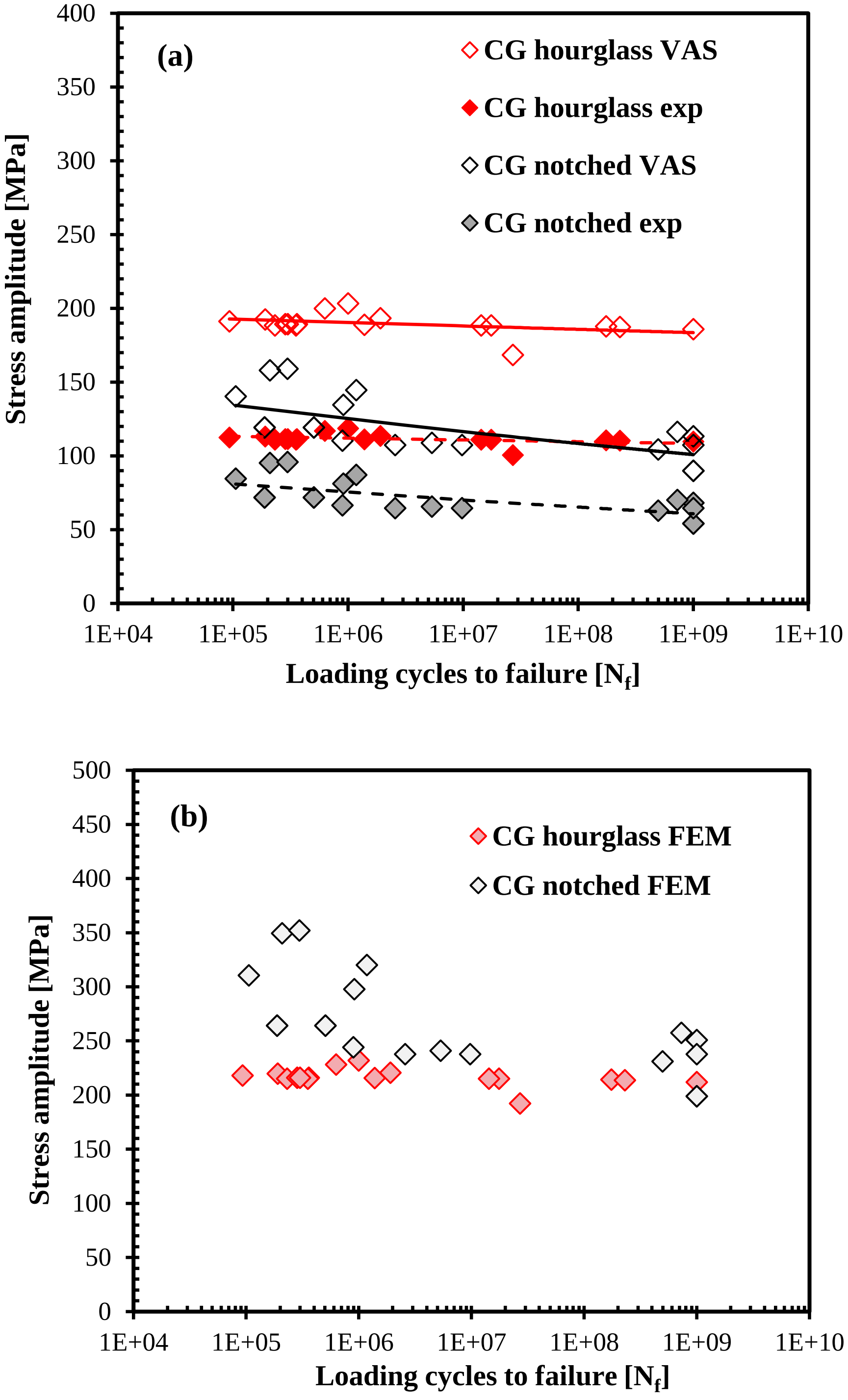

Fig. 37: Fatigue life curves of miniaturized notched and hourglass shaped CG Ti-45Nb samples (a) Experimental data without Kt, and volume average stress curves (b) Plotted based on the maximum stress (FEM).

Table 17. Fatigue data of Fatigue life curves of miniaturized notched and hourglass shaped CG Ti-45Nb samples a) experimental data without Kt, and volume average stress curves.

CG hourglass samples	Exp.stress amplitude without k_t (MPa)	Volume averaged stress (MPa)-FEM	Number of cycles to failure
sample1	119	203	1.00E+06
sample2	117	200	6.30E+05
sample3	114	193	1.90E+05
sample4	113	193	1.91E+06
sample5	112	191	9.30E+04
sample9	111	189	2.31E+05
sample13	111	189	2.84E+05
sample15	111	189	3.00E+05
sample11	111	189	3.53E+05
sample6	111	189	3.60E+05
sample8	111	189	1.38E+06
sample12	111	189	1.43E+07
sample14	111	189	1.75E+07
sample10	111	188	1.75E+08
sample17	110	187	2.30E+08
sample16	110	186	1.00E+09
sample20	101	169	2.7E+07
CG notched samples	**Exp.stress amplitude without k_t (MPa)**	**Volume averaged stress (MPa)-FEM**	**Number of cycles to failure**
sample6	96	159	2.98E+05
sample3	95	158	2.09E+05
sample2	87	145	1.18E+06
sample5	85	140	1.06E+05
sample4	81	135	9.11E+05
sample7	72	119	1.88E+05
sample13	72	119	1.88E+05
sample14	72	119	5.05E+05
sample15	72	119	5.05E+05
sample12	70	116	7.28E+08
sample10	68	113	1.00E+09
sample16	67	110	8.95E+05
sample19	66	109	5.34E+06
sample11	65	107	2.57E+06
sample17	65	107	9.75E+06
sample18	65	107	1.00E+09
sample8	63	104	4.96E+08
sample1	54	90	1.00E+09
sample9	54	90	1.00E+09

Table 18. Fatigue data of Fatigue life curves of miniaturized notched and hourglass shaped CG Ti-45Nb samples b) plotted based on the maximum stress (FEM).

CG hourglass samples	strain onsample	maximum stress amplitude (MPa)-(FEM)	Number of cycles to failure
sample1	1.83E-03	232	1.00E+06
sample2	1.80E-03	228	6.30E+05
sample3	1.75E-03	221	1.91E+06
sample4	1.74E-03	220	1.90E+05
sample5	1.73E-03	218	9.30E+04
sample10	1.71E-03	216	2.84E+05
sample14	1.72E-03	216	3.00E+05
sample16	1.72E-03	216	3.60E+05
sample12	1.71E-03	215	2.31E+05
sample6	1.71E-03	215	3.53E+05
sample9	1.71E-03	215	1.38E+06
sample13	1.71E-03	215	1.43E+07
sample15	1.71E-03	215	1.75E+07
sample11	1.72E-03	214	1.75E+08
sample20	1.70E-03	214	2.30E+08
sample17	1.69E-03	212	1.00E+09
sample21	1.55E-03	192	2.7E+07
CG notched samples	**strain on sample**	**maximum stress amplitude (MPa)-(FEM)**	**Number of cycles to failure**
sample6	9.90E-04	352	2.98E+05
sample3	9.84E-04	349	2.09E+05
sample2	9.08E-04	320	1.18E+06
sample5	8.83E-04	310	1.06E+05
sample4	8.50E-04	298	9.11E+05
sample7	7.63E-04	264	1.88E+05
sample13	7.63E-04	264	1.88E+05
sample14	7.63E-04	264	5.05E+05
sample15	7.63E-04	264	5.05E+05
sample12	7.46E-04	257	7.28E+08
sample10	7.29E-04	251	1.00E+09
sample16	7.12E-04	244	8.95E+05
sample19	7.03E-04	241	5.34E+06
sample11	6.95E-04	238	2.57E+06
sample17	6.95E-04	238	9.75E+06
sample18	6.95E-04	238	1.00E+09
sample8	6.77E-04	231	4.96E+08
sample1	5.94E-04	199	1.00E+09
sample9	5.94E-04	199	1.00E+09

The influence of grain refinement on the fatigue life of Ti-45Nb is presented in Fig. 38a with the stress amplitude being calculated based on the averaged v. Mises stress for the CG and UFG Ti-45Nb hourglass shaped samples. The endurance limit of UFG and CG material at 1E+09 cycles are 200 MPa and 186 MPa respectively resulting in a slight improvement of fatigue resistance due to HPT processing. Typical fatigue crack paths of the samples are displayed in the plane views of the failed CG (Fig. 38b) and UFG sample (Fig. 38c). The zigzag type and the straight crack path of the CG and the UFG samples respectively are in conformity with the commonly observed grain size dependent fatigue crack path morphologies in metallic materials (Figs. 38b, c, 39 and 40).

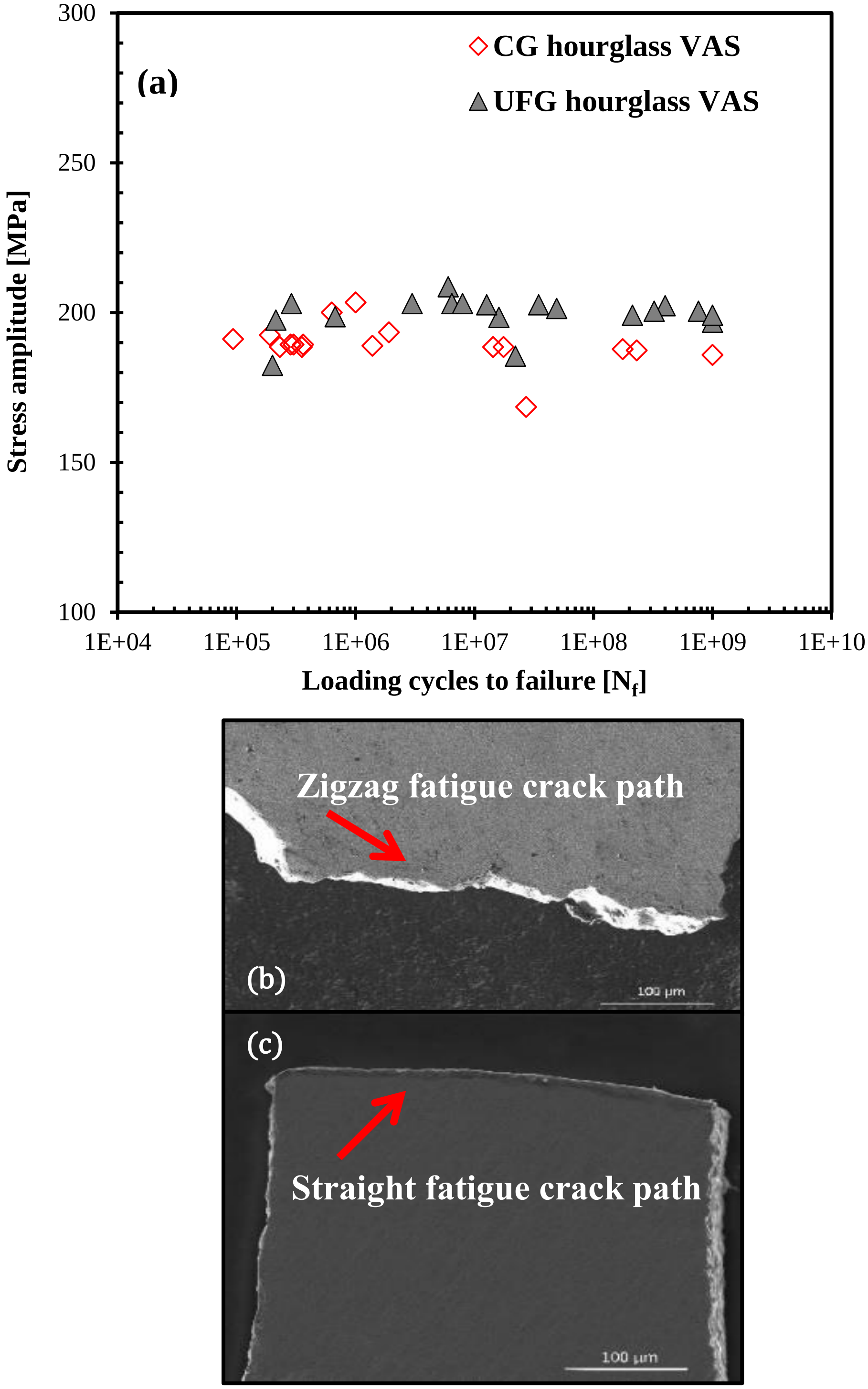

Fig. 38: (a) S-N curves of miniaturized hourglass initial (CG) and HPT samples (UFG) the notch factor of which (K_t) was calculated by FEM simulation (K_t =3.90). Plane view of failed (b) CG and (c) UFG Ti-45Nb fatigue samples.

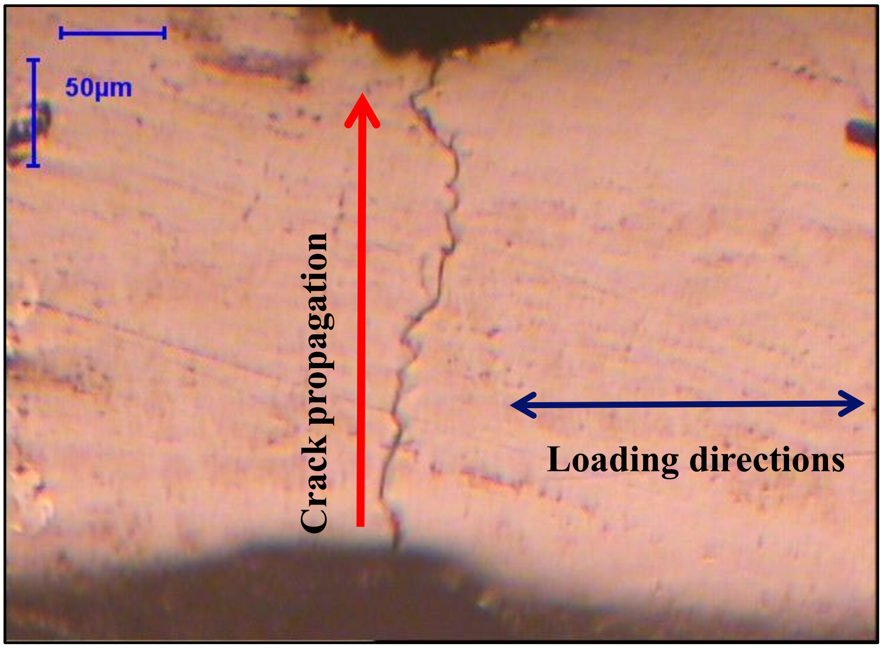

Fig. 39: Surface overview of the CG notched Ti-45Nb sample after fatigue test.

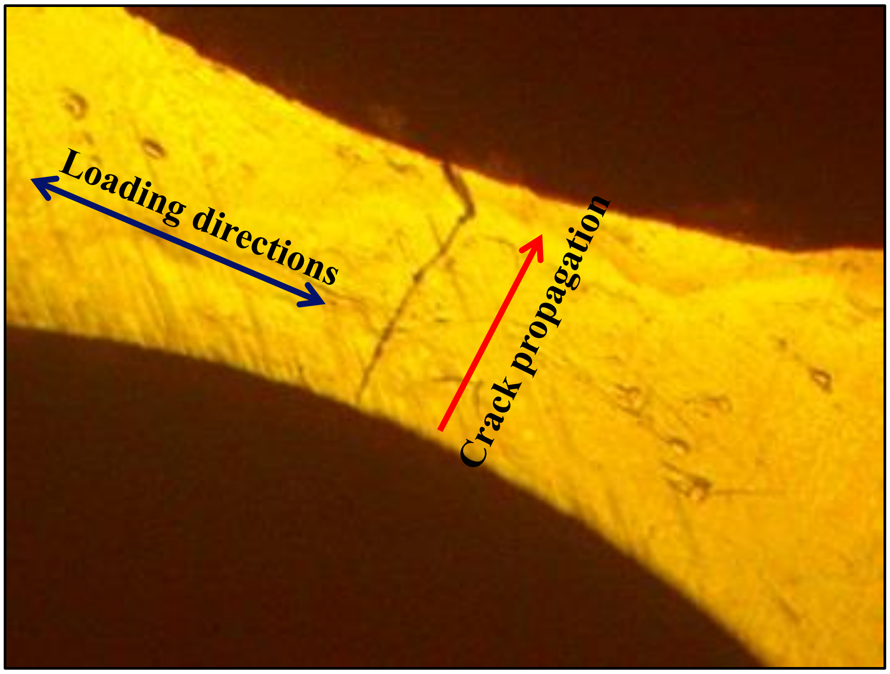

Fig. 40: Surface overview of the UFG hourglass shaped Ti-45Nb sample after fatigue test.

Table 19. Fatigue data of S-N curves of miniaturized hourglass initial (CG) and HPT samples (UFG) the notch factor of which (K_t) was calculated by FEM simulation (K_t =3.90).

CG hourglass samples	strain on sample	volume averaged stress (MPa)-FEM	Number of cycles to failure
sample1	1.83E-03	203	1.00E+06
sample2	1.80E-03	200	6.30E+05
sample3	1.75E-03	193	1.90E+05
sample4	1.74E-03	193	1.91E+06
sample5	1.73E-03	191	9.30E+04
sample6	1.71E-03	189	2.31E+05
sample8	1.71E-03	189	3.60E+05
sample9	1.71E-03	189	1.75E+07
sample10	1.72E-03	188	1.75E+08
sample11	1.70E-03	189	2.84E+05
sample12	1.71E-03	189	3.00E+05
sample13	1.71E-03	189	3.53E+05
sample14	1.72E-03	189	1.38E+06
sample15	1.71E-03	189	1.43E+07
sample16	1.72E-03	186	1.00E+09
sample17	1.69E-03	187	2.30E+08
sample20	1.70E-03	169	2.7E+07
UFG hourglass samples	**strain on sample**	**volume averaged stress (MPa)-FEM**	**Number of cycles to failure**
sample7	1.72E-03	209	6.00E+06
sample4	1.72E-03	203	2.89E+05
sample12	1.73E-03	203	2.99E+06
sample17	1.73E-03	203	6.45E+06
sample18	1.76E-03	203	7.89E+06
sample13	1.76E-03	203	1.26E+07
sample14	1.76E-03	203	3.45E+07
sample1	1.75E-03	202	4.00E+08
sample19	1.76E-03	201	4.88E+07
sample9	1.73E-03	201	3.22E+08
sample15	1.76E-03	201	7.60E+08
sample11	1.71E-03	199	6.70E+05
sample16	1.74E-03	199	2.12E+08
sample8	1.80E-03	199	1.00E+09
sample6	1.62E-03	198	1.60E+07
sample3	1.60E-03	197	2.13E+05
sample10	1.74E-03	197	1.00E+09
sample5	1.76E-03	185	2.20E+07
sample2	1.71E-03	182	2.00E+05

The effect of severe plastic deformation on the improvement of fatigue resistance of metals has been subject of a large number of investigations [129]–[131]. It has been reported that the expected fatigue response is dependent on several factors including the purity and composition of the used material, processing conditions, fatigue testing conditions and also the anticipated fatigue regime [131]–[133]. In most cases, it is reported that grain refinement by SPD processing of alloys and low purity metals results in a significant enhancement of fatigue resistance under stress controlled testing conditions in the high cycle regime [134]–[137]. In our study, as already presented, grain refinement by HPT processing resulted in a considerable increase in the yield strength and tensile stress of theTi-45Nb alloy (Table 14, Fig. 35). The fatigue limit at 1E+09 cycles is in the range of 185 to 200 MPa for the CG and UFG samples which correspond to $\frac{\sigma_s}{\sigma_f}$ (ratio of UTS to fatigue limit) of about 2.5 and 4.5 for the former and latter materials. Thus, considering that the maximum stress amplitude of the obtained S-N curve in the very high cycle regime (about 210MPa) is far below the elastic limit of the UFG material (σ_y = 860MPa), the high cycle fatigue response of the UFG Ti-45Nb of this study is rather unexpected.

Generally, the moderate fatigue performance of nanostructured or ultrafine grained materials processed by SPD has been related to the occurrence of cyclic softening due to the thermal and mechanical instability of the material. A further issue is the decreased ductility and the high crack growth rate in the materials with extremely fine microstructure [24], [50], [138], [139]. For a better understanding and interpretation of the fatigue response of CG and UFG Ti-45Nb alloy of the present study, fatigue fracture surfaces of the CG and UFG samples are analyzed and the evolution of microstructure, hardness and dislocation density of the UFG samples with increasing the loading cycles are investigated in the following.

6.3.3. Fracture surface analysis

Due to the flat trend of the obtained fatigue curves, the impact of the number of loading cycles to failure on the fracture behavior of the samples was studied. The fracture surfaces of CG samples which failed at almost the same stress amplitude and different loading cycles in the range of ~1E+05 to 1E+08 are presented in Figs. 41a, c, e. The corresponding details are shown in Figs 41b, d and f. It can be observed that independent from the loading cycles all samples failed in a crystallographic appearance with crack initiation site being at the surface or close to the surface. Surface or internal defects were scarcely identified as sources of fatigue cracks. Fatigue crack in the specimens which failed earlier initiated mostly from their corners with cracks originating from cleavage of one or a few grains at these sites and expanding radially across the surface (Figs. 41b, d). These plane faceted features were rarely observed on the samples which failed at higher loading cycles (Figs. 41e, f). The overall fracture morphology was a dominant quasi-cleavage type, which maintained its rough appearance throughout the sample. Apparently, a transition of crack propagation mode I to mode II did not occur, however several grains contained fatigue striations as marked in Figs. 41b, d, f. The fracture appearance could be related to the small size of the samples, suppressing the fatigue crack growth phase resulting in a short time to failure after initiation of the fatigue crack.

Fig. 42a shows the overview of the fracture surface of long life UFG Ti-45Nb fatigue sample with the detail being displayed in higher magnification in Fig. 42b. Fatigue crack originates from the corners and propagates through the gauge section of the sample resulting in a flat fracture surface morphology typical for UFG materials. Several fine lines expand across the cross section parallel to the surface of the sample in the shear plane of the HPT disc resulting in a step like appearance of fracture surface. The extremely fine parallel fatigue lines which run throughout the long life sample are shown at higher magnification in Fig. 42b. This image corresponds perfectly to the straight crack path observed on the plane surface of the UFG sample and indicates a rapid crack growth rate which might have resulted in a moderate fatigue resistance of UFG material. The low fatigue performance of the UFG samples can also be related to the fatigue notch sensitivity (q) of the material and the chosen sample geometry. The rectangular cross section of the samples with edges acting as stress raisers which may promote early crack initiation in both CG and UFG Ti-45Nb samples (as also shown in the FEM plots). Considering the high value of q = 0.89 obtained for the CG alloy of this study, and the commonly accepted trend of increased notched sensitivity with decreasing grain size, a higher impact of the sample geometry on the fatigue response of the UFG Ti-45Nb may be expected [140], [141].

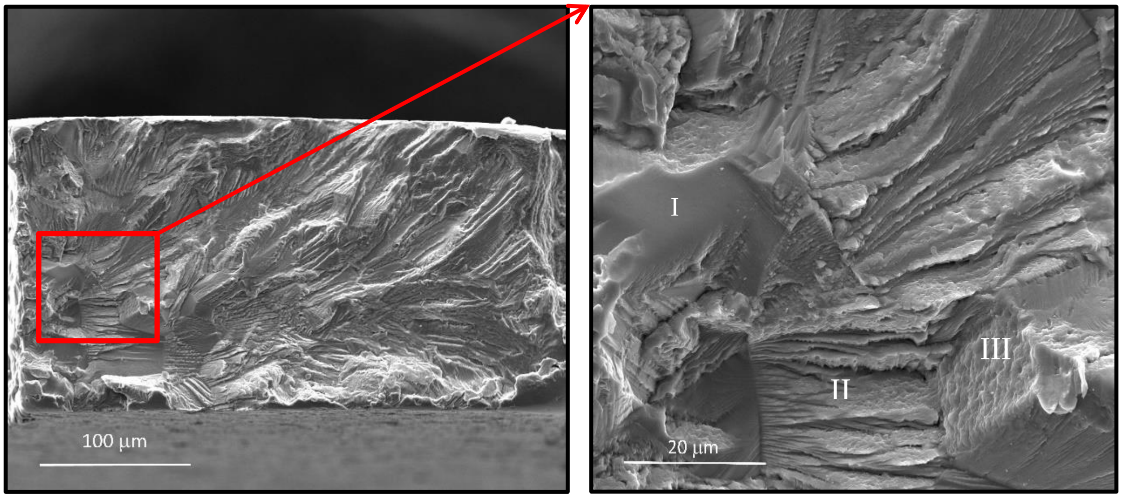

a) Stress amplitude 189 MPa, N_f 3e5

b) detail of (a) showing plane faceted grains (I), river lines (II) and striations (III)

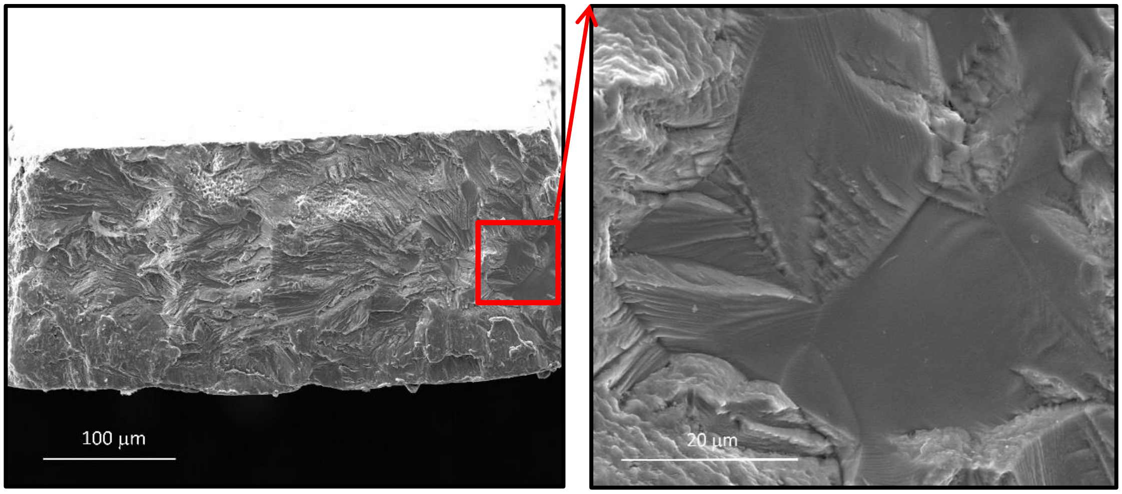

c) Stress amplitude 189 MPa, N_f 1.38e6

d) details of (c)

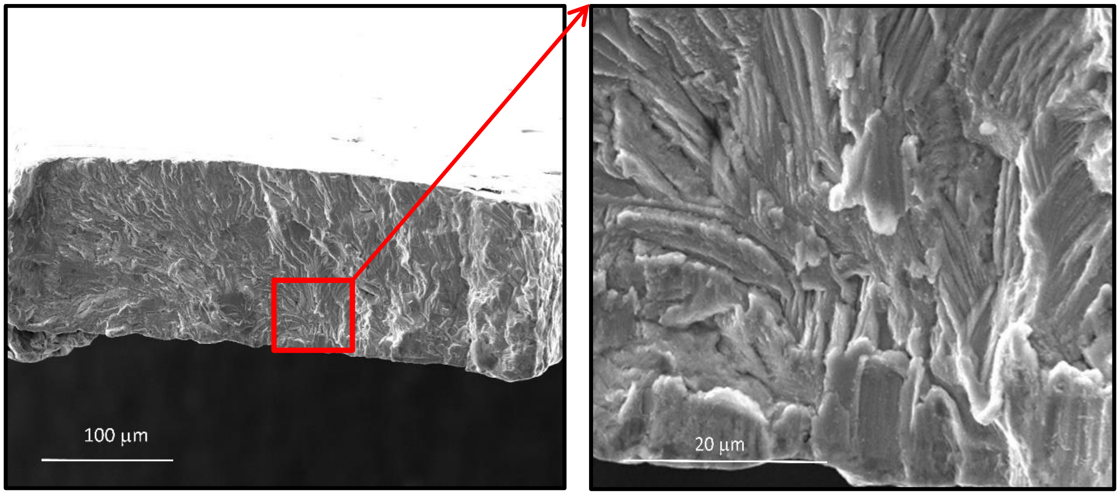

e) Stress amplitude 187 MPa, N_f 2.3e8

f) details of (e)

Fig. 41: Fatigue fracture surfaces of coarse grained Ti-45Nb samples failed at about 234 MPa and different loading cycles, (a, c, e) overview and (b, d, f) detail SEM images.

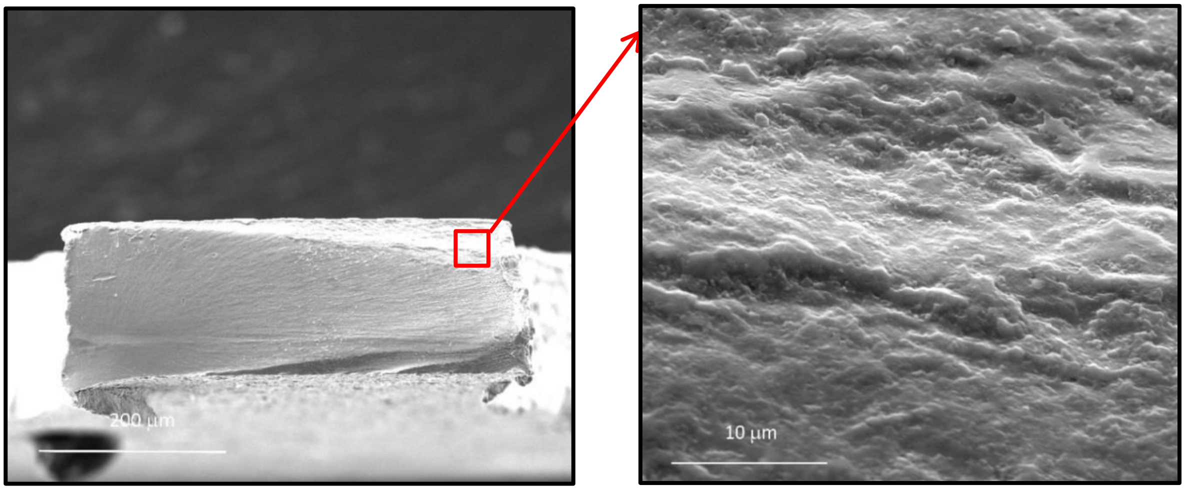

a) Stress amplitude 199 MPa, N_f 6.7e5
(early failure)

b) Extrusions on the fatigued surface, details of (a)

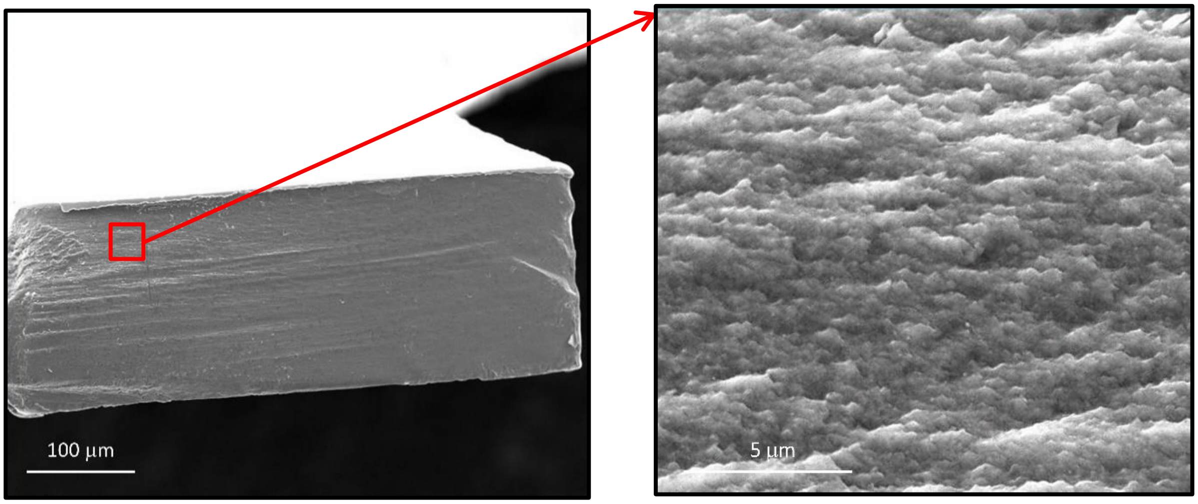

c) Overview of an UFG sample, stress amplitude 199 MPa, N_f 2.12e8 (long life)

d) Details of the fracture surface shown in (a)

Fig. 42: Overviews and details of fatigue fracture surfaces of ultra-fine grained Ti-45Nb samples failed at about 200 MPa at (a) lower and (c) higher loading cycles with details (b, d).

6.3.4. Analysis of the fatigue response of UFG Ti-45Nb

The microstructural stability of the HPT Ti-45Nb material during the dynamic loading was examined by means of TEM and X-ray diffraction analysis. TEM images of a run out UFG Ti-45Nb sample (Stress amplitude = 200 MPa and N=1E+09) are presented in Figs. 43a and b. Careful microstructural examinations did not show evidence of noticeable changes in the grain size of material after long-term fatigue loading. Fig. 44 confirms that the measured intensity profiles of the UFG Ti-45Nb samples prior to and subsequent to fatigue loading remain unchanged. Measurement of the crystallite size of the HPT processed samples in dependency with loading cycles to failure as performed by using Convolutional Multiple Whole Profile (CMWP) [113], [114] indicated a sub-grain size of about 20 nm for all specimens (Fig. 45). These data also confirm absence of grain coarsening as a result of dynamic recrystallization of the UFG Ti-45Nb during the high cycle fatigue.

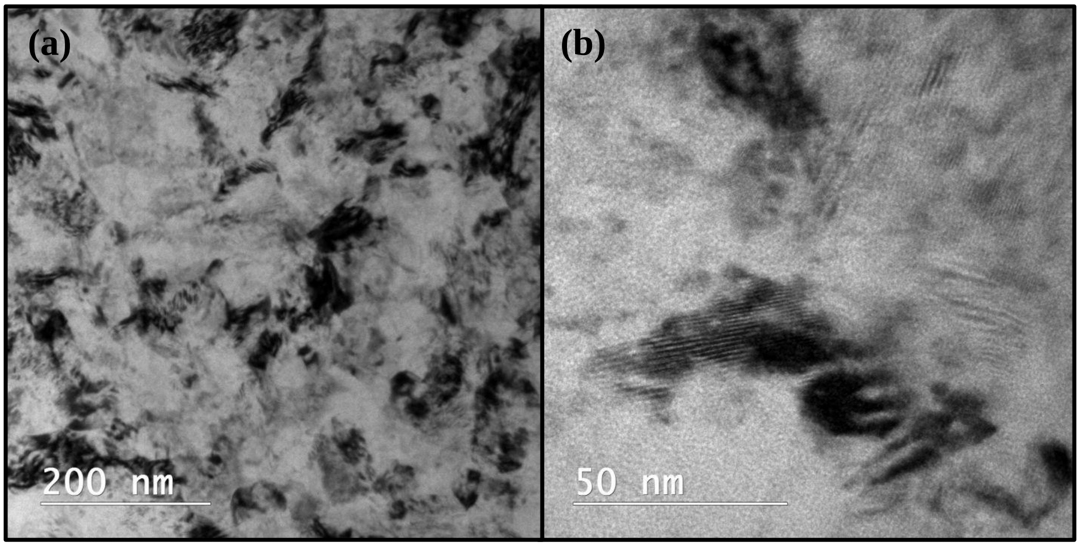

Fig. 43: Low (a) and high (b) magnification bright field TEM images of the microstructure of a run out UFG Ti-45Nb material (200MPa, N=1e9 loading cycles).

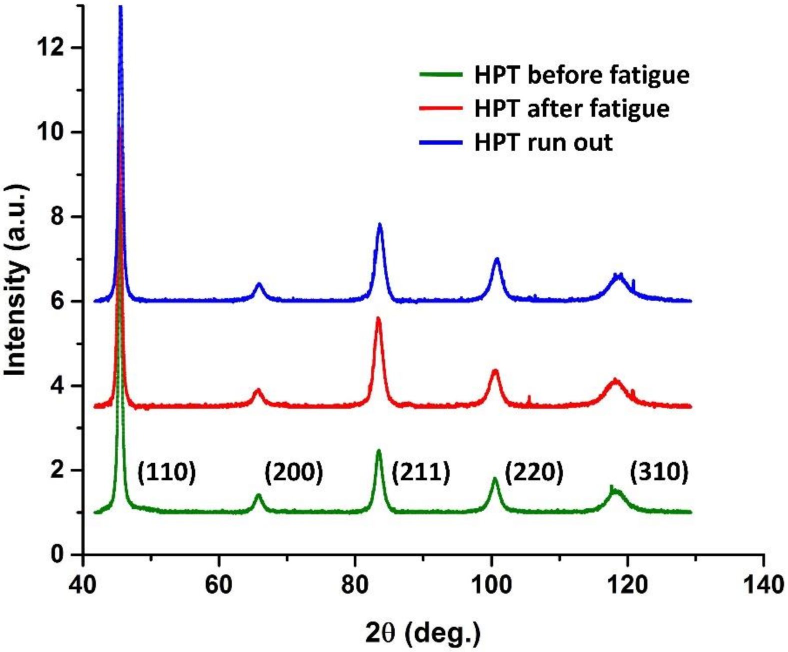

Fig. 44: Measured intensity profiles of HPT Ti-45Nb samples in three different states.

The influence of cyclic loading on the evolution of nanohardness and dislocation density (ρ) of the UFG samples is displayed in Fig. 46 in which a gradual decrease of the both values with increasing the loading cycles is observed. The relatively high dislocation density of the Ti-45Nb sample after HPT processing ($\rho = 3.1\times10^{15}$ m^{-2}) decreases about 10% after 3.45e7 loading cycles at 203 MPa and falls to about 60% of the original value (1.9×10^{15} m^{-2}) after loading at 200MPa and 1e9 loading cycles. The nanohardness values obtained for the same samples showed a slight reduction of about 4% in the intermediate regime and 12% at very high loading cycles.

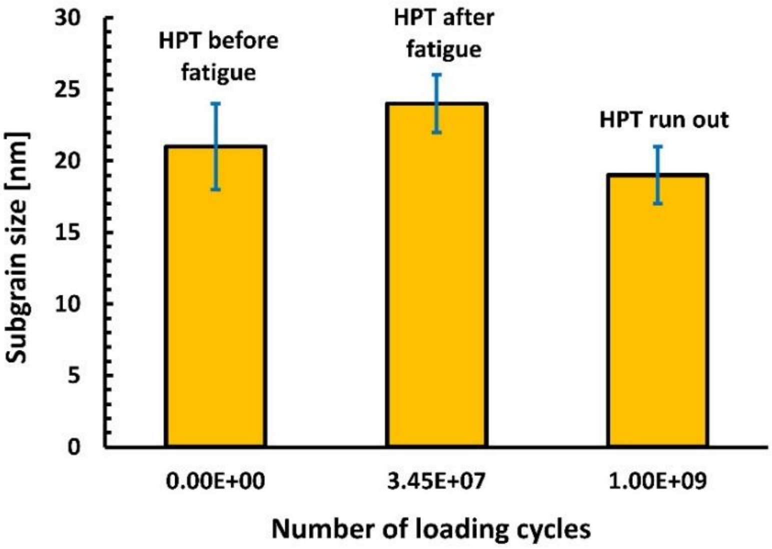

Fig. 45: Subgrain size as a function of loading cycles.

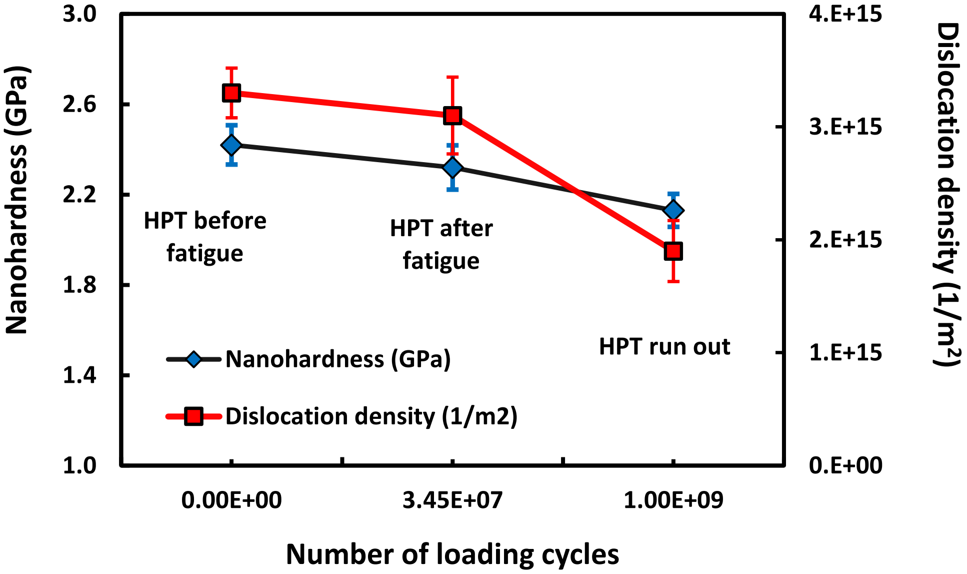

Fig. 46: Nanohardness and dislocation density of UFG material as a function of loading cycles.

Table 20 summarizes results of the measured nanohardness, dislocation density and subgrain size as a function of loading cycles for the UFG samples before and after fatigue tests.

Table 20. Analysis results of the HPT samples before and after fatigue tests.

sample	Loading cycles	Nanohardness (GPa)	Dislocation density (m^{-2})	Subgrain size (nm)
HPT before fatigue	0	2.42	3.30E+15	21
HPT after fatigue	3.45E+07	2.32	3.10E+15	24
HPT run-out	1E+09	2.13	1.90E+15	19

Previous studies have shown that the decrease in hardness of UFG Cu after fatigue does not necessarily scale with the cell size according to a well-known relationship between the saturation stress and cell size [142]. It has been suggested that cyclic softening in UFG metals is not directly related to the grain coarsening and the mechanism of softening is related to the decrease of defect density and changes of boundary misorientation rather than to the grain size [143]. This might also be considered as a possible explanation of the moderate fatigue response of the UFG Ti-45Nb material of this study requiring future investigations.

6.4. Bulk Ti-45Nb specimens

6.4.1. Finite element analysis

Fig. 47 shows an FEM model of the resonance sample with details in the notch region. The plots of von Mises stress in the gauge section of the samples with U and V shaped notches are presented in Figs. 48a and c and the corresponding magnified images are shown in Figs. 48b and d, respectively. These plots clearly show that introducing a circumferential V-notch in the sample with the given geometry causes a significantly higher stress concentration in the root of the notch (242 MPa for U notch, 420 MPa for V-notch in Figs. 48b and d). Therefrom, the dynamical values for K_t at the notch root were evaluated ($K_{t\text{-dyn}}$ in Table 22).

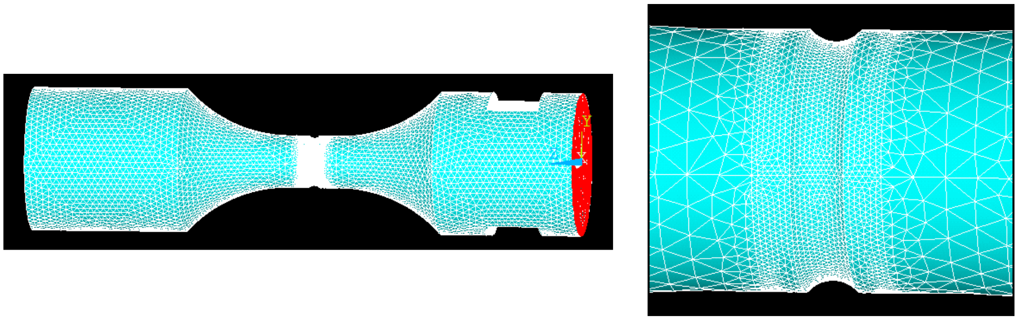

Fig. 47: FEM model of the resonance sample with details in the notch region.

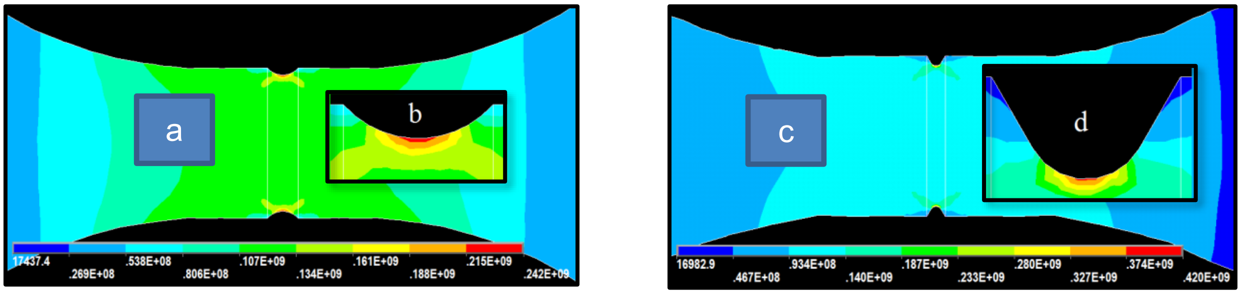

Fig. 48: Plot of the von Mises stress [Pa] for samples with U- and V-notches (a, c), corresponding magnified plot of the von Mises stress showing the stress concentration at the notch (b, d). (The displacement amplitude at the ends of both samples was 13.4 µm, respectively).

6.4.2. Fatigue life curves

Fatigue life curves of the plain and notched Ti45Nb up to 1E+09 loading cycles are shown in Fig. 49. The fatigue resistance of the smooth samples at 1E+09 cycles is 260 MPa, while without considering the stress concentration factors, the stress amplitude for U-notched and V-notched samples is about 147 and 110 MPa, respectively. The fatigue notch factors K_f for the samples with U- and V-notches was determined by using (Eq. 6.4a). The notch sensitivity (Eq. 6.4 b) was considered using Peterson's approach (Eq. 6.4 c).

$$K_f = \frac{\sigma_{smooth}}{\sigma_{notch}} \quad (6.4\ a) \qquad q = \frac{K_f - 1}{K_t - 1} \quad (6.4\ b) \qquad K_f = 1 + \frac{K_t - 1}{1 + \frac{\alpha}{r}} \quad (6.4\ c)$$

where r is the notch radius and α is a material parameter. The material parameter α was calculated by inserting the experimental values for K_f and the FEM results of the harmonic simulation for K_t in equation (6.4 b). The results of this evaluation are also summarized in Table 22 and Fig. 50.

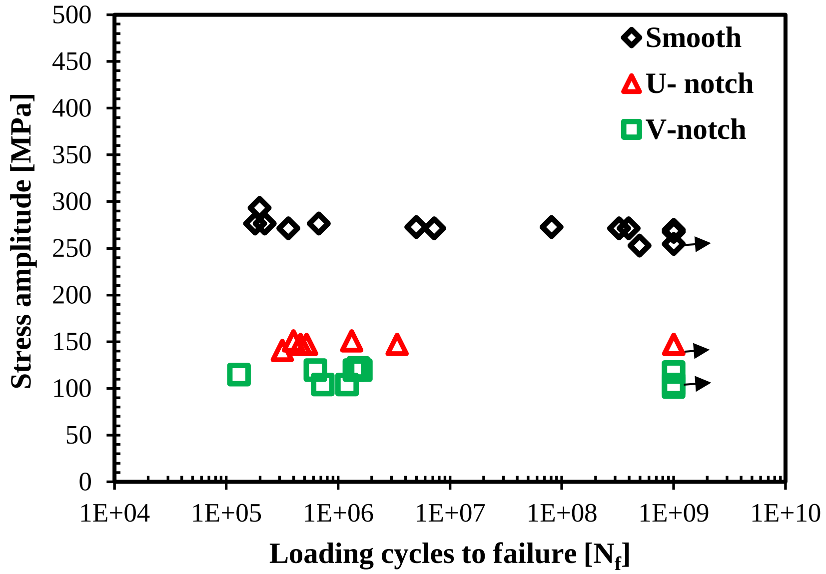

Fig. 49: Fatigue life curves of bulk Ti45-Nb samples (arrows indicate the run-out samples).

Table 21. Fatigue data of smooth, U-notched and V-notched bulk Ti-45Nb samples.

Smooth Ti-45Nb samples	**Strain at midsection of sample**	**Stress amplitude (MPa)**	**Number of cycles to failure**
Sample 4	**4.50E-03**	**320**	**1.99E+05**
Sample 5	**4.24E-03**	**301**	**1.81E+05**
Sample 7	**4.24E-03**	**301**	**2.21E+05**
Sample 8	**4.24E-03**	**301**	**6.72E+05**
Sample 14	**4.19E-03**	**297**	**5.00E+06**
Sample 15	**4.19E-03**	**297**	**8.11E+07**
Sample 9	**4.17E-03**	**296**	**3.58E+05**
Sample 11	**4.17E-03**	**296**	**7.22E+06**
Sample 12	**4.17E-03**	**296**	**3.26E+08**
Sample 13	**4.17E-03**	**296**	**3.95E+08**
Sample 10	**4.14E-03**	**294**	**1.00E+09**
Sample 3	**4.11E-03**	**292**	**1.00E+09**
Sample 6	**3.91E-03**	**278**	**1.00E+09**
Sample 2	**3.88E-03**	**276**	**4.95E+08**
Sample 1	**3.53E-03**	**250**	**1.00E+09**
U-notch Ti-45Nb samples			
Sample 6	**2.32E-03**	**165**	**4.00E+05**
Sample 7	**2.32E-03**	**165**	**1.32E+06**
Sample 1	**2.26E-03**	**160**	**4.61E+05**
Sample 2	**2.26E-03**	**160**	**5.23E+05**
Sample 3	**2.26E-03**	**160**	**3.37E+06**
Sample 4	**2.26E-03**	**160**	**1.00E+09**
Sample 5	**2.26E-03**	**160**	**1.00E+09**
Sample 8	**2.16E-03**	**153**	**3.17E+05**
V-notch Ti-45Nb samples			
Sample 10	**1.87E-03**	**133**	**1.52E+06**
Sample 1	**1.83E-03**	**130**	**6.29E+05**
Sample 7	**1.83E-03**	**130**	**1.40E+06**
Sample 9	**1.83E-03**	**130**	**1.60E+06**
Sample 3	**1.80E-03**	**128**	**1.00E+09**
Sample 4	**1.76E-03**	**125**	**1.30E+05**
Sample 5	**1.60E-03**	**113**	**7.30E+05**
Sample 6	**1.60E-03**	**113**	**1.21E+06**
Sample 8	**1.60E-03**	**113**	**1.00E+09**
Sample 2	**1.55E-03**	**110**	**1.00E+09**

Table 22. Comparison of calculated and experimental stress concentration factors, notch sensitivity and parameter α.

Notch shape	K_t	$K_{t\text{-}dyn}$	K_f	*q*	α[mm]
U	**1.83**	**1.93**	**1.79**	**0.95**	**0.0975**
V	**2.69**	**3.37**	**2.28**	**0.76**	**0.126**

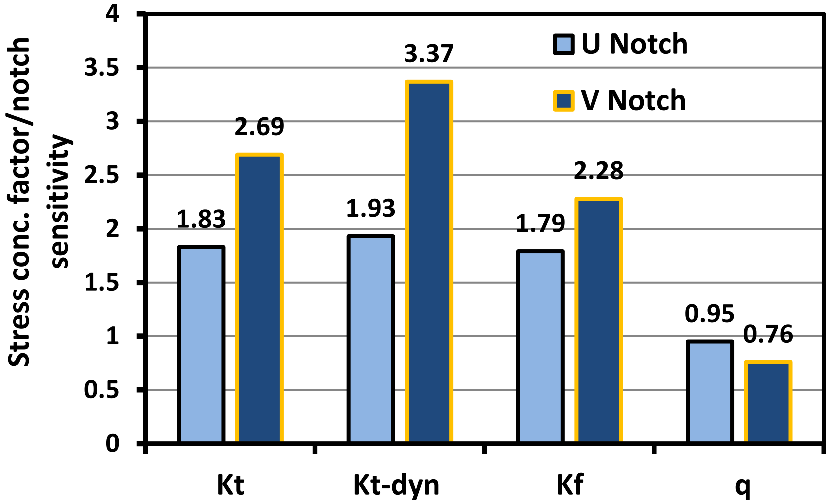

Fig. 50: The plot of comparison of calculated and experimental stress concentration and notch sensitivity factors.

The notch sensitivity observed in the fatigue experiments resulting in $K_f < K_t$ has been previously discussed [31], [144], [145]. One possible explanation for this behaviour could be that a sharp V-notch increases the stress only in a small volume while a U-notch with larger radius of curvature increases the stress in a larger portion of the volume. Such fatigue behaviour is known from Weibull statistics. Another possible explanation may be derived from strain gradient elasticity. The stress gradients observed near the notches certainly lead to strain gradients and therefore to a bending of the crystal lattice. However, the microstructure of the material reacts with stiffness against bending and therefore stress concentrations are reduced [146]. In consequence, the parameter α of equation (6.4 c) representing a critical length could be related to strain gradient elasticity.

6.4.3. Fracture surface analysis

Examination of the fracture surfaces of the fatigued samples showed a strong dependency of the lifetime on the location of the microstructural inhomogeneity or defects (Fig. 51). Independent from the stress amplitude, failures up to a maximum of 1E+07 were caused due to crack initiation from one or several locations at the periphery of the samples. Those which survived up to higher loading cycles finally failed due to internal crack initiation.

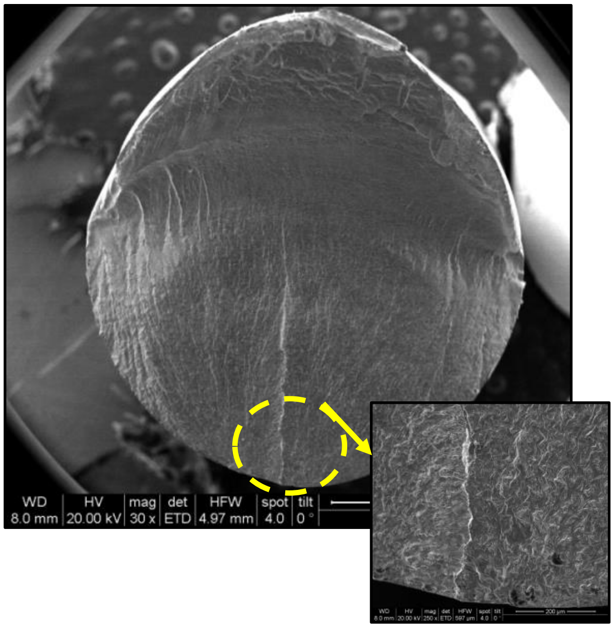

a) $\Delta\sigma/2$ = 276 MPa N_f =4.24E+03

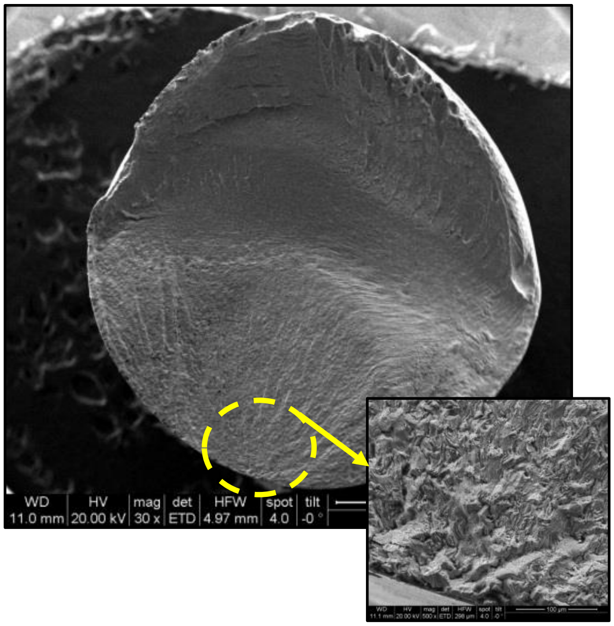

b) $\Delta\sigma/2$ = 276 Mpa N_f =1.81E+05

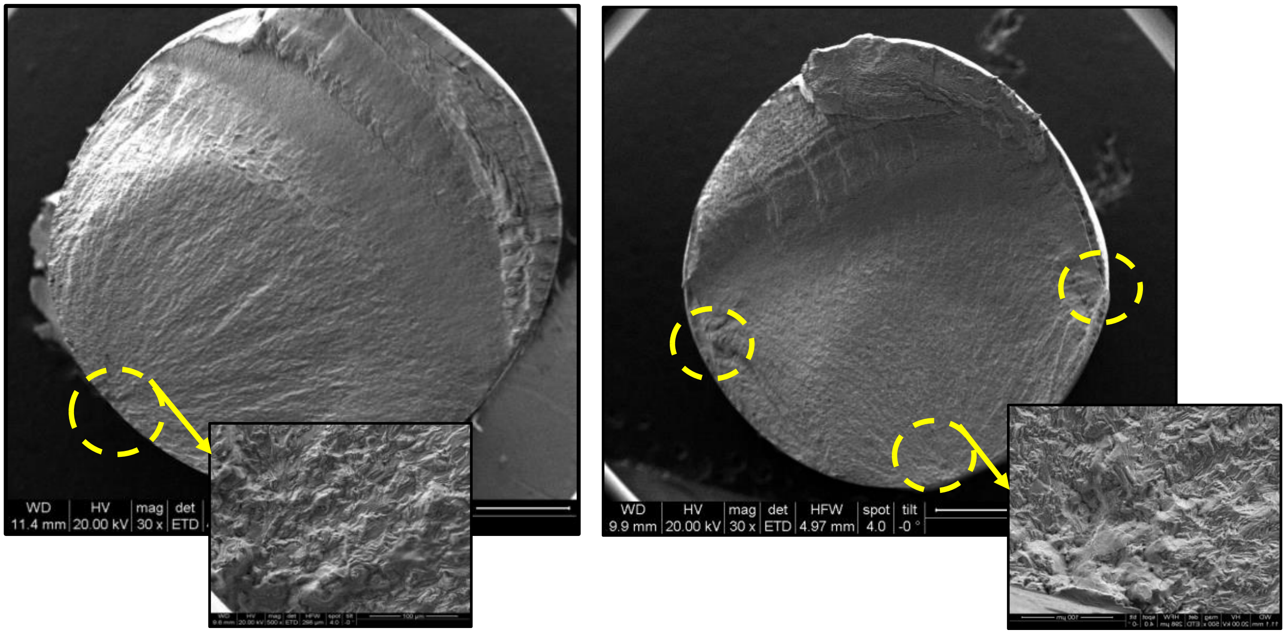

c)$\Delta\sigma/2 = 273$ MPa $N_f = 5.00E+06$

d) $\Delta\sigma/2 = 273$ MPa $N_f = 8.11E+07$

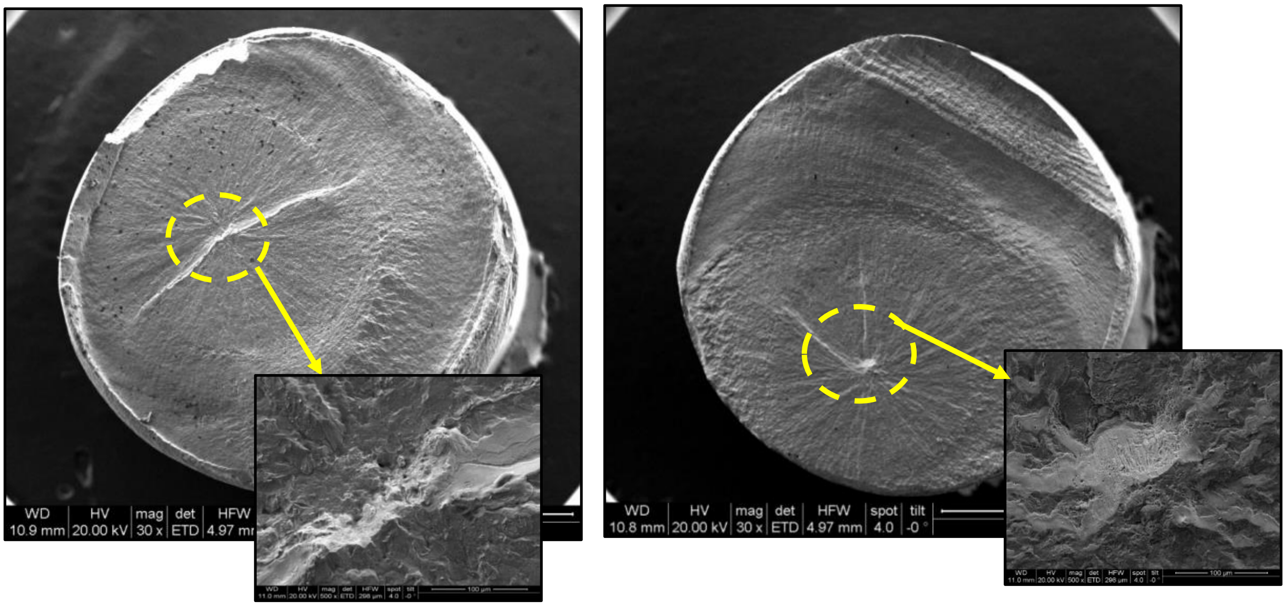

e)$\Delta\sigma/2 = 271$ MPa $N_f = 3.95E+08$

f) $\Delta\sigma/2 = 271$ MPa $N_f = 3.26E+08$

Fig. 51: Typical fatigue fracture surfaces (overview and detail SEM images) of smooth Ti45Nb samples after fatigue failure, (a, b, c) single and d) multiple surface crack initiation sites,(e, f) internal crack initiation site.

Previous studies have shown a relationship between the origin of the fatigue crack and loading cycles to failure. It is suggested that **i)** failure at higher loads and low cycle to failure is mainly caused by several crack initiation sites at the surface, **ii)** failure at intermediate fatigue life regime originates from surface cracks and **iii)** the materials fail due to internal defects after very high loading cycles [147]. In our study, the type of failure was rather independent from the stress level, but mainly dependent on the number of loading cycles. It was observed that at almost the same stress level failure might occur either due to internal or surface defects as demonstrated in Fig. 51. The relation between the failure mode and cycles to failure can be also seen in Fig. 52.

This behavior, which can be mainly related to the distribution of inhomogeneities, defects and flaws in the tested Ti45Nb material, may explain the rather straight shape of the lifetime curve and the scatter of fatigue data. Figs. 53-57 show other examples of internal and multiple fatigue surface crack initiation sites of bulk Ti-45Nb samples failed at different stress amplitudes.

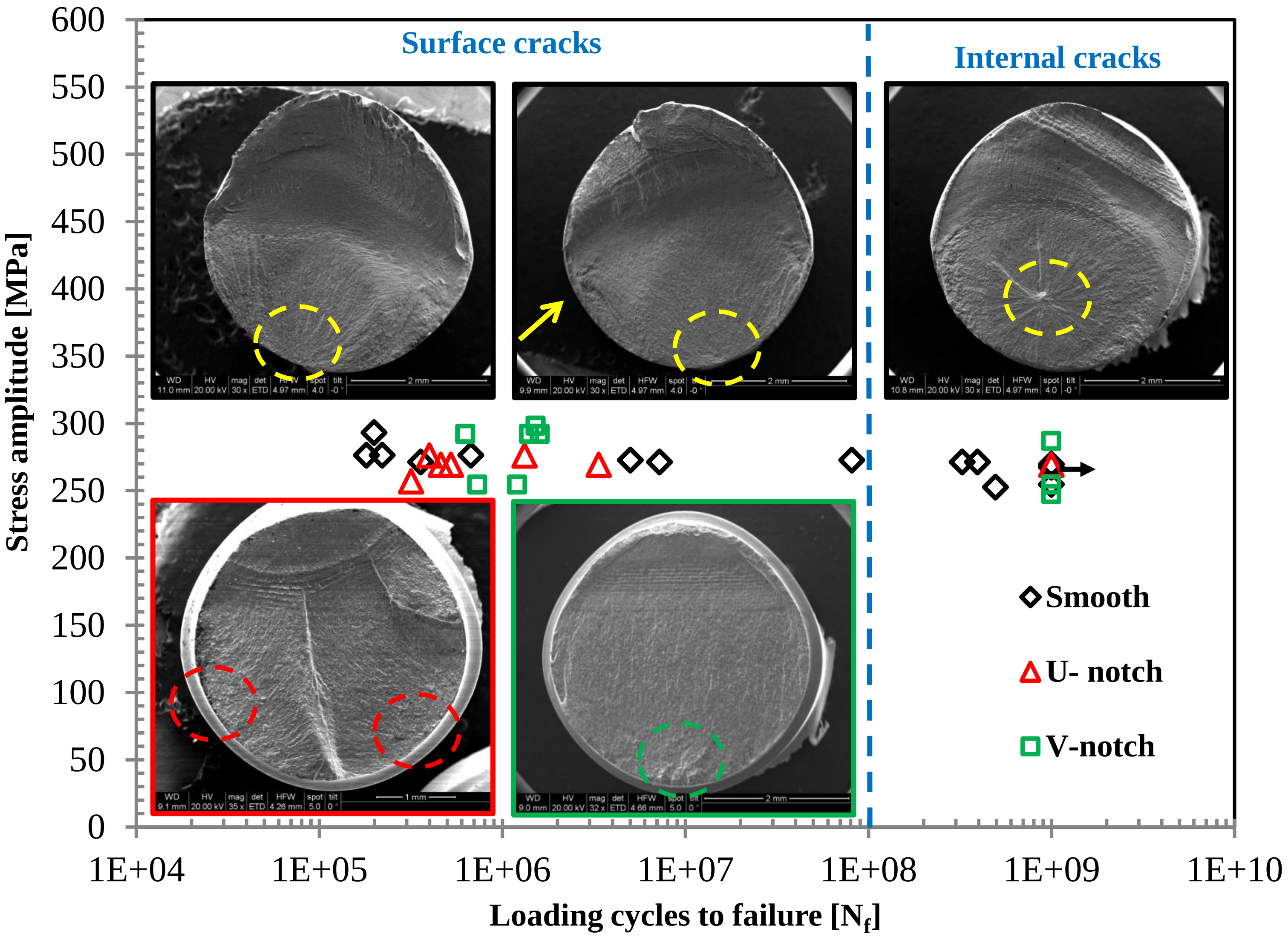

Fig. 52: Relation between the failure mode and cycles to failure.

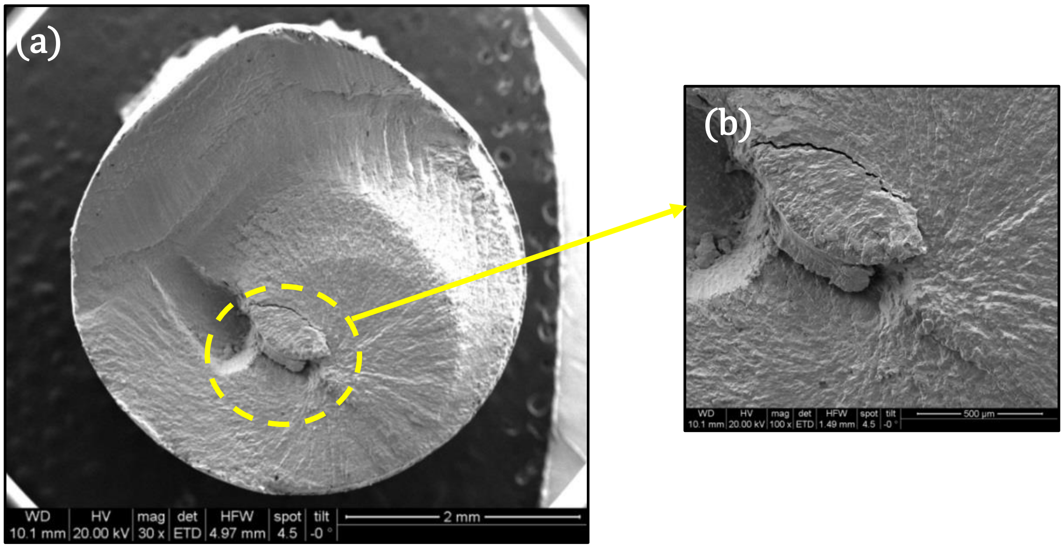

Fig. 53: Fatigue fracture surface of bulk Ti-45Nb sample failed at $\frac{\Delta\sigma}{2}$ = 293 MPa, N_f =1.99E+05 (a) overview and (b) detail of (a) internal crack initiation site.

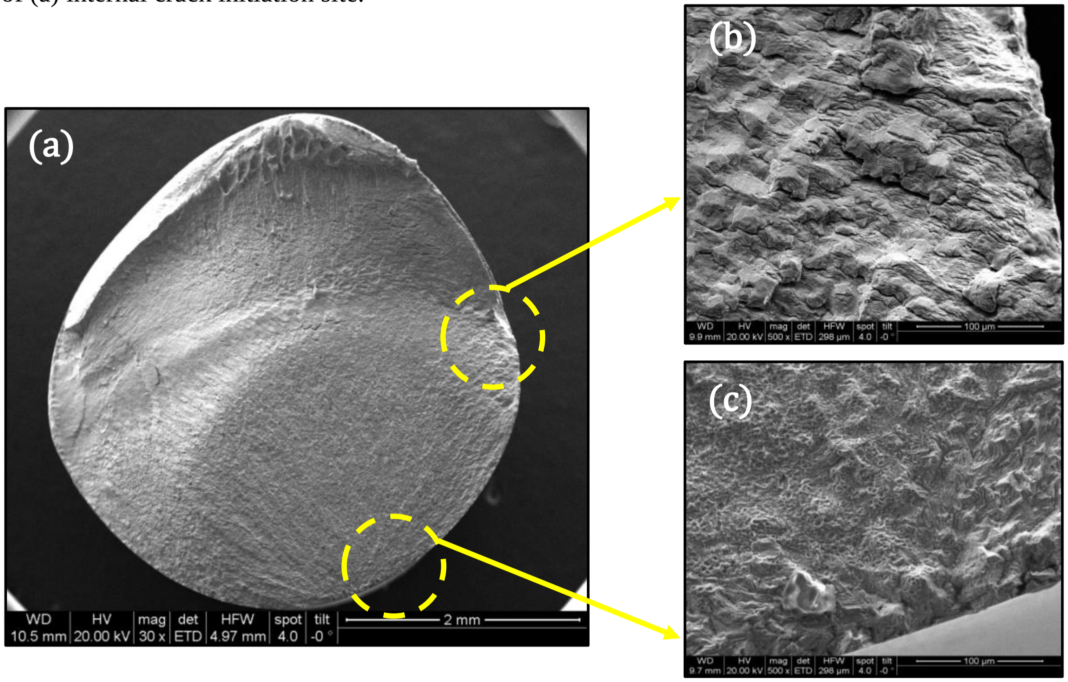

Fig. 54: Fatigue fracture surface of bulk Ti-45Nb sample failed at $\frac{\Delta\sigma}{2}$ = 293 MPa, N_f =1.99E+05, (a) overview and (b, c) details of (a) multiple surface crack initiation sites.

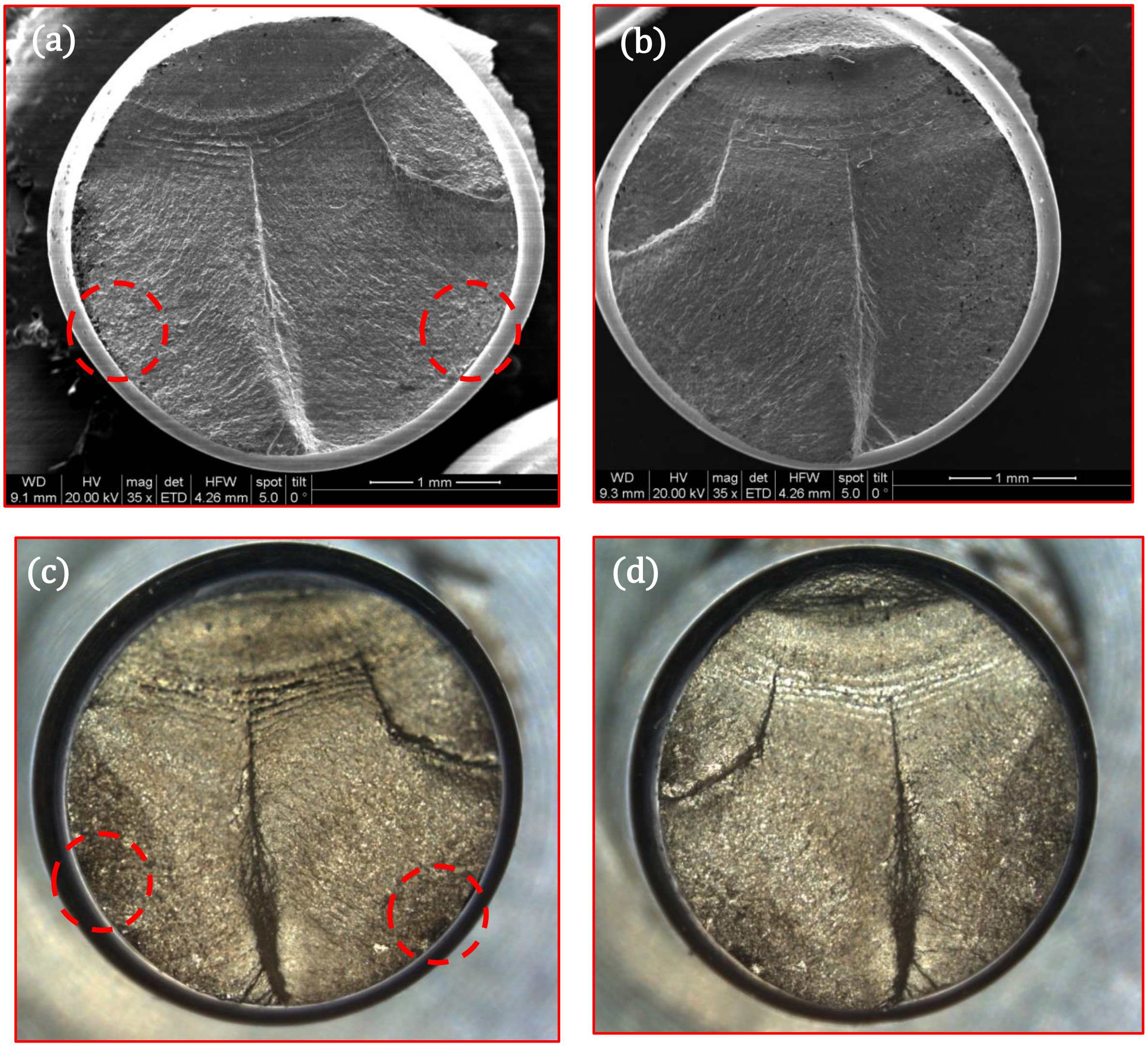

Fig. 55: overviews of multiple surface crack initiation sites of U-notched Ti45Nb sample failed very soon at $\frac{\Delta\sigma}{2}$ = 342 MPa, (a, b) SEM images, (c, d) OM images.

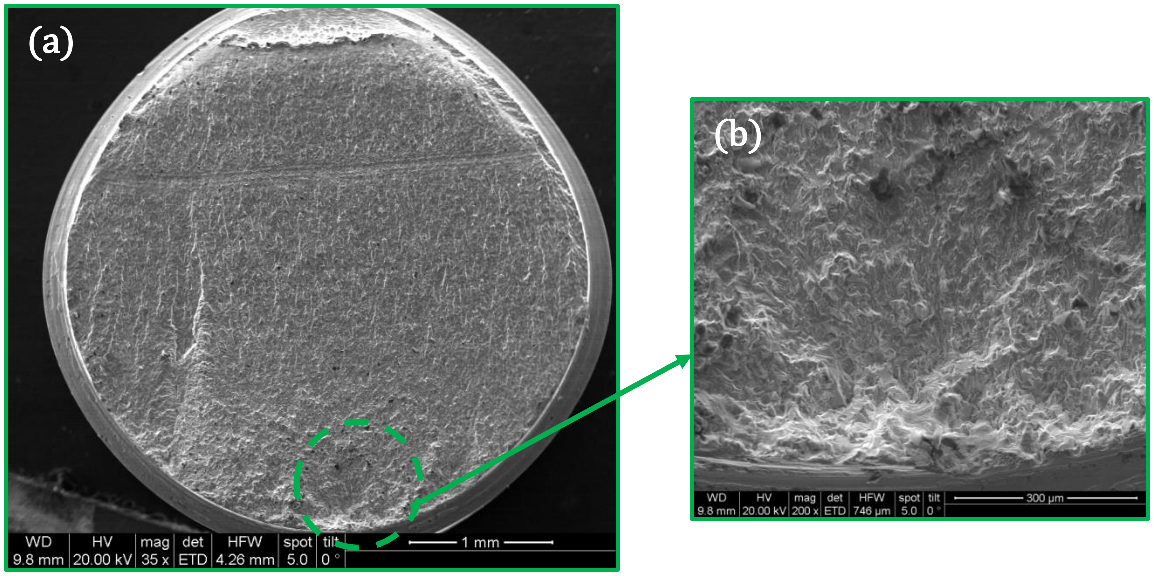

Fig. 56: Fatigue fracture surface of V-notched Ti45Nb sample failed very soon at at $\frac{\Delta\sigma}{2}$ = 305 MPa, N_f =7.30E+05, (a) overview and (b) details of (a).

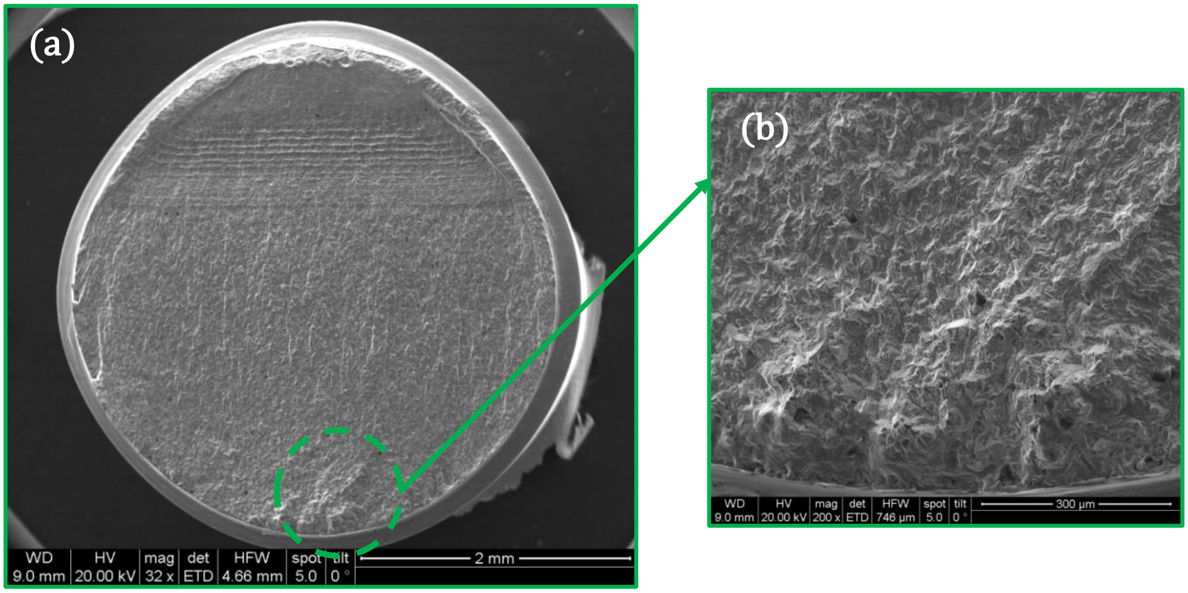

Fig. 57: Fatigue fracture surface of V-notched Ti45Nb sample failed very soon at at $\frac{\Delta\sigma}{2}$ = 350 MPa, N_f =1.60E+06, (a) overview and (b) details of (a).

6.4.4. A comparison of high cycle fatigue life of bulk samples with lifetime of miniaturized samples of Ti-45Nb

S-N curves of miniaturized and bulk smooth (hourglass shaped) CG Ti-45Nb samples are shown in Fig. 58. The stress amplitude related to the miniaturized hourglass shaped samples given in the fatigue life curve is based on the maximum stress concentration in the gauge section of the miniaturized hourglass-shaped samples. The fatigue resistance of miniaturized and smooth bulk samples at 1e9 cycles was determined to be 216 MPa and 260 MPa, respectively. In case of smooth bulk samples, the cycles to failure was highly dependent on the location of the defects.

The lower fatigue resistance of the smooth miniaturized samples of the present study with a rectangular cross section (216 MPa) in comparison with the bulk Ti-45Nb samples with circular cross section [34] can be mainly explained by the influence of sample geometry. According to the cross-sectional stress distribution plots of Figs. 36e and f the stress at the edges of the rectangular shaped samples is considerably raised. Thus, for the notch sensitive material, the presence of these stress concentrators can lead to an earlier failure as also confirmed by the fracture surface analysis of the fatigued miniaturized samples.

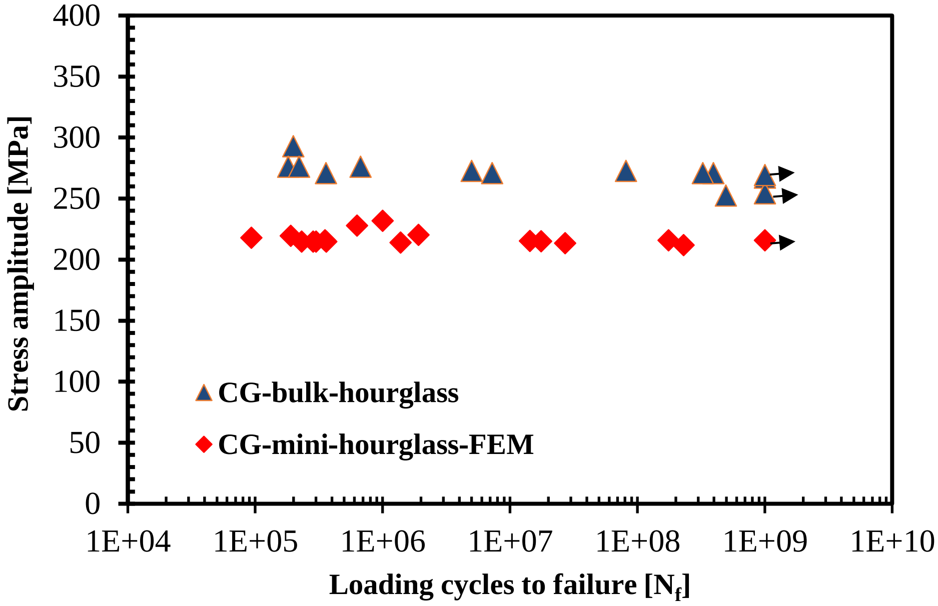

Fig. 58: S-N curves of miniaturized and bulk hourglass shaped Ti-45Nb samples.

Table 23. Fatigue data of fatigue life curves of miniaturized and bulk hourglass shaped Ti-45Nb samples.

CG-mini- hourglass samples	strain on sample	maximum stress amplitude (MPa)-(FEM)	Number of cycles to failure
sample1	1.83E-03	232	1.00E+06
sample2	1.80E-03	228	6.30E+05
sample3	1.75E-03	221	1.91E+06
sample4	1.74E-03	220	1.90E+05
sample5	1.73E-03	218	9.30E+04
sample10	1.71E-03	216	2.84E+05
sample14	1.72E-03	216	3.00E+05
sample16	1.72E-03	216	3.60E+05
sample12	1.71E-03	215	2.31E+05
sample6	1.71E-03	215	3.53E+05
sample9	1.71E-03	215	1.38E+06
sample13	1.71E-03	215	1.43E+07
sample15	1.71E-03	215	1.75E+07
sample11	1.72E-03	214	1.75E+08
sample20	1.70E-03	214	2.30E+08
sample17	1.69E-03	212	1.00E+09
sample21	1.55E-03	192	2.7E+07
CG-bulk- hourglass samples	strain on sample	stress amplitude (MPa)	Number of cycles to failure
sample4	4.50E-03	293	1.99E+05
sample5	4.24E-03	276	1.81E+05
sample7	4.24E-03	276	2.21E+05
sample8	4.24E-03	276	6.72E+05
sample14	4.19E-03	272	5.00E+06
sample15	4.19E-03	272	8.11E+07
sample9	4.17E-03	271	3.58E+05
sample11	4.17E-03	271	7.22E+06
sample12	4.17E-03	271	3.26E+08
sample13	4.17E-03	271	3.95E+08
sample10	4.14E-03	269	1.00E+09
sample3	4.11E-03	267	1.00E+09
sample6	3.91E-03	254	1.00E+09
sample2	3.88E-03	252	4.95E+08
sample1	3.53E-03	229	1.00E+09

6.5. Bulk L605 specimens

6.5.1. Fatigue response

Fatigue life curves as a function of stress amplitude against the loading cycles to failure in the range of 1E+05 and 1E+09 loading cycles are presented for the three series of L605 CoCr samples in Fig. 59. The data correspond to lifetimes obtained for the smooth samples after mechanical polishing (grinding) and electropolishing as well as U-notched samples without considering the stress concentration factors for the notched samples. The resulting fatigue life for mechanically polished smooth L605 samples obtained in the range of 1E+05 and 1E+09 loading cycles is within 475-397 MPa and shows a decreasing trend up to the very high-cycle region. The fatigue resistance at 1E+09 cycles is 397 MPa and 343 MPa for the mechanically polished and electropolished smooth samples, respectively while without considering the stress concentration factors, the stress amplitude for U-notched is about 260MPa.

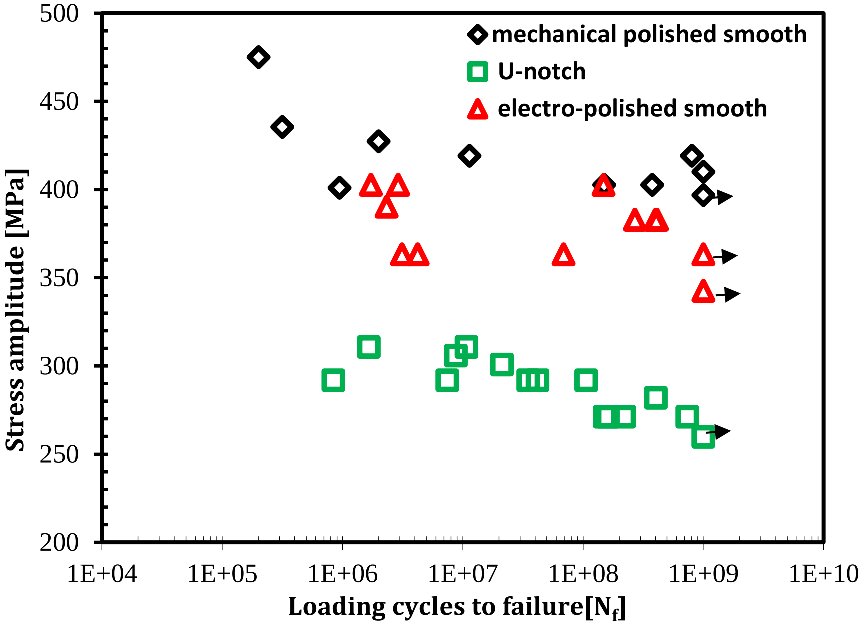

Fig. 59: Fatigue life curves of the mechanical and electro-polished plain and notched L605 samples up to 1E+09 loading cycles without considering K_t.

Table 24. Fatigue data of fatigue life curves of mechanical and electro-polished plain and notched L605 samples.

Mechanical polished Co-Cr samples	Strain at midsection of sample	Stress amplitude (MPa)	Number of cycles to failure	Report
Sample 5	1.95E-03	475	2.00E+05	
Sample 6	1.79E-03	436	3.16E+05	
Sample 7	1.76E-03	427	2.00E+06	
Sample 4	1.72E-03	419	1.13E+07	
Sample 9	1.72E-03	419	8.03E+08	
Sample 11	1.69E-03	410	1.00E+09	run-out
Sample 3	1.66E-03	403	1.50E+08	
Sample 8	1.66E-03	403	3.75E+08	
Sample 2	1.65E-03	401	9.47E+05	
Sample 10	1.63E-03	397	1.00E+09	run-out
Sample 1	1.37E-03	332	1.00E+07	
Electro- polished Co-Cr samples	Strain at midsection of sample	Stress amplitude (MPa)	Number of cycles to failure	
Sample 1	1.66E-03	403	1.72E+06	middle crack
Sample 2	1.66E-03	403	2.90E+06	crack near end/screw side
Sample 3	1.66E-03	403	1.48E+08	crack near end/screw side
Sample 4	1.61E-03	390	2.32E+06	crack near end/screw side
Sample 5	1.58E-03	383	2.69E+08	near middle/towards screw
Sample 6	1.58E-03	383	4.00E+08	middle crack
Sample 7	1.58E-03	383	4.12E+08	near middle/towards screw
Sample 8	1.49E-03	363	3.13E+06	middlecrack
Sample 9	1.49E-03	363	4.22E+06	near middle/towards screw
Sample10	1.49E-03	363	6.89E+07	near middle
Sample11	1.49E-03	363	1.00E+09	run-out
Sample12	1.41E-03	343	1.00E+09	run-out
U-notch Co-Cr samples	Strain at midsection of sample	Stress amplitude (MPa)	Number of cycles to failure	
Sample12	1.28E-03	450	1.66E+06	
Sample14	1.28E-03	450	1.08E+07	
Sample13	1.26E-03	443	8.76E+06	
Sample11	1.24E-03	436	2.13E+07	
Sample1	1.20E-03	423	8.40E+05	
Sample7	1.20E-03	423	7.44E+06	
Sample8	1.20E-03	423	3.52E+07	
Sample9	1.20E-03	423	4.18E+07	
Sample10	1.20E-03	423	1.06E+08	
Sample6	1.16E-03	409	4.05E+08	
Sample2	1.12E-03	393	1.52E+08	
Sample3	1.12E-03	393	1.61E+08	
Sample4	1.12E-03	393	2.20E+08	
Sample5	1.12E-03	393	7.35E+08	
Sample15	1.07E-03	376	1.00E+09	run-out

The reduction of the fatigue strength of L605 samples after electropolishing can be related to the effect of residual stresses on the fatigue behaviour as also observed in other studies [148], [149].

M. Goto et al. studied the fatigue damage of a high carbon chromium steel SUJ2, with rotating bending fatigue tests of smooth specimens finished by the grinding and electropolishing. They observed that removing the surface layer by electropolishing results in a decreased surface hardness and compressive residual stresses and consequently a reduction in the fatigue strength. On the other words, the higher resistance observed in ground specimen results from the surface strengthened layer (work hardening and residual stresses) due to grinding [148]. Sohar et al. investigated the effect of surface compressive residual stresses induced by surface grinding and polishing on the high cycle fatigue behavior of medium-carbon high-chromium alloy cold work tool steel. They found that the fatigue strength of the diamond polished specimens with low residual stresses was lower than the polished specimens with high compressive residual stresses at the surface [149].

Comparison of theoretical stress concentration factor (K_t=1.83) with experimentally determined fatigue stress concentration factor (K_f=1,42) showed that the obtained value of stress concentration factor is lower than that theoretical stress concentration factor. Using these data fatigue notch sensitivity factor (q) of L605 alloy was determined by using (Eq. 6.3) which is q=0.50. It can be seen that L605 alloy is less notch sensitive compared to Ti-45Nb with q=0.89.

6.5.2. Fracture surface analysis

SEM techniques were applied for examination of the fracture surfaces and failure analysis of the L605 samples. In most cases, final rupture did not occur during the loading of the smooth L605 samples and the measurements were stopped after separation of about 40% of the cross sectional area. This probably occurred due to high toughness of the material resulting in a slower growth rate during the stage 2 of fatigue life as discussed later. As the change in the resonance frequency of the sample exceeds the pre-set range of +/- 200 Hz, as the failure criteria, the ultrasonic testing system stops the measurements. Thus, these samples were cooled in liquid nitrogen and were broken in a brittle manner in order to examine the fracture surfaces. Full crack propagation and final rupture were observed for U-notched samples. Typical fatigue fracture surfaces of smooth electro-polished and U- grooved bulk L605 specimens are presented in Figs 60-67.

The overview fracture surface in Figs. 60a to 63a show a faceted topography at the initiation sites from which the cracks grow and expand radially through the sample and build a semi-circular shape. The rough surface beyond this region corresponds to the broken area as stated above. The detail images in Figs 60-63 show clearly that independent from the stress amplitude and the number of loading cycles almost all the cracks initiated at the surface (e.g. Figs 60 and 62) or near the surface in larger grains or grain agglomerates (e.g. 64). The cleavage type of fracture of the surface grains indicated cracking along the slip bands which were formed during the early stages of cyclic deformation. In the case of smooth samples, failure was found to be related mainly to crack initiation at large “soft” surface grains or grain colonies with similar orientation.

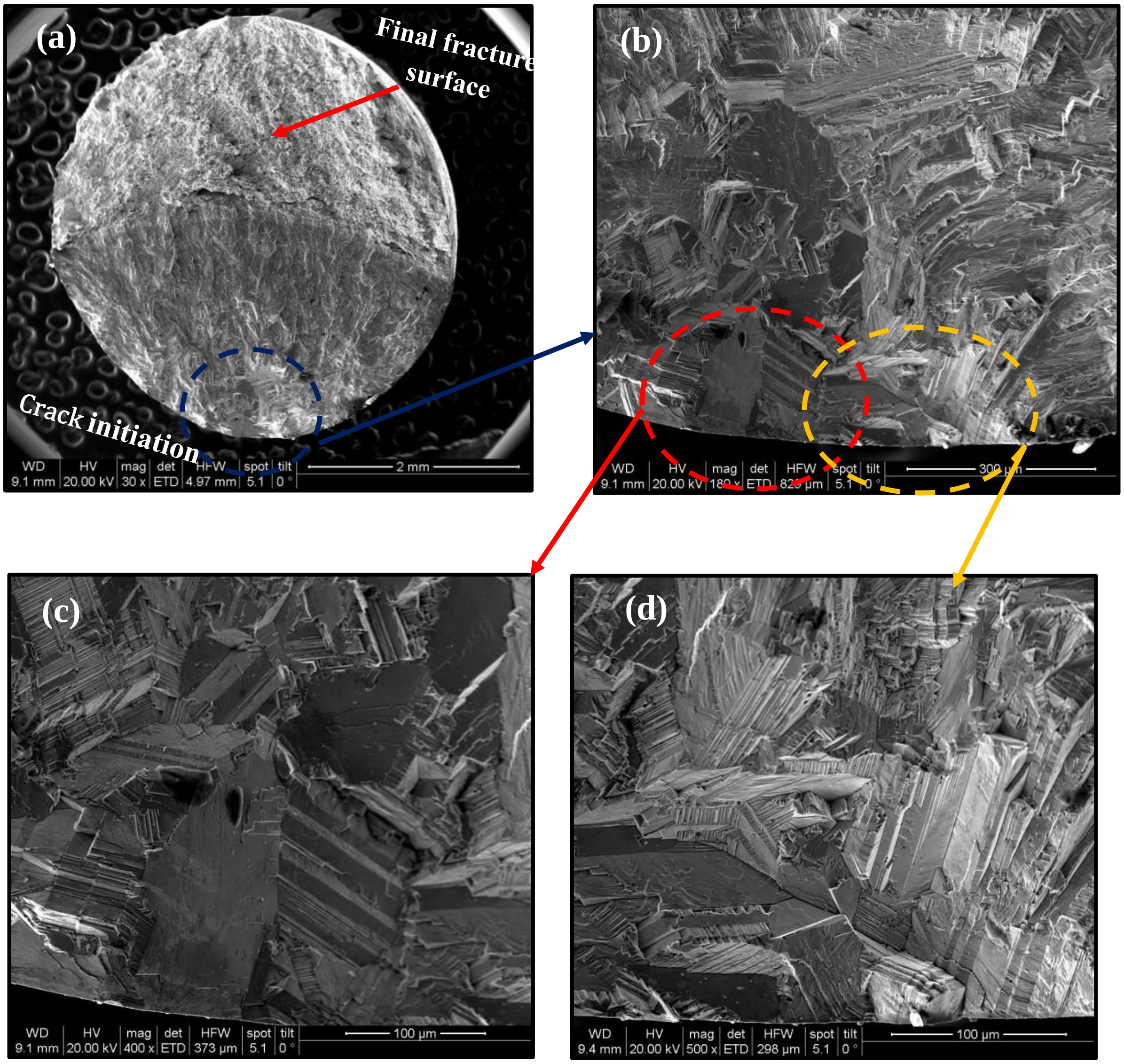

Fig. 60: Typical fatigue fracture surface of smooth electro polished bulk L605 sample failed at $\frac{\Delta\sigma}{2}$ = 363 MPa, N_f =3.13E+06 (a) overview, (b) detail of (a), (c, d) details of (b).

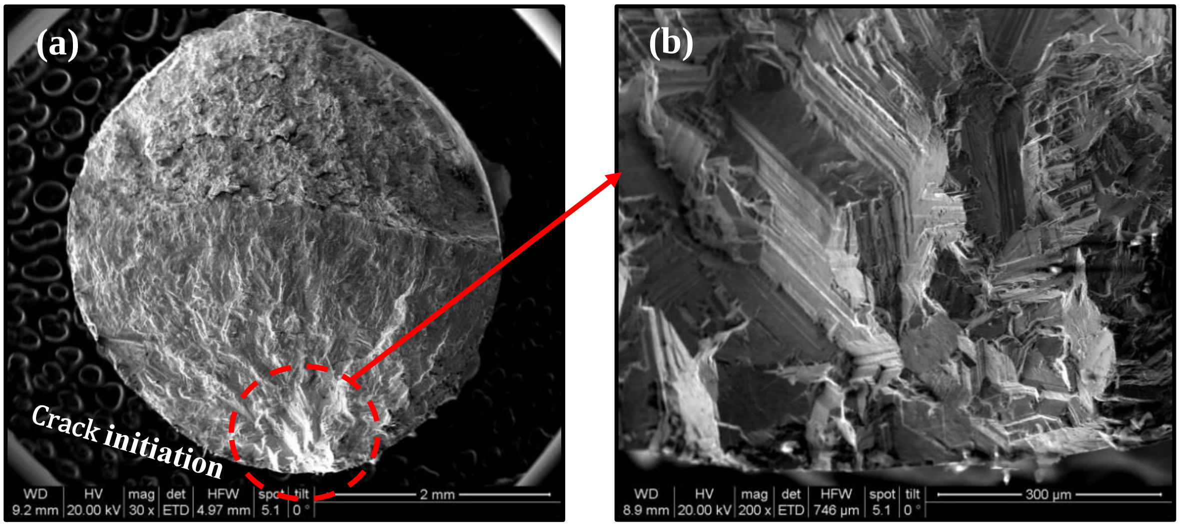

Fig. 61: Typical fatigue fracture surface of smooth electro polished bulk L605 sample failed at $\frac{\Delta\sigma}{2}$ = 363 MPa, N_f =6.89E+07 (a) overview, (b) detail of (a).

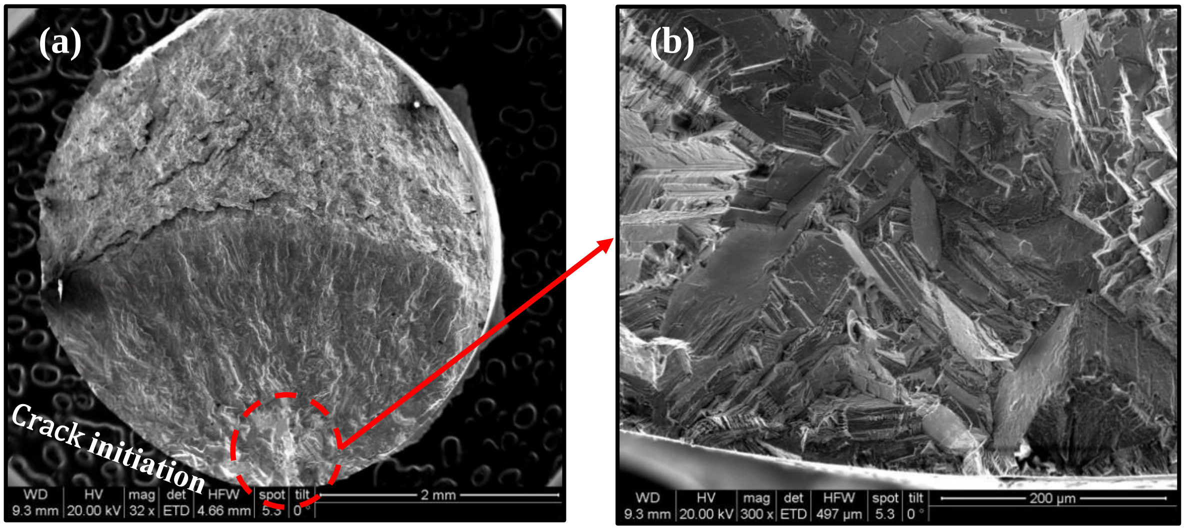

Fig. 62: Typical fatigue fracture surface of smooth electro polished bulk L605 sample failed at $\frac{\Delta\sigma}{2}$ = 383 MPa, N_f =4.00E+08 (a) overview, (b) detail of (a).

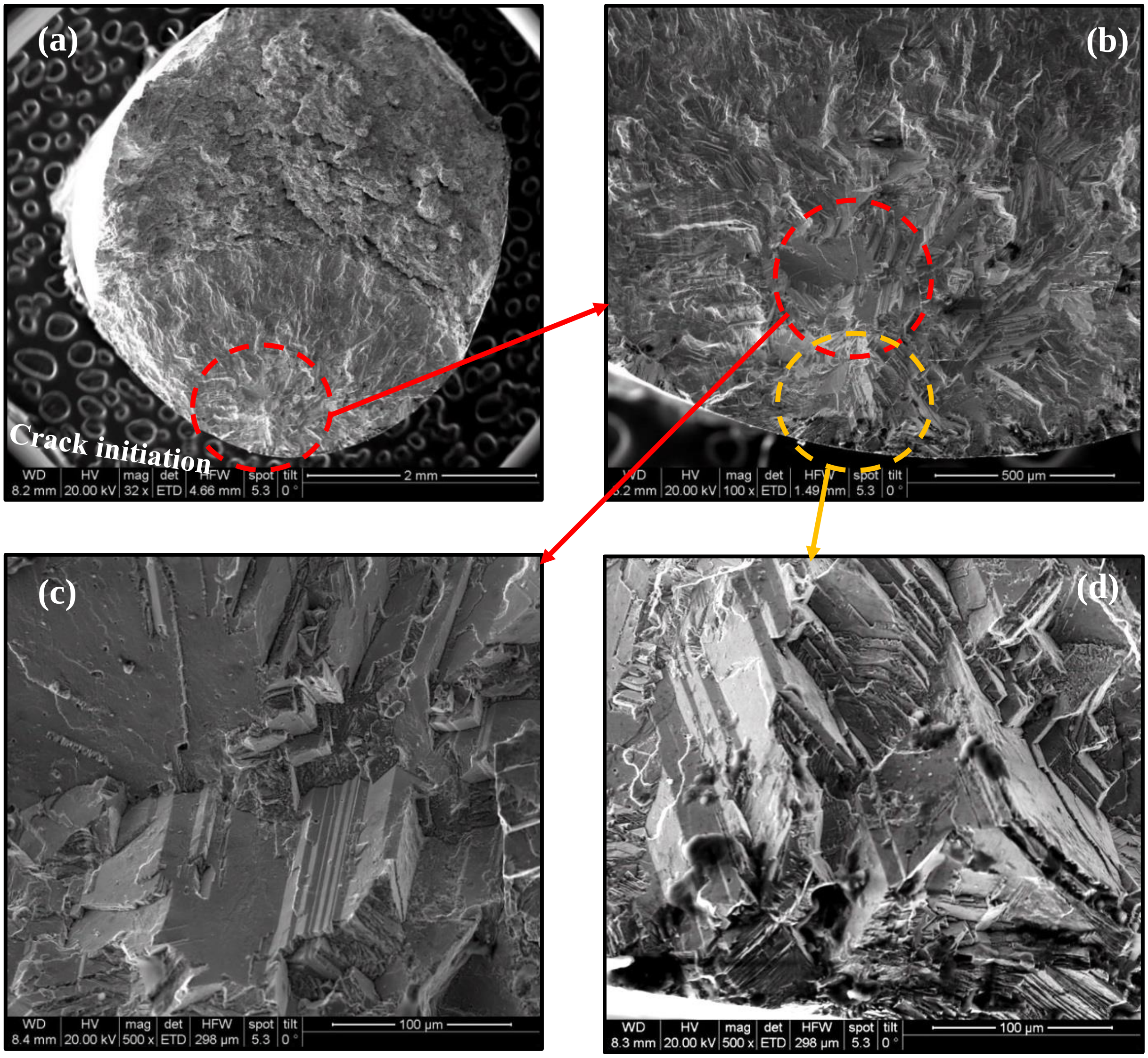

Fig. 63: Typical fatigue fracture surface of smooth electro polished bulk L605 sample failed at $\frac{\Delta\sigma}{2} = 383$ MPa, N_f =2.69E+08 (a) overview, (b) detail of (a), (c, d) detail of (b).

Typical fracture surfaces of U-grooved L605 samples are shown in Figs 64-67. The crack initiation site is again located at the periphery of the sample featuring a crystallographic morphology (Fig 64 b). In this case due to the high stress concentration caused by the notch, the fatigue crack growth area is extended through the samples and the final rupture occurs in a ductile manner covering a small area as presented in Fig. 64c. The detail images shown in Figs. 65-67 indicate presence of a considerable amount Cr and W carbide particles close to the surface at the initiation site as confirmed by EDX analysis of the fracture surface (Fig.68).

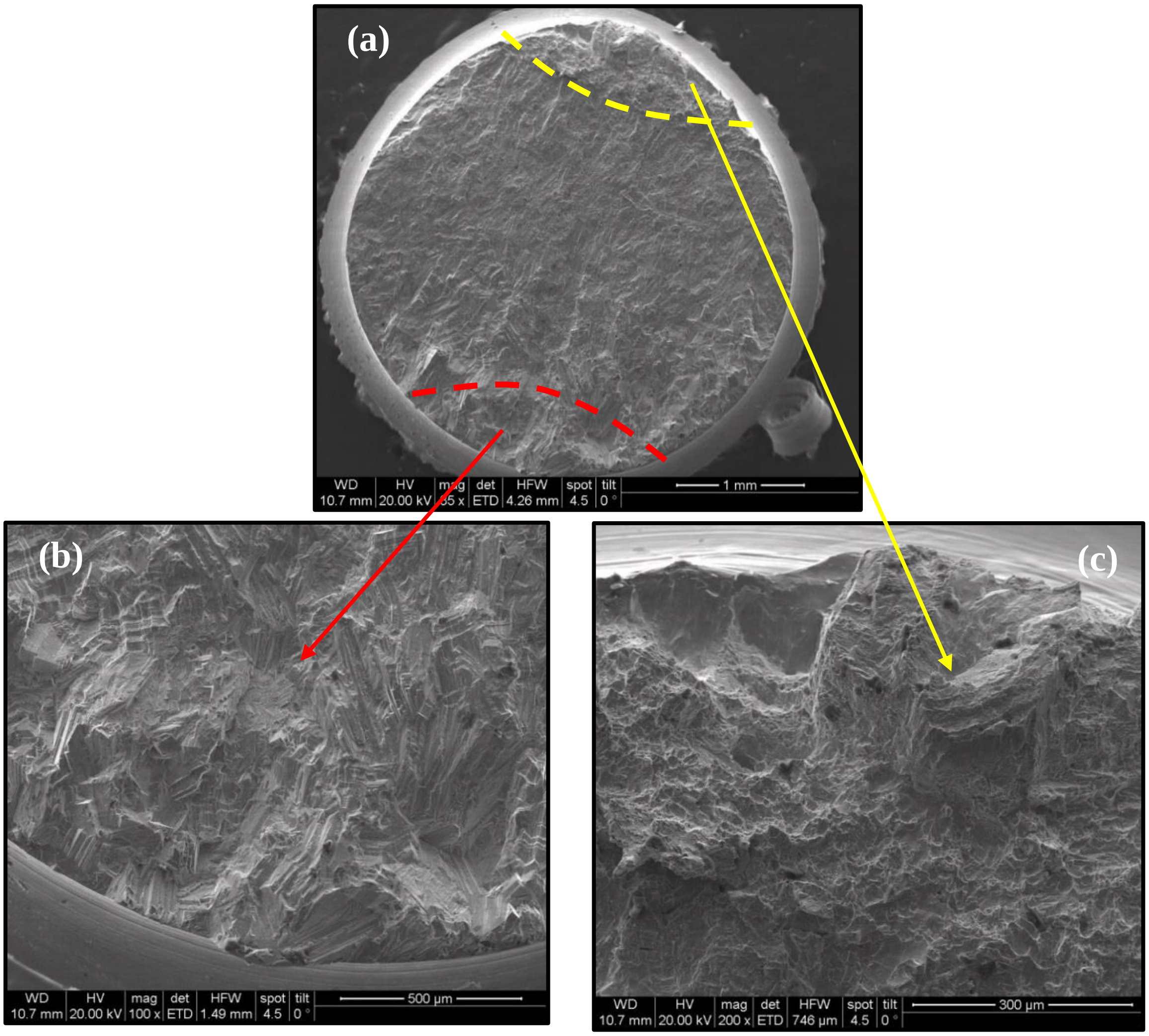

Fig. 64: Typical fatigue fracture surface of U-grooved bulk L605 sample failed at $\frac{\Delta\sigma}{2}$ = 307 MPa, N_f =3.69E+06 (a) overview, (b) crack initiation site, (c) final rupture region.

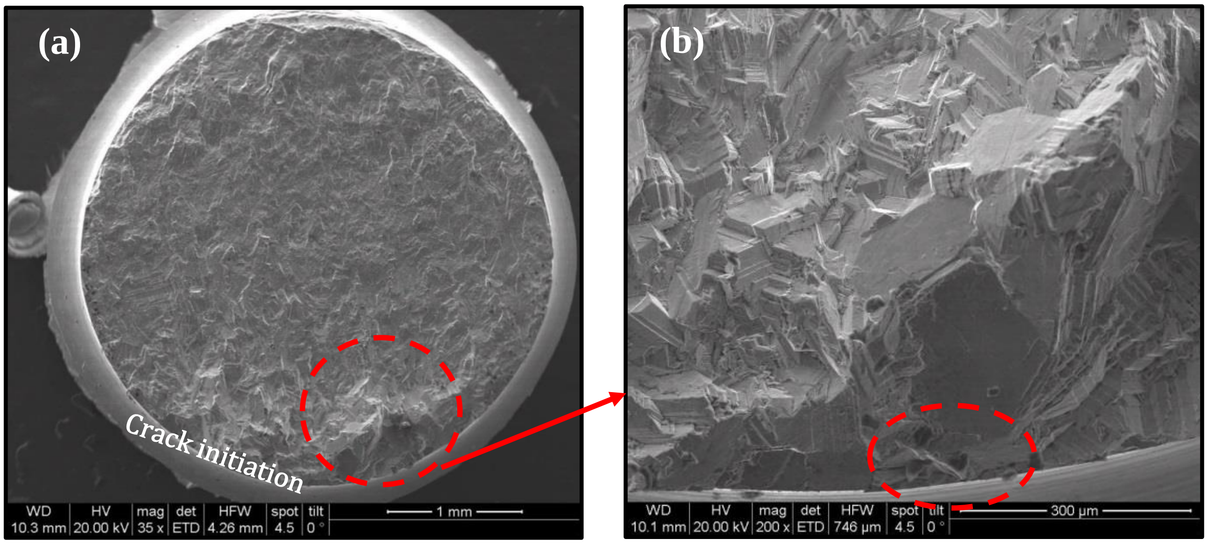

Fig. 65: Typical fatigue fracture surface of U-grooved bulk L605 sample failed at $\frac{\Delta\sigma}{2}$ = 307 MPa, N_f =9.36E+08 (a) overview, (b) detail of (a).

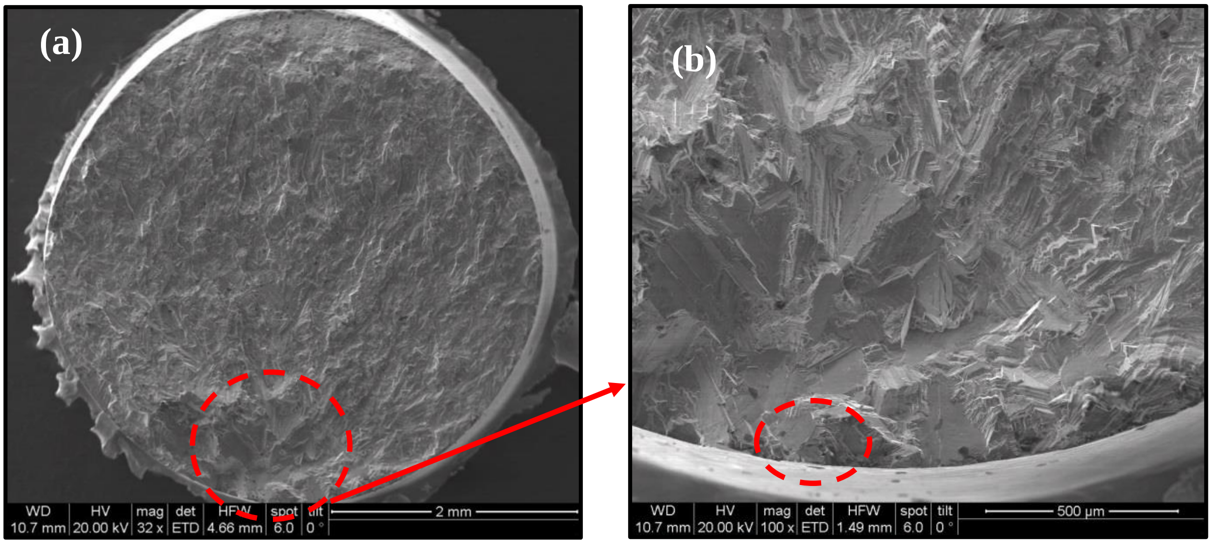

Fig. 66: Typical fatigue fracture surface of U-grooved bulk L605 sample failed at $\frac{\Delta\sigma}{2}$ = 393 MPa, N_f =7.359E+08 (a) overview, (b) detail of (a).

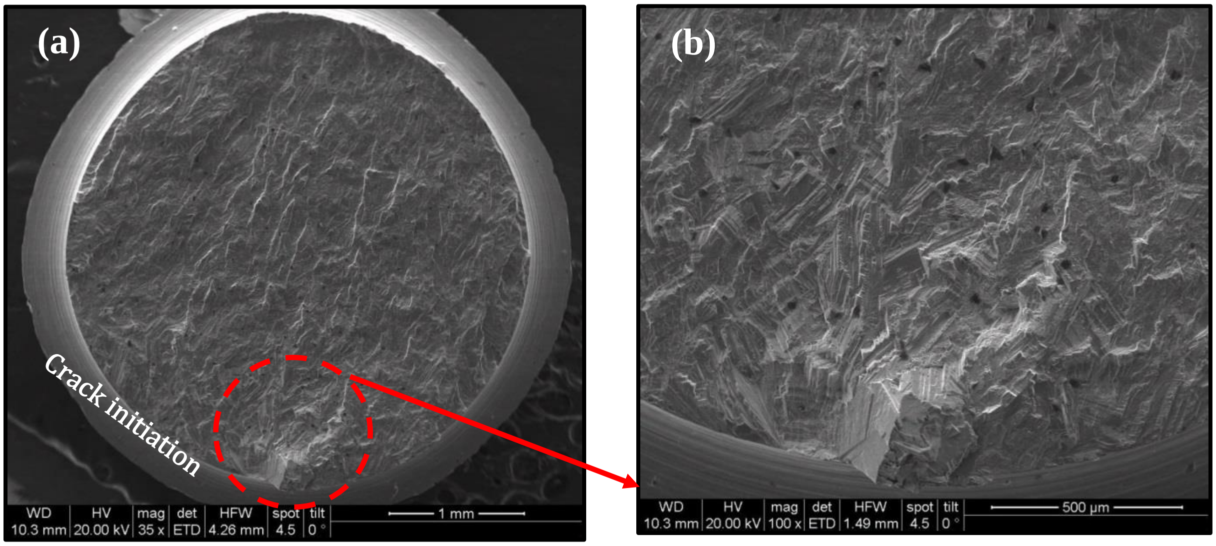

Fig. 67: Typical fatigue fracture surface of U-grooved bulk L605 sample failed at $\frac{\Delta\sigma}{2}$ = 423 MPa, N_f =7.44E+06 (a) overview, (b) detail of (a).

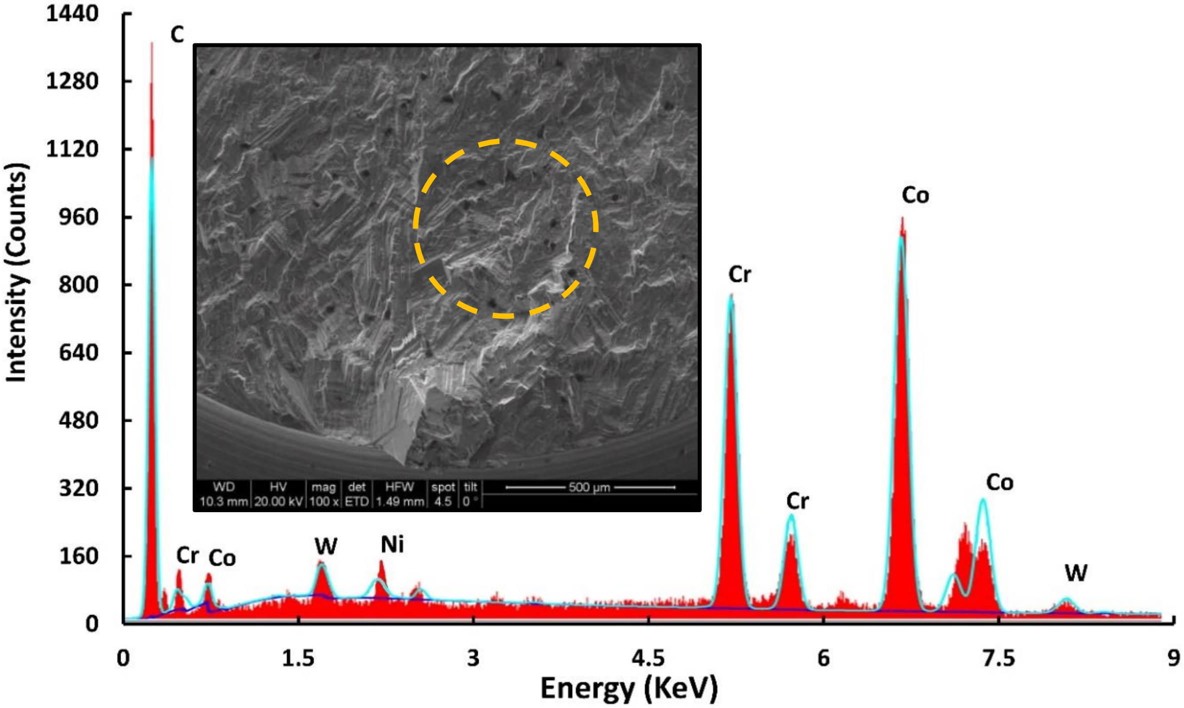

Fig. 68: EDX spectrum of black points of U-grooved bulk L605 sample failed at $\frac{\Delta\sigma}{2}$ = 423 MPa, N_f =7.44E+06.

Figures 69 and 70 show the plastically deformed area with fine and coarse slip lines along the crack path at the surface of a fatigued smooth sample after failure at 1.72e6 loading cycles. In this sample, it is assumed that the fatigue crack started to grow at the marked area due to formation of extensive extrusions and intrusions in a few large grains with suitable orientations. Initiation and growth of micro crack resulted in crystallographic fracture along the slip planes of these grains and propagation of the fatigue crack during the further cyling. The crack path shows a considerable amount of crack branching and deflection which indicates a strong interaction with grain- and twin boundaries at the periphery of the sample. Considering the fracture surface morphologies shown in Figs 60 and 67, it is evident that the crack mainly grew perpendicular to the loading axis during the stage II.

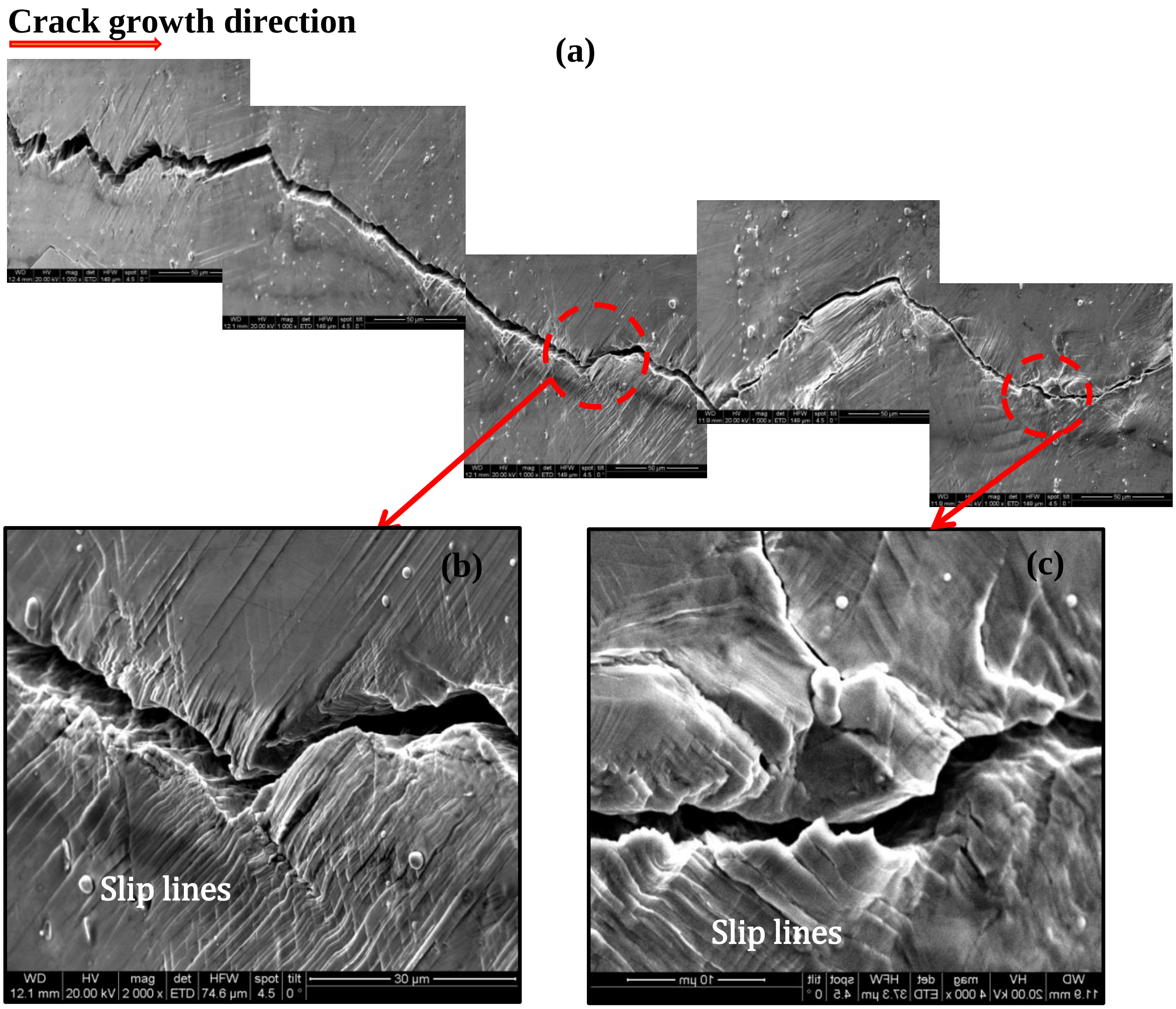

Fig. 69: SEM images of a crack profile grown under cyclic loading of the electro polishing smooth L605 specimen loaded at 403 MPa and fractured after 1.72E+06. (a) Overview of the crack initiation and crack growth, (b, c) magnified views of the crack regions shown visible slip lines. The blue arrow indicates the direction of the crack growth.

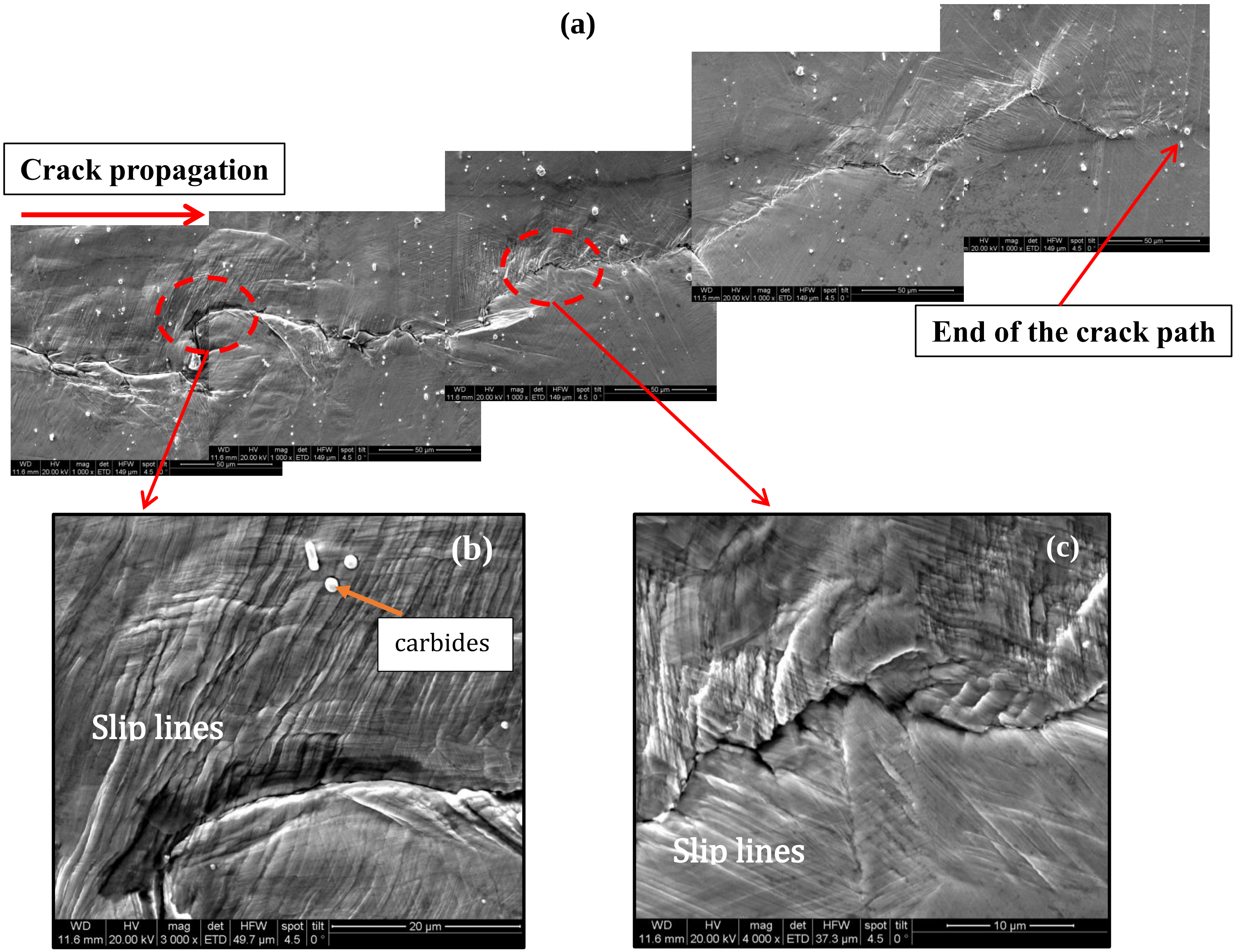

Fig. 70: SEM images of a crack profile grown under cyclic loading of the electro polishing smooth L605 specimen loaded at 403 MPa and fractured after 1.72E+06. (a) Overview of the rest crack propagation until the end of the crack, (b, c) magnified views of the crack regions shown visible slip lines.

For a better understanding and explanation of the observed failure mechanisms, metallographic samples were prepared from longitudinal cuts along the main axis of the selected smooth fatigued samples before full separation. The micrographs presented in Figs. 71 - 75 show the profiles of the fatigue cracks in the midsection of the samples and their interaction with the microstructural features of the L605 alloy. The severe crack deflection and branching observed in Fig 71c corresponds very well to the faceted and rough fracture topography which was observed in the areas close to the surface of the samples (Figs 60-63). This behaviour indicates also a high fracture resistance of the tough L605 materials with a coarse and strongly twinned microstructure. The BSE images presented in Figs. 71, 72 and 74 also reveal the distribution of Cr and W carbides with diameters of a few microns up to about 5 µm near to the crack path. However, in this investigation a notable interaction of the carbide particles with the crack path is not observed.

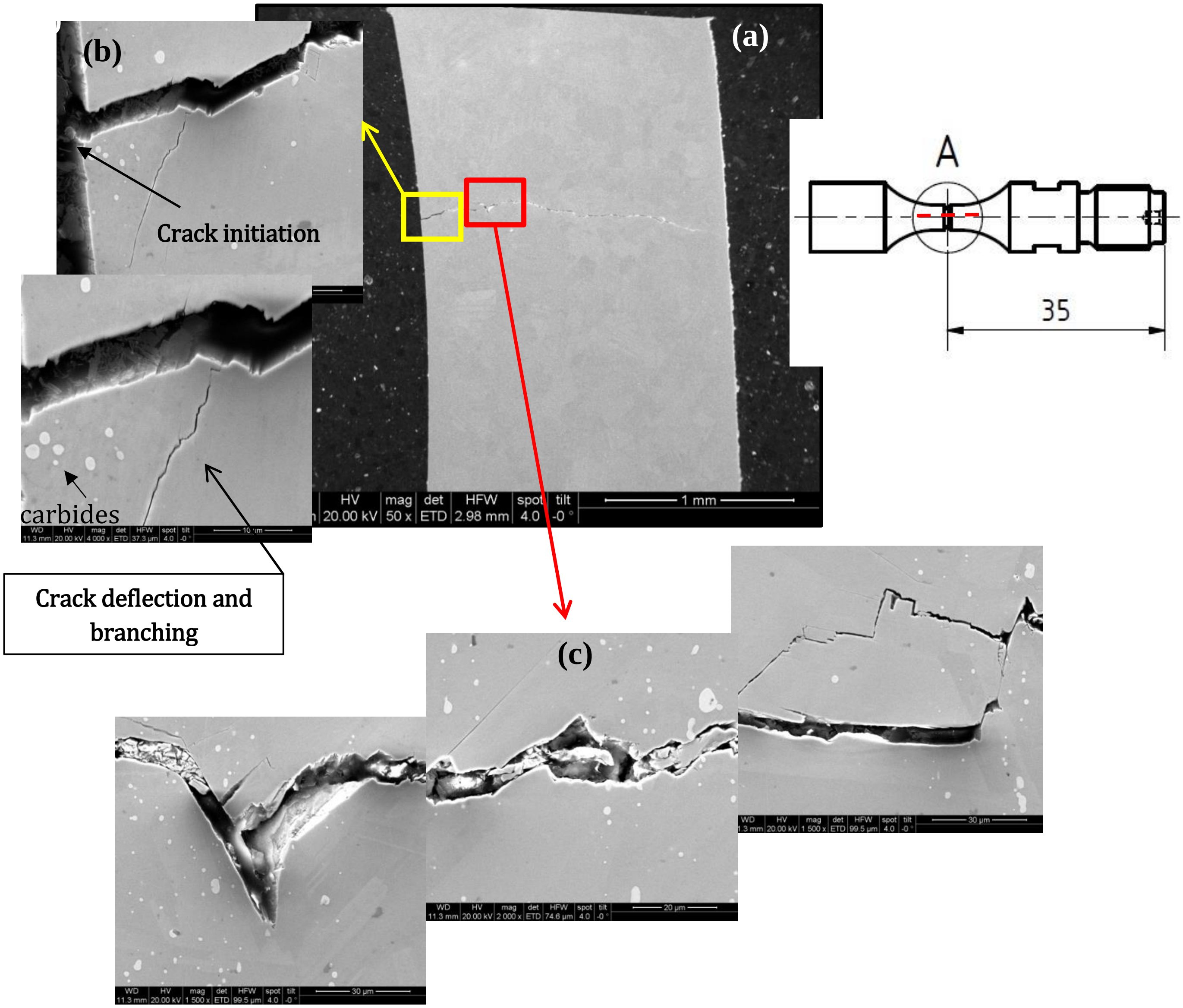

Fig. 71: SEM images of a crack profile grown under cyclic loading of the mechanical polishing smooth L605 specimen loaded at 419 MPa and fractured after 8.03E+08. (a) An overview of the crack path, (b) crack initiation site, (c) intergranular crack propagation at a high magnification.

Fig. 72 and the related EBSD images (Fig. 73) shows that in this case the crack initially propagated with a zig-zag shape and became progressively flat with further growth through the sample. The boundary map of the beginning of the crack path near the surface (Fig. 72c) with the corresponding EBSD image (Fig. 73a), reveal the distribution of the grains with an orientation close to (101) at this location. The crack grew in an intergranular manner within the grain boundaries of a few grains of similar orientation along a length of about 300 µm and then followed a transgranular path perpendicular to the loading axis. Similar fatigue crack process can be seen in Figs. 74-76**.**

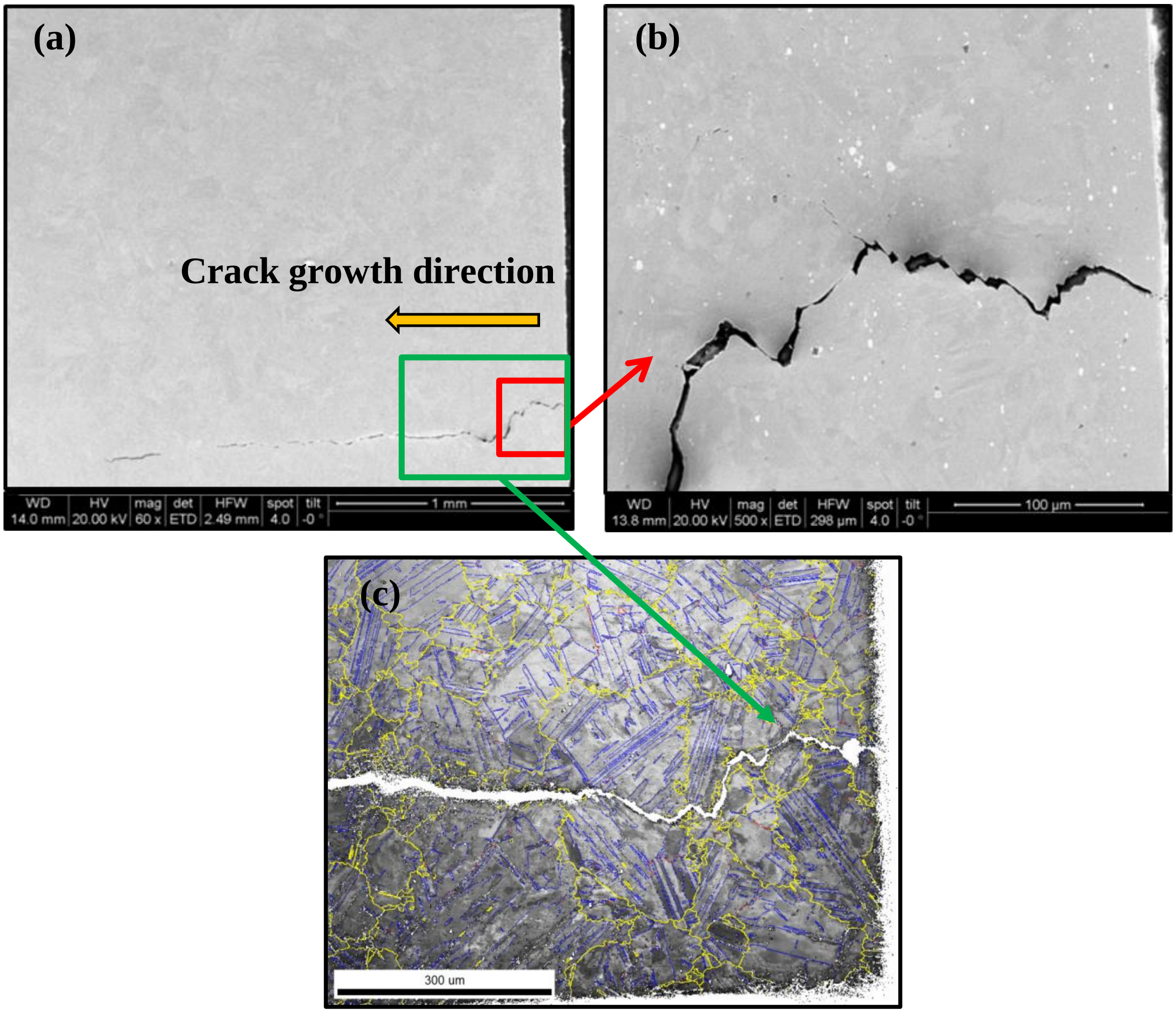

Fig. 72: SEM images of a crack profile grown under cyclic loading of the mechanical polishing smooth L605 specimen loaded at 436 MPa fractured after 3.16E+05. (a) An overview of the crack path, (b) crack initiation site,(c) magnified grain boundary map of crack initiation sit. The red arrow indicates the direction of the crack growth.

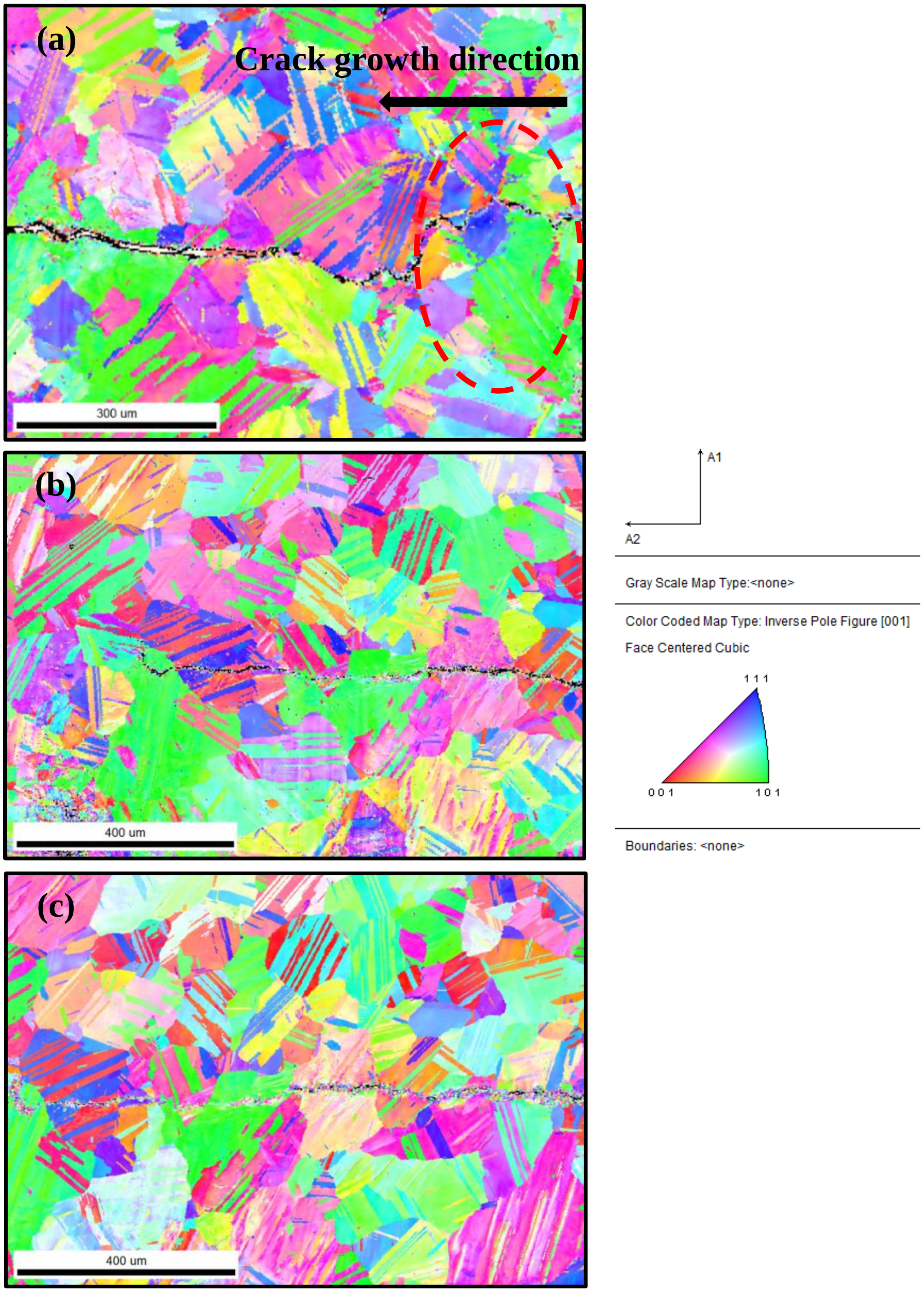

Fig. 73: The EBSD analysis of the crack path: IPF map of the (a) crack initiation site, (b) middle of the crack path and (c) end of the crack path, in a fatigued mechanically polished smooth L605 specimen loaded at 436 MP and fractured very soon after 3.16E+05 cycles.

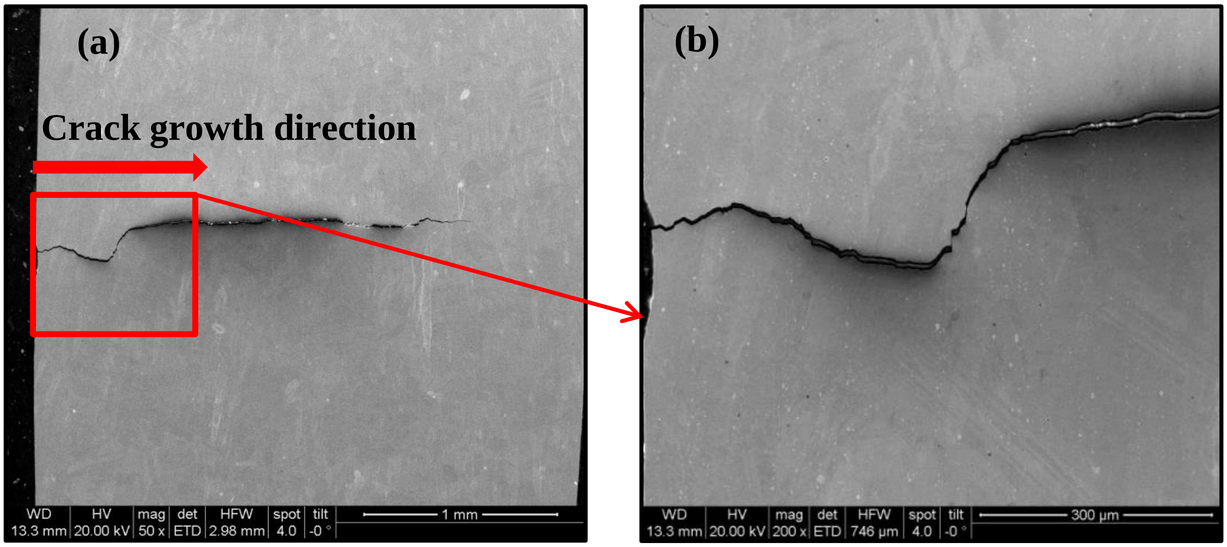

Fig. 74: SEM images of a crack profile grown under cyclic loading of the mechanical polishing smooth L605 specimen loaded at 419 MPa fractured after 1.13E+07. (a) An overview of the crack path, (b) crack initiation site. The blue arrow indicates the direction of the crack growth.

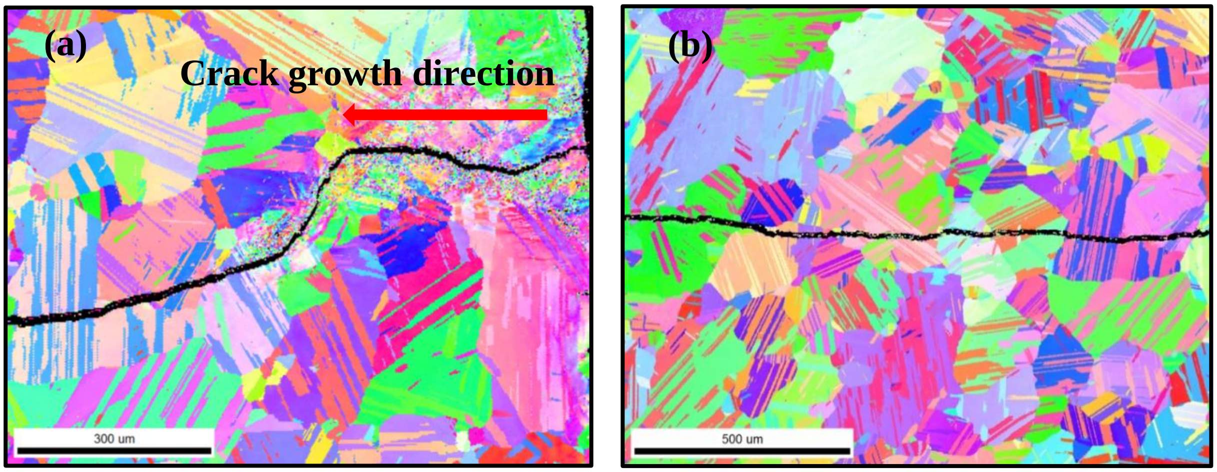

Fig. 75: The EBSD analysis of the crack path: IPF map of the (a) crack initiation site, (b) grain map of the middle of the crack path with twins in a fatigued mechanically polished smooth L605 specimen loaded at 419 MP and fractured very soon after 1.13E+05 cycles.

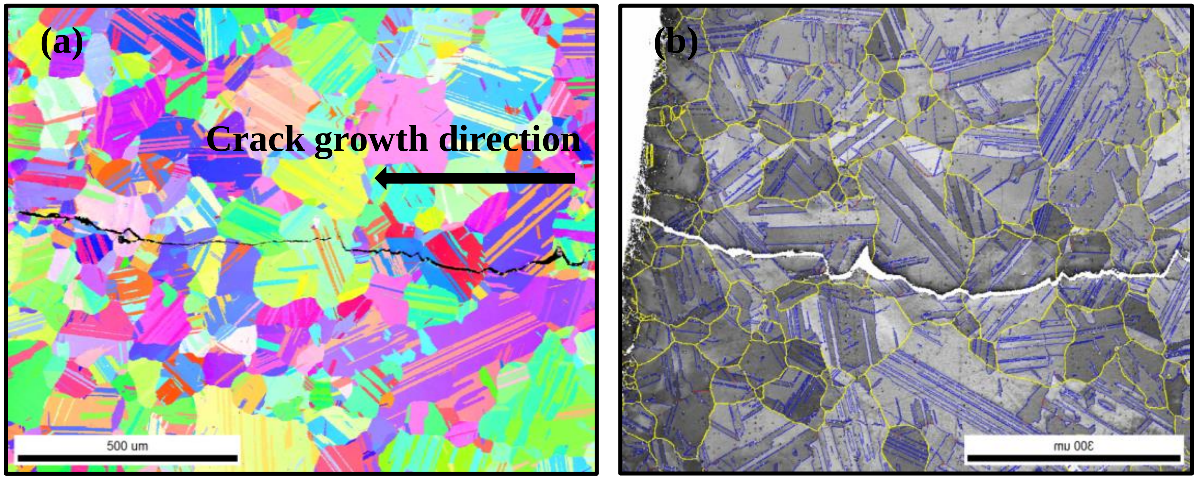

Fig. 76: The EBSD analysis of the crack path of the mechanical polishing smooth L605 specimen loaded at 419 MPa and fractured after 8.03E+08: IPF map of the (a) grain map of the overview of the crack path with twins (b) magnified grain boundary map.

The micrographs presented in Figs. 71 and 76 along with the microstructural and fracture surface analysis of the samples suggest the following mechanism for fatigue crack growth in L605 alloy. The fatigue crack initiation (stage 1) at the surfaces of samples includes the movement of dislocations localized in the primary slip planes of a few grains with approximately 45° to the tensile axis, followed by the formation of intrusions (notches) and extrusions (ridges) at the surface. The microstructure of the investigated L605 consists of large grains with a considerable proportion of twinning and an average size of 75 - 203 µm. The initiated micro cracks either followed the primary slip plane in the large and softer grains resulting in a trans-granular fracture, or proceeded within a colony of smaller grains of similar orientation in an inter-granular manner. Then at the propagation stage (stage 2) the direction of the crack changed and it propagated roughly perpendicular to the applied stress until final catastrophic failure. As mentioned before, in this study the last stage was mainly observed in notched samples. The schematic illustration in Fig. 77 is representative for the fatigue failure of the L605 alloy of the present study.

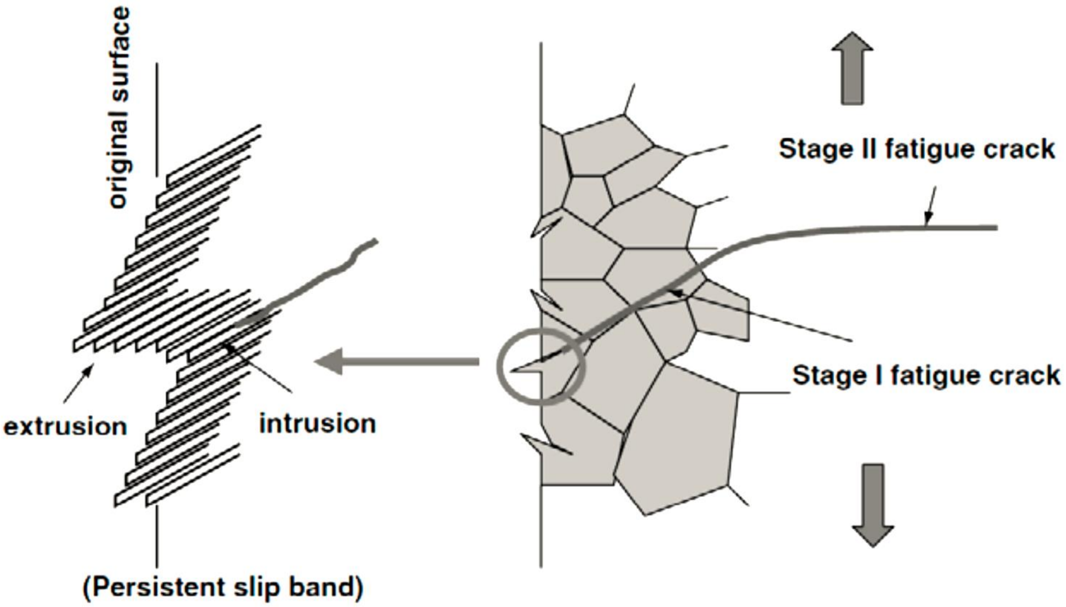

Fig. 77: Different stages of fatigue failure including process of fatigue crack initiation and growth.

6.6. Comparison of high cycle fatigue life of Ti45Nb and L605 alloys with lifetime of Ti, Nb and Ti- biocompatible alloys

S-N curves of smooth and U-notched shaped Ti-45Nb and L605 samples are shown in Fig. 78. The fatigue resistance of the smooth Ti-45Nb and L605 samples at 1E+09 cycles is 260 MPa and 397 MPa respectively, while without considering the stress concentration factors, the stress amplitude for U-notched Ti-45Nb and L605 samples is about 147 and 260 MPa, respectively. According to the obtained results L605 alloy showed a considerably better fatigue performance than that of Ti-45Nb material. However, Ti-45Nb alloy has significantly lower elastic modulus of about 65 GPa in comparison with that of L605 with a value of about 242 GPa.

Fatigue data of smooth Ti45Nb and Co-Cr L605 samples are also plotted in Fig. 79 using a strain-life diagram. Contrary to the fatigue life plots (Fig. 78), strain-life diagram i.e. normalized stress life data (stress/E) of smooth Ti45Nb samples lies above the plot of Co-Cr L605 samples. The strain amplitude of the smooth Ti-45Nb and L605 samples at 1E+09 loading cycles is approximately 0.39 and 0.17%, respectively. A summary of static and dynamic mechanical properties of Co-Cr L605 and Ti-45Nb alloys is given in Table 25.

Table 25. Comparison of static and dynamic properties of Co-Cr L605 and Ti-45Nb alloys.

Sample	UTS [MPa]	Yield strength [MPa]	Young's Modulus [GPa]	Micro Vickers Hardness [GPa]	Nanohardness [GPa]	Average Grain Size [µm]	K_f	q
L605	**1021±27**	**434±32**	**242.2±2.9**	**3.52±0.3**	**3.83±0.14**	**70-200**	**1.42**	**0.50**
Ti-45Nb	**446±12**	**430±21**	**65.4±2.1**	**1.32±0.02**	**1.42±0.02**	**20**	**1.79**	**0.95**

A comparison of high cycle fatigue life of Ti-45Nb and Co-Cr alloys with lifetime of Ti, Nb and Ti-alloys tested at 20kHz can be seen in Fig. 80 [18], [20] and the corresponding material properties are given in table 26. As seen, the fatigue limits of ($\alpha + \beta$)-type Ti alloys such as Ti–6Al–7Nb and Ti–6Al–4V are greater than those of α and β-type titanium alloys. The fatigue life curve of Co-Cr L605 alloy lies below the plot of Ti–6Al–4V and the fatigue strength of Ti-45Nb and Nb alloys are in a similar range. To compare the cyclic fatigue resistance of these Ti-based alloys and Co-Cr L605 alloy their different values of Young's moduli should be considered being the most important issue in application of biocompatible metallic materials due to the occurrence of bone atrophy because of the stress shielding between the implant and bone.

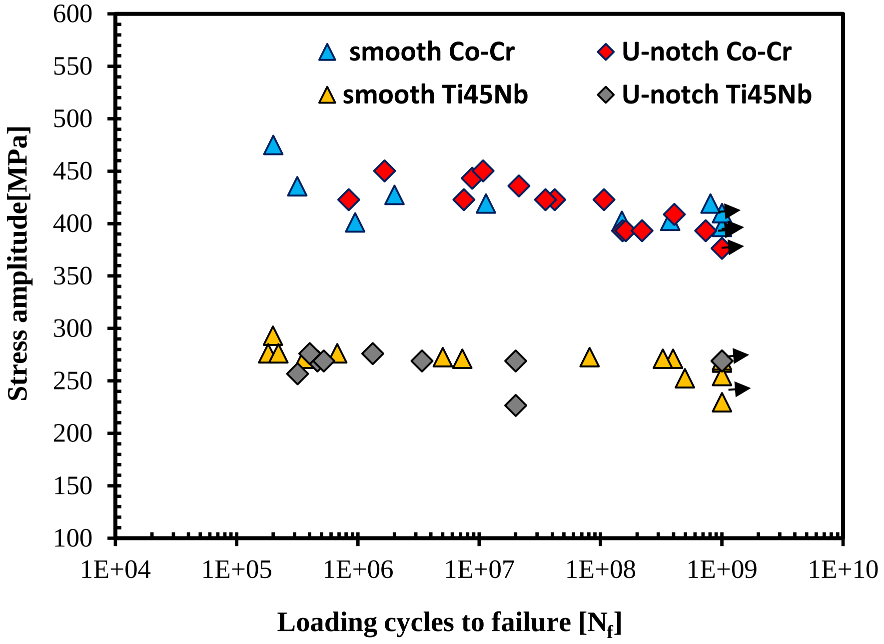

Fig. 78: Comparison of high cycle fatigue life of Ti45Nb alloy with lifetime of Co-Cr L605 alloy with considering the notch effect (K_t).

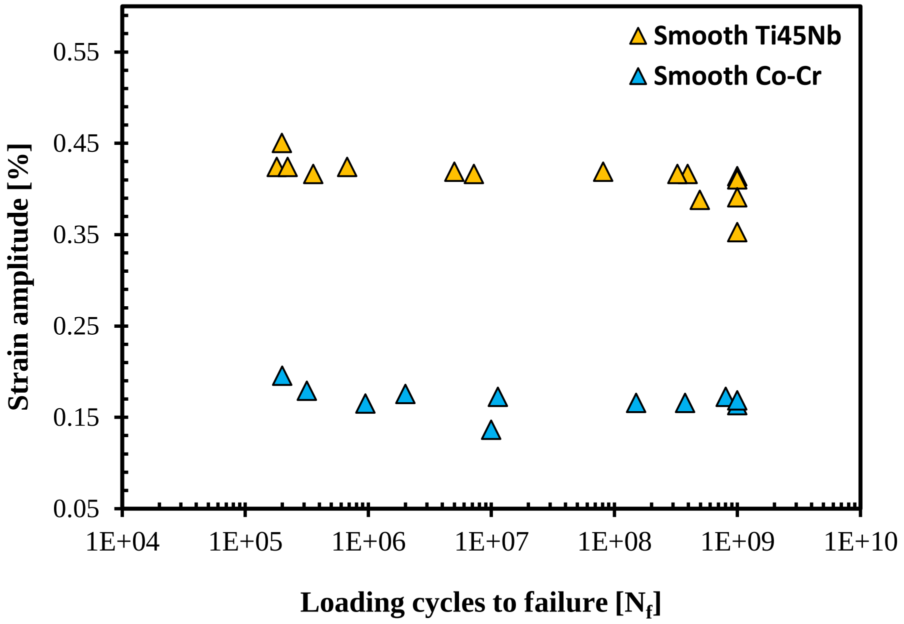

Fig. 79: Comparison of strain-life plots of smooth Ti45Nb and Co-Cr L605 alloys.

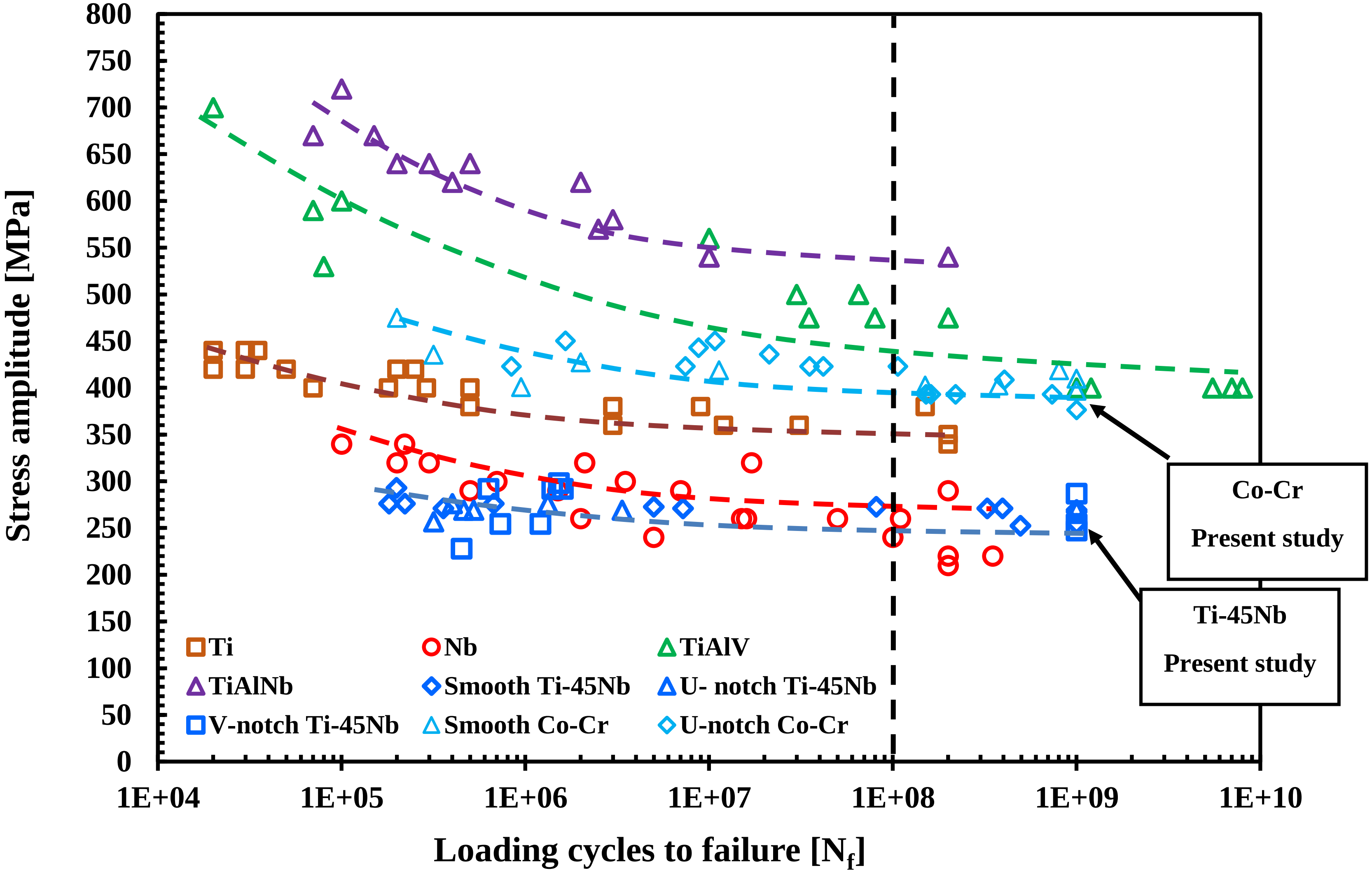

Fig. 80: A comparison of high cycle fatigue life of L605 and Ti45Nb alloys with lifetime of Ti, Nb and Ti-alloys [18], [20].

Table 26. Comparison of mechanical properties and structures of Ti-alloys, Ti, Nb, Ti-45Nb and Co-Cr L605 alloys.

Material	E (GPa)	UTS (MPa)	Fatigue at 1e8	Structure
Ti-6Al-7Nb	105	953	540	α+β
Ti-6Al-4V	114	1050	430	α+β
Ti	116	522	340	hcp – α phase
Nb	105	385	290	bcc – β phase
Ti-45Nb	65	446	250	bcc – β phase
Co-Cr L605	242	1021	410	fcc - γ phase

Chapter 7: Summary, Conclusions and Outlook

The mechanical properties and high cycle fatigue behavior of ß-type Ti-45Nb and γ-type Co-Cr L605 alloys were studied. High pressure torsion (HPT) process was applied for grain refinement and improvement of the mechanical properties of the low modulus Ti-45Nb alloy. Fatigue investigations were performed on conventional (CG) and ultrafine grained (UFG) small scaled Ti-45Nb samples with different geometries. In order to consider the design aspects of the medical implants and to determine the notch sensitivity of the Ti-45Nb and L605 alloys, fatigue response of the smooth and notched bulk samples up to 1E+09 loading was studied and compared. The effects of surface finish characteristics on the lifetime of L605 Co-Cr alloy was studied by using two series of smooth bulk samples the surfaces of which was prepared by mechanical polishing (MP) and electropolishing (EP).

The Ti-45Nb samples processed by HPT showed a considerable increase of hardness and strength due to the significant grain refinement while maintaining a low Young's modulus of about 65 GPa. Ultrasonic fatigue tests were conducted to obtain lifetime curves for the CG and UFG miniaturized samples which were plotted by using the calculated volume averaged stress against loading cycles to failure. The results showed only a slight improvement of the fatigue resistance of the UFG material with superior tensile properties. In order to explain this unexpected behavior, careful microstructural and texture analysis were performed which confirmed the microstructural stability of the UFG Ti-45Nb alloy and absence of grain coarsening up to the very high cycle regime. Cyclic softening effects were found in terms of a gradual reduction of hardness and dislocation density with increasing the loading cycles from 1e6 to 1e9. According to our findings, the moderate fatigue performance of the UFG Ti-45Nb is more likely related to the early crack initiation due to the geometrical effects in the notch sensitive alloy and the rapid crack growth which is known as a common feature in nano- and ultrafine grained materials. The fatigue resistance of the smooth miniaturized and bulk Ti-45Nb as well L605 samples at 1E+09 cycles was determined to be 216, 260 and 397 MPa respectively. Without considering the stress concentration factors, the stress amplitude for U-notched bulk Ti-45Nb and L605 samples was found to be about 147 and 260 MPa, respectively. The smooth miniaturized Ti-45Nb samples with a rectangular cross section showed the lower fatigue resistance in comparison with the smooth bulk Ti-45Nb samples with circular cross section which can be mainly explained by the influence of sample size and geometry. The fatigue resistance at 1E+09 cycles for electropolished smooth L605 samples was 343 MPa. The fatigue strength of electropolished smooth L605 specimens was lower than those prepared by mechanical polishing which can be mainly related to the effect of residual stresses on the fatigue response. According to the obtained results L605 alloy showed much better cyclic fatigue performance than their Ti-45Nb counterparts. However, Ti-45Nb alloy has significantly lower elastic modulus of about 65GPa in comparison with L605 with an elastic modulus of about 242GPa. Examination of the fracture surfaces of the fatigued Ti-45Nb and L6045 samples showed two different mechanisms of crack initiation. A strong dependency of the fatigue lives of Ti-45Nb specimens with the location of microstructural inhomogeneities or defects was observed. Independent of the stress amplitude, failures up to a maximum of 1E+07 were mainly caused due to crack initiation from one or several locations at the periphery of the samples. Those which survived up to higher loading cycles finally failed due to internal crack initiation. Typical fatigue fracture surfaces of the bulk coarse grained L605 specimens showed that independent of the stress amplitude and the number of loading cycles almost all the cracks were initiated at or near the surface due to the existence of large grains or a number of smaller neighbouring grains with a soft orientation. The experimentally determined K_f values for both Ti-45Nb and L605 alloys were lower than the theoretical stress concentration factors. Furthermore, concerning the effect of notch geometry on the high cycle fatigue response of β-Ti-45Nb bulk alloy a decrease of fatigue notch sensitivity with decreasing notch radius was observed. This effect is explained by a reduction of stress concentration near the sharp notches due to presence of strain gradients as confirmed by FEA. Based on the fatigue experiments on smooth and notched samples, Ti-45Nb and L605 alloys were found to be full and moderate notch sensitive materials, respectively.

A part of the present study covered the high cycle fatigue behaviour of a commercial bulk L605 alloy. The fatigue studies can be supplemented by investigation of the effect of HPT deformation on the L605 material in comparison with the miniaturized Ti-45Nb specimens. Variation of the processing parameters of the HPT deformation may also lead to optimization of the fatigue performance of the investigated alloys. To improve the surface quality of miniaturized samples laser cutting with a subsequent electropolishing procedure can be used instead of electro discharge machining. Concerning the bulk L605 samples, future work can be conducted to investigate the effect of other surface finishing procedures (e.g. porous-coating and laser sintering) and residual stress on the fatigue strength.

References

[1] M. Delshadmanesh, G. Khatibi, M. Z. Z. Ghomsheh, M. Lederer, M. Zehetbauer, and H. Danninger, “Influence of microstructure on fatigue of biocompatible β-phase Ti-45Nb,” *Mater. Sci. Eng. A*, vol. 706, pp. 83–94, Oct. 2017.

[2] M. Delshadmanesh, G. Khatibi, M. Lederer, M. Zehetbauer, and H. Danninger, “Influence of Defects on High Cycle Fatigue Response of Ti45Nb Biocompatible Alloy,” *Solid State Phenom.*, vol. 258, pp. 337–340, Dec. 2017.

[3] J. W. Boretos and M. Eden, *Contemporary biomaterials : material and host response, clinical applications, new technology, and legal aspects*. Noyes Publications, 1984.

[4] T. M. Sridhar and S. Rajeswari, “Biomaterials Corrosion,” *Corros. Rev.*, vol. 27, no. Supplement, pp. 287–332, 2009.

[5] J. Y. Wong and J. D. Bronzino, *Biomaterials*. New York: CRC Press Taylor & Francis Group, 2007.

[6] T. Akahori, M. Niinomi, H. Fukui, M. Ogawa, and H. Toda, “Improvement in fatigue characteristics of newly developed beta type titanium alloy for biomedical applications by thermo-mechanical treatments,” *Mater. Sci. Eng. C*, vol. 25, no. 3, pp. 248–254, 2005.

[7] H. Yilmazer, M. Niinomi, M. Nakai, K. Cho, J. Hieda, Y. Todaka, and T. Miyazaki, “Mechanical properties of a medical β-type titanium alloy with specific microstructural evolution through high-pressure torsion,” *Mater. Sci. Eng. C*, vol. 33, no. 5, pp. 2499–2507, 2013.

[8] M. Niinomi, “Recent metallic materials for biomedical applications,” *Metall. Mater. Trans. A*, vol. 33, no. 3, pp. 477–486, 2002.

[9] D. Stoeckel, A. Pelton, and T. Duerig, “Self-expanding nitinol stents: material and design considerations,” *Eur. Radiol.*, vol. 14, no. 2, pp. 292–301, Feb. 2004.

[10] T. Duerig, A. Pelton, and D. Stöckel, “An overview of nitinol medical applications,” *Mater. Sci. Eng. A*, vol. 273–275, pp. 149–160, Dec. 1999.

[11] M. Syed, R. Chopra, and V. Sachdev, “Allergic reactions to dental materials-a systematic review,” *J. Clin. Diagnostic Res.*, vol. 9, no. 10, pp. ZE04-ZE09, 2015.

[12] Q. Chen and G. Thouas, *Biomaterials: a basic introduction*. CRC Press, 2014.

[13] V. dos Santos, R. N. Brandalise, and M. Savaris, *Engineering of Biomaterials*. Cham: Springer International Publishing, 2017.

[14] B. Ratner, A. Hoffman, F. Schoen, and J. Lemons, *Biomaterials science: an introduction to materials in medicine*. Elsevier, 2004.

[15] S. D. Cook and K. A. Thomas, “Fatigue failure of noncemented porous-coated implants. A retrieval study.,” *J. Bone Joint Surg. Br.*, vol. 73, no. 1, pp. 20–4, Jan. 1991.

[16] F. Zivic, S. Affatato, M. Trajanovic, M. Schnabelrauch, and N. Grujovic, *Biomaterials in clinical practice : advances in clinical research and medical devices*. Springer, 2017.

[17] G. Khatibi, M. Lederer, A. Betzwar Kotas, M. Frotscher, A. Krause, and S. Poehlmann, “High-cycle fatigue behavior of thin-walled CoCr tubes,” *Int. J. Fatigue*, vol. 80, no. February 2016, pp. 103–112, 2015.

[18] M. Papakyriacou, H. Mayer, C. Pypen, H. Plenk, and S. Stanzl-Tschegg, “Influence of loading frequency on high cycle fatigue properties of b . c . c . and h . c . p . metals,” *Mater. Sci. Eng. A*, vol. 308, no. 1–2, pp. 143–152, 2001.

[19] M. Niinomi, “Mechanical properties of biomedical titanium alloys,” *Mater. Sci. Eng. A*, vol. 243, no. 1–2, pp. 231–236, 1998.

[20] M. Janeček, F. Nový, P. Harcuba, J. Stráský, L. Trško, M. Mhaede, and L. Wagner, “The very high cycle fatigue behaviour of Ti-6Al-4V alloy,” *Acta Phys. Pol. A*, vol. 128, no. 4, pp. 497–502, 2015.

[21] C. C. Gomes, L. M. Moreira, V. J. S. V Santos, A. S. Ramos, J. P. Lyon, C. P. Soares, and F. V. Santos, “Assessment of the genetic risks of a metallic alloy used in medical implants,” *Genet. Mol. Biol.*, vol. 34, no. 1, pp. 116–121, 2011.

[22] C. Siemers, D. Wolter, and H. Sibum, “New, Aluminum- and Vandium-Free Titanium Alloys for Osteosynthesis Applications,” in *Proceedings of the 13th World Conference on Titanium*, Hoboken, NJ, USA: John Wiley & Sons, Inc., 2016, pp. 1665–1668.

[23] D. R. Sumner, T. M. Turner, R. Igloria, R. M. Urban, and J. O. Galante, “Functional adaptation and ingrowth of bone vary as a function of hip implant stiffness,” *J. Biomech.*, vol. 31, no. 10, pp. 909–917, 1998.

[24] M. Niinomi, “Low Modulus Titanium Alloys for Inhibiting Bone Atrophy,” *Biomater. Sci. Eng.*, Sep. 2011.

[25] Y. Song, D. S. Xu, R. Yang, D. Li, W. T. Wu, and Z. X. Guo, “Theoretical study of the effects of alloying elements on the strength and modulus of β-type bio-titanium alloys,” *Mater. Sci. Eng. A*, vol. 260, no. 1–2, pp. 269–274, 1999.

[26] R. Godley, D. Starosvetsky, and I. Gotman, “Corrosion behavior of a low modulus β -Ti-45 % Nb,” vol. 7, pp. 63–67, 2006.

[27] M. Niinomi, *Fatigue failure of metallic biomaterials*. Woodhead Publishing Limited,

2010.

[28] C.-W. Lin, C.-P. Ju, and J.-H. C. Lin, “Comparison among Mechanical Properties of Investment-Cast c.p. Ti, Ti-6Al-7Nb and Ti-15Mo-1Bi Alloys,” *Mater. Trans.*, vol. 45, no. 10, pp. 3028–3032, 2004.

[29] C. Schulze, M. Weinmann, C. Schweigel, O. Keßler, and R. Bader, “Mechanical properties of a newly additive manufactured implant material based on Ti-42Nb,” *Materials (Basel).*, vol. 11, no. 1, pp. 13–16, 2018.

[30] Y. Li, C. Yang, H. Zhao, S. Qu, X. Li, and Y. Li, “New developments of ti-based alloys for biomedical applications,” *Materials (Basel).*, vol. 7, no. 3, pp. 1709–1800, 2014.

[31] T. Ozaki, H. Matsumoto, S. Watanabe, and S. Hanada, “Beta Ti Alloys with Low Young ’ s Modulus,” vol. 45, no. 8, pp. 2776–2779, 2004.

[32] J. Sun, Q. Yao, H. Xing, and W. Y. Guo, “Elastic properties of β, α’’ and ω metastable phases in Ti–Nb alloy from first-principles,” *J. Phys. Condens. Matter*, vol. 19, no. 48, p. 486215, Dec. 2007.

[33] Y. Zhang, H. Liu, and Z. Jin, “Thermodynamic assessment of the Nb-Ti system,” *Calphad Comput. Coupling Phase Diagrams Thermochem.*, vol. 25, no. 2, pp. 305–317, 2001.

[34] V. G. Hatt, B.A. & Rivlin, “Phase transformations in superconducting Ti-Nb alloys,” *J. Phys. D. Appl. Phys.*, vol. 1, no. 9, pp. 1145–1149, 1968.

[35] S. S. Satheesh Kumar and T. Raghu, “Mechanical behaviour and microstructural evolution of constrained groove pressed nickel sheets,” *J. Mater. Process. Technol.*, vol. 213, no. 2, pp. 214–220, Feb. 2013.

[36] T. C. Lowe and R. Z. Valiev, *Investigations and Applications of Severe Plastic Deformation*. Springer Netherlands, 2000.

[37] S. Zherebtsov, E. Kudryavtsev, S. Kostjuchenko, S. Malysheva, and G. Salishchev, “Strength and ductility-related properties of ultrafine grained two-phase titanium alloy produced by warm multiaxial forging,” *Mater. Sci. Eng. A*, vol. 536, pp. 190–196, Feb. 2012.

[38] R. Z. Valiev and T. G. Langdon, “Principles of equal-channel angular pressing as a processing tool for grain refinement,” *Prog. Mater. Sci.*, vol. 51, no. 7, pp. 881–981, Sep. 2006.

[39] B. Z. Jiang, S. Emura, and K. Tsuchiya, “Microstructures and mechanical properties of Ti5553 alloy processed by high-pressure torsion,” *IOP Conf. Ser. Mater. Sci. Eng.*, vol. 63, no. 1, 2014.

[40] J. Jiang and A. Ma, “Bulk Ultrafine-Grained Magnesium Alloys by SPD Processing :

Technique , Microstructures and Properties," *Magnes. Alloy. - Des. Process. Prop.*, 2009.

[41] G. Khatibi, J. Horky, B. Weiss, and M. J. Zehetbauer, "High cycle fatigue behaviour of copper deformed by high pressure torsion," *Int. J. Fatigue*, vol. 32, no. 2, pp. 269–278, 2010.

[42] H. W. Höppel, M. Prell, L. May, and M. Göken, "Influence of grain size and precipitates on the fatigue lives and deformation mechanisms in the VHCF-regime," *Procedia Eng.*, vol. 2, no. 1, pp. 1025–1034, 2010.

[43] H. Mughrabi and H. W. Höppel, "Cyclic deformation and fatigue properties of very fine-grained metals and alloys," *Int. J. Fatigue*, vol. 32, no. 9, pp. 1413–1427, 2010.

[44] A. Vinogradov and S. Hashimoto, "Fatigue of severely deformed metals," *Adv. Eng. Mater.*, vol. 5, no. 5, pp. 351–358, 2003.

[45] R. V. Marrey, R. Burgermeister, R. B. Grishaber, and R. O. Ritchie, "Fatigue and life prediction for cobalt-chromium stents: A fracture mechanics analysis," *Biomaterials*, vol. 27, no. 9, pp. 1988–2000, 2006.

[46] C. A. Sweeney, B. OBrien, F. P. E. Dunne, P. E. McHugh, and S. B. Leen, "Micro-scale testing and micromechanical modelling for high cycle fatigue of CoCr stent material," *J. Mech. Behav. Biomed. Mater.*, vol. 46, pp. 244–260, 2015.

[47] L. Jiang, C. R. Brooks, P. K. Liaw, and D. L. Klarstrom, "High-Cycle Fatigue of ULTIMET Alloy," *Superalloys 2000*, no. May 2016, pp. 583–591, 2000.

[48] A. Mishra, M. Hamby, and W. Kaiser, "Metallurgy, Microstructure, Chemistry and Mechanical Properties of a New Grade of Cobalt-Chromium Alloy Before and After Porous-Coating," in *Cobalt-Base Alloys for Biomedical Applications*, ASTM International, 1999.

[49] and J. K. McEvily, Arthur J., *Metal Failures: Mechanisms, Analysis, Prevention*. John Wiley & Sons, 2013.

[50] S. Suresh, *Fatigue of Materials*. Cambridge University Press, 2004.

[51] B. S. A. Mitchell, *introduction to materials engineering and science for chemical and materials engineers*. John Wiley & Sons, 2004.

[52] W. J. W. Donald R. Askeland, Pradeep P. Fulay, *The Science and Engineering of Materials*, Sixth. 2011.

[53] S. L. Kakani, *Material science*. 2004.

[54] Y. Murakami, *Metal fatigue: effects of small defects and nonmetallic inclusions*. Elsevier, 2002.

[55] W. F. Hosford, *Mechanical behavior of materials*, vol. 12, no. 3. 2009.

[56] “Phase separation and second phase precipitation in beta titanium alloys.,” 2011.

[57] T. Dahlberg and A. Ekberg, *Failure , Fracture , Fatigue*. 2002.

[58] D. Roylance, “Mechanical Properties of Materials,” *Massachusetts Inst. Technol.*, vol. 51–78, p. 128, 2008.

[59] A. International, “Fatigue,” *Elem. Metall. Eng. Alloy.*, pp. 243–265, 2008.

[60] K. Fukuda, S. E. Straus, I. Hickie, M. C. Sharpe, J. G. Dobbins, and A. Komaroff, “The Chronic Fatigue Syndrome: A Comprehensive Approach to Its Definition and Study,” *Ann. Intern. Med.*, vol. 121, no. 12, p. 953, Dec. 1994.

[61] D. Hull and D. J. Bacon, *Introduction to Dislocations*. Elsevier Ltd, 2009.

[62] Hael Mughrabi, “Materials science and technology : a comprehensive treatment,” in *Materials Science and Technology*, no. 6, VCH, 1993, p. 697 p.

[63] H. Mughrabi, “Specific features and mechanisms of fatigue in the ultrahigh-cycle regime,” *Int. J. Fatigue*, vol. 28, no. 11, pp. 1501–1508, Nov. 2006.

[64] H. Mughrabi, “On ‘multi-stage’ fatigue life diagrams and the relevant life-controlling mechanisms in ultrahigh-cycle fatigue,” *Fract. Eng. Mater. Struct.*, vol. 25, no. 8–9, pp. 755–764, Sep. 2002.

[65] T. Sakai and H. Harada, “Crack initiation mechanism of bearing steel in very high cycle fatigue,” *Proceeding of ECF-16*, 2006.

[66] C. R. Sohar, A. Betzwar-Kotas, C. Gierl, B. Weiss, and H. Danninger, “Gigacycle fatigue behavior of a high chromium alloyed cold work tool steel,” *Int. J. Fatigue*, vol. 30, no. 7, pp. 1137–1149, Jul. 2008.

[67] C. R. Sohar, A. Betzwar-Kotas, C. Gierl, B. Weiss, and H. Danninger, “Fractographic evaluation of gigacycle fatigue crack nucleation and propagation of a high Cr alloyed cold work tool steel,” *Int. J. Fatigue*, vol. 30, no. 12, pp. 2191–2199, Dec. 2008.

[68] U. Of, “Chapter 2:,” pp. 1–18, 2009.

[69] A. Fatemi and N. Shamsaei, “Multiaxial Fatigue Modelling and Some Simple Approximations,” pp. 7–24, 2010.

[70] E. Storgärds, “High Temperature Fatigue Crack Growth in a Ni-based Superalloy Modelling Including the Interaction of Dwell Times,” no. 1681, p. 67, 2015.

[71] J. Schijve, *Fatigue of Structures andMaterials*. Springer, 2009.

[72] and D. J. B. Dieter, George Ellwood, *Mechanical metallurgy*, Vol. 3. New York: McGraw-hill, 1983.

[73] F. C. Campbell, *Fatigue and fracture: understanding the basics*. ASM International, 2012.

[74] C. Bathias, L. Drouillac, and P. Le François, “How and why the fatigue S–N curve does not approach a horizontal asymptote,” *Int. J. Fatigue*, vol. 23, pp. 143–151, 2001.

[75] H. Mughrabi, “Damage mechanisms and fatigue lives: From the low to the very high cycle regime,” *Procedia Eng.*, vol. 55, pp. 636–644, 2013.

[76] C. Shao, F. Lu, X. Wang, Y. Ding, and Z. Li, “Microstructure characterization and HCF fracture mode transition for modified 9Cr-1Mo dissimilarly welded joint at different elevated temperatures,” *J. Mater. Sci. Technol.*, vol. 33, no. 12, pp. 1610–1620, 2017.

[77] J. William D. Callister and David G. Rethwisch, “Materials science and engineering: An introduction,” *Mater. Des.*, p. 885, 2010.

[78] R. A. S. J. J. Xiong, *Fatigue and Fracture Reliability Engineering*. Springer, 2011.

[79] J. Roesler, H. Harders, and M. Baeker, *Mechanical Behavior of Engineering Materials*. 2006.

[80] B. S. Mitchell, *An Introduction To Materials Engineering and Science for Chemical and Materials Engineers*. John Wiley & Sons, 2004.

[81] G. Pluvinage, *Fracture and fatigue emanating from stress concentrators*. Springer Science & Business Media, 2007.

[82] P. Lukáš, L. Kunz, and M. Svoboda, “Fatigue notch sensitivity of ultrafine-grained copper,” *Mater. Sci. Eng. A*, vol. 391, no. 1–2, pp. 337–341, 2005.

[83] M. T. Ozkan, C. Eldem, and I. Sahin, “Determination of the notch factor for shafts under torsional stress with artificial neural networks,” *Mater. Tehnol.*, vol. 48, no. 1, pp. 81–90, 2014.

[84] H. Gleiter, *Nanostructured materials: basic concepts and microstructure*, vol. 48.1. Acta materialia, 2000.

[85] C. C. Koch, Ed., *Nanostructured Materials Processing, Properties, and Applications*, vol. 131, no. 2. William Andrew, 2007.

[86] K. Cho, L. Kecskes, R. Dowding, B. Schuster, Q. Wei, and R. Z. Valiev, “Nanocrystalline and Ultra-Fine Grained Tungsten for Kinetic Energy Penetrator and Warhead Liner Applications,” *Mater. Res.*, no. June, 2007.

[87] U. Bansal and M. Sharma, “Development of Mechanical Properties by Severe Plastic

Deformation Methods," vol. 2, no. 5, pp. 38–45, 2015.

[88] Sung H. Whang, *Nanostructured metals and alloys*. Philadelphia: Woodhead Publishing Limited, 2011.

[89] H. S. Nalwa, Ed., *Nanostructured Materials and Nanotechnology*. ACADEMIC PRESS, 2000.

[90] H. L. Yu and C. Lu, "Special rolling techniques for improvement of mechanical properties of ultrafine-grained metal sheets : a review," vol. 18, pp. 754–769, 2016.

[91] L. Tian, "A Short Review on Mechanical Behavior of Nanocrystalline Materials," no. February, 2018.

[92] D. D. Gill, P. Yang, A. C. Hall, T. J. Vogler, T. J. Roemer, D. Anthony, and C. J. Saldana, "Creating Bulk Nanocrystalline Metal," *Distribution*, pp. 1–92, 2008.

[93] R. Z. Valiev, Y. Estrin, Z. Horita, T. G. Langdon, M. J. Zehetbauer, and Y. T. Zhu, "Fundamentals of Superior Properties in Bulk NanoSPD Materials," *Mater. Res. Lett.*, vol. 4, no. 1, pp. 1–21, Jan. 2016.

[94] R. E. Smallman and A. H. W. Ngan, "Physical Metallurgy and Advanced Materials," *Vasa*, p. 650, 2008.

[95] H. Lim, M. G. Lee, J. H. Kim, B. L. Adams, and R. H. Wagoner, "Simulation of polycrystal deformation with grain and grain boundary effects," *Int. J. Plast.*, vol. 27, no. 9, pp. 1328–1354, 2011.

[96] K. Sülleiová, M. Besterci, and T. Kvačkaj, "Verification of Hall-Petch equation of nanocrystalline copper," *Metal*, vol. 19, no. 5, pp. 1–7, 2009.

[97] K. O. Sanusi, O. D. Makinde, and G. J. Oliver, "Equal channel angular pressing technique for the formation of ultra-fine grained structures," *S. Afr. J. Sci.*, vol. 108, no. 9–10, pp. 1–7, 2012.

[98] and G. J. O. Sanusi, K. O., K. O. Sanusi, and G. J. Oliver, "Effects of grain size on mechanical properties of nanostructured copper alloy by severe plastic deformation (SPD) process," *J. Eng. Des. Technol.*, vol. 7, no. 3, pp. 335–341, Oct. 2009.

[99] X. Sauvage, G. Wilde, S. Divinski, Z. Horita, R. Valiev, X. Sauvage, G. Wilde, S. Divinski, Z. Horita, and R. Valiev, "Grain boundaries in ultrafine grained materials processed by severe plastic deformation and related phenomena," *Mater. Sci. Eng. A, Elsevier*, vol. 540, p. 1, 2012.

[100] A. Moreira, J. Junior, and W. J. Botta, "Development of Ultrafine-Grained Metals by Equal-Channel Angular Pressing," no. May 2018, 2014.

[101] A. Pramono, *Investigation of Severe Plastic Deformation Processes for Aluminum Based Composites Faculty of Mechanical Engineering*. .

[102] N. S. De Vincentis, M. C. Avalos, A. M. Kliauga, V. L. Sordi, and R. E. Bolmaro, "Deformation analysis on F138 austenitic stainless steel: ECAE and rolling," vol. 112, no. 4, p. 2011, 2011.

[103] R. Z. Valiev, Y. Estrin, Z. Horita, T. G. Langdon, M. J. Zehetbauer, and Y. T. Zhu, "Producing bulk ultrafine grained materials by severe plastic deformation," *Jom*, vol. 58, no. 4, pp. 33–39, 2006.

[104] G. Raab, "The innovation potential of ECAP techniques of severe plastic deformation," *IOP Conf. Ser. Mater. Sci. Eng.*, vol. 63, no. 1, pp. 3–9, 2014.

[105] R. Z. Valiev, R. K. Islamgaliev, and I. V. Alexandrov, *Bulk nanostructured materials from severe plastic deformation*, vol. 45, no. 2. 2000.

[106] R. Z. Valiev, A. P. Zhilyaev, and T. G. Langdon, *Bulk Nanostructured Materials*. .

[107] A. Azushima, R. Kopp, A. Korhonen, D. Y. Yang, F. Micari, G. D. Lahoti, P. Groche, J. Yanagimoto, N. Tsuji, A. Rosochowski, and A. Yanagida, "Severe plastic deformation (SPD) processes for metals," *CIRP Ann. - Manuf. Technol.*, vol. 57, no. 2, pp. 716–735, 2008.

[108] A. P. Zhilyaev and T. G. Langdon, "Using high-pressure torsion for metal processing: Fundamentals and applications," *Prog. Mater. Sci.*, vol. 53, no. 6, pp. 893–979, Aug. 2008.

[109] C. Suryanarayana and M. G. Norton, *X-Ray Diffraction*. Boston, MA: Springer US, 1998.

[110] B. S. Prabhu, Y. T., Rao, K. V., Kumar, V. S. S., & Kumari, "X-Ray Analysis by Williamson-Hall and Size-Strain Plot Methods of ZnO Nanoparticles with Fuel Variation," *World J. Nano Sci. Eng.*, no. March, pp. 21–28, 2014.

[111] E. Schafler and M. Zehetbauer, "E. Schafler and M. Zehetbauer, 'Characterization of Nanostructured Materials By X-Ray Line Profile Analysis,'" *Rev. Adv. Mater. Sci*, vol. 10, pp. 28–33, 2005.

[112] G. W. and W. Hall, "X-ray line broadening from filed aluminium and wolfram," *Acta Metall.*, vol. 1, no. 1, pp. 22–31, 1953.

[113] G. Ribárik, T. Ungár, J. Gubicza, and IUCr, "MWP-fit: A program for multiple whole-profile fitting of diffraction peak profiles by ab initio theoretical functions," *J. Appl. Crystallogr.*, vol. 34, no. 5, pp. 669–676, Oct. 2001.

[114] J. Gubicza, G. Riba, T. Unga, T. Ungár, J. Gubicza, G. Ribárik, A. Borbély, and IUCr, "Crystallite size distribution and dislocation structure determined by diffraction profile

analysis : principles and practical application to cubic and hexagonal crystals research papers," *J. Appl. Crystallogr.*, vol. 34, no. 3, pp. 298–310, Jun. 2001.

[115] T. Ungár, L. Balogh, and G. Ribárik, "Twinning, dislocations and grain size in nanoSPD materials determined by X-ray diffraction." pp. 571–578, 2008.

[116] T. Ungár, G. Tichy, J. Gubicza, and R. J. Hellmig, "Correlation between subgrains and coherently scattering domains," *Powder Diffr.*, vol. 20, no. 04, pp. 366–375, Dec. 2005.

[117] T. Ungár and A. Borbély, "The effect of dislocation contrast on x-ray line broadening: A new approach to line profile analysis," *Appl. Phys. Lett.*, vol. 69, no. 21, p. 3173, Jun. 1998.

[118] W. C. Oliver and G. M. Pharr, "An improved technique for determining hardness and elastic modulus using load and displacement sensing indentation experiments," *J. Mater. Res.*, vol. 7, no. 06, pp. 1564–1583, Jun. 1992.

[119] I. Yamaguchi, "Speckle Displacement and Decorrelation in the Diffraction and Image Fields for Small Object Deformation," *Opt. Acta Int. J. Opt.*, vol. 28, no. 10, pp. 1359–1376, Oct. 1981.

[120] E. Schenuit, R. Bolkart, T. Becker, and O. Spinka, "Optical Strain Measurement on Small Specimens Based on Laser Speckles," *Mater. Sci. Forum*, vol. 584–586, pp. 237–242, Jun. 2008.

[121] R. Feiel and P. Wilksch, "High-resolution laser speckle correlation for displacement and strain measurement.," *Appl. Opt.*, vol. 39, no. 1, pp. 54–60, Jan. 2000.

[122] S. J. Kirkpatrick and D. D. Duncan, "Laser Speckle Strain Measurements in Soft Tissue," *SEM X Int. Congr. Expo. Exp. Appl. Mech.*, 2004.

[123] R. E. Smallman and A. H. W. Ngan, *Modern physical metallurgy*, 8th ed. Elsiver, 2014.

[124] M. Yovanovich, "Micro and Macro Hardness Measurements, Correlations, and Contact Models," *44th AIAA Aerosp. Sci. Meet. Exhib.*, no. January, pp. 1–28, 2006.

[125] J. C. Newman and R. S. Piascik, *Fatigue Crack Growth Thresholds, Endurance Limits, and Design*, vol. 15, no. 4. 2000.

[126] H. Mayer, "Fatigue crack growth and threshold measurements at very high frequencies," *Int. Mater. Rev.*, vol. 44, no. 1, p. 1–34., 1999.

[127] W. D. Pilkey, D. F. Pilkey, and R. E. Peterson, *Peterson's stress concentration factors*. John Wiley, 2008.

[128] Y. Weixing, "Stress field intensity approach for predicting fatigue life," *Int. J. Fatigue*, vol. 15, no. 3, pp. 243–246, May 1993.

[129] P. Grad, B. Reuscher, A. Brodyanski, M. Kopnarski, and E. Kerscher, "Mechanism of fatigue crack initiation and propagation in the very high cycle fatigue regime of high-strength steels," *Scr. Mater.*, vol. 67, no. 10, pp. 838–841, Nov. 2012.

[130] K. Dai and L. Shaw, "Analysis of fatigue resistance improvements via surface severe plastic deformation," *Int. J. Fatigue*, vol. 30, no. 8, pp. 1398–1408, Aug. 2008.

[131] M. J. I.P. Semenova, S.A. Gatina, V.S. Zhernakov, *Proceedings of the 13th World Conference on Titanium*. John Wiley & Sons, Inc., 2016.

[132] R. B. Figueiredo, E. R. de C. Barbosa, X. Zhao, X. Yang, X. Liu, P. R. Cetlin, and T. G. Langdon, "Improving the fatigue behavior of dental implants through processing commercial purity titanium by equal-channel angular pressing," *Mater. Sci. Eng. A*, vol. 619, pp. 312–318, Dec. 2014.

[133] M. Launey, S. W. Robertson, L. Vien, K. Senthilnathan, P. Chintapalli, and A. R. Pelton, "Influence of microstructural purity on the bending fatigue behavior of VAR-melted superelastic Nitinol," *J. Mech. Behav. Biomed. Mater.*, vol. 34, pp. 181–186, Jun. 2014.

[134] H.W. Höppel, "Mechanical Properties of Ultrafine Grained Metals under Cyclic and Monotonic Loads: An Overview," *Mater. Sci. Forum*, vol. 503–504, pp. 259–266, 2006.

[135] C. Z. Xu, Q. J. Wang, M. S. Zheng, J. W. Zhu, J. D. Li, M. Q. Huang, Q. M. Jia, and Z. Z. Du, "Microstructure and properties of ultra-fine grain Cu–Cr alloy prepared by equal-channel angular pressing," *Mater. Sci. Eng. A*, vol. 459, no. 1–2, pp. 303–308, Jun. 2007.

[136] A. Vinogradov, "Fatigue limit and crack growth in ultra-fine grain metals produced by severe plastic deformation," *J. Mater. Sci.*, vol. 42, no. 5, pp. 1797–1808, Mar. 2007.

[137] K. Hockauf, T. Niendorf, S. Wagner, T. Halle, and L. W. Meyer, "Cyclic behavior and microstructural stability of ultrafine-grained AA6060 under strain-controlled fatigue," *Procedia Eng.*, vol. 2, no. 1, pp. 2199–2208, Apr. 2010.

[138] R. H. Li, Z. J. Zhang, P. Zhang, and Z. F. Zhang, "Improved fatigue properties of ultrafine-grained copper under cyclic torsion loading," *Acta Mater.*, vol. 61, no. 15, pp. 5857–5868, Sep. 2013.

[139] I.-C. Choi, B.-G. Yoo, O. Kraft, R. Schwaiger, M.-Y. Seok, M. Kawasaki, T. G. Langdon, and J. Jang, "High-cycle fatigue behavior of Zn–22% Al alloy processed by high-pressure torsion," *Mater. Sci. Eng. A*, vol. 618, pp. 37–40, Nov. 2014.

[140] and R. G. B. Young, Warren Clarence, *Roark's formulas for stress and strain.* New York: McGraw-Hill, 2002.

[141] K. Yang, Y. Ivanisenko, A. Caron, A. Chuvilin, L. Kurmanaeva, T. Scherer, R. Z. Valiev, and H.-J. Fecht, "Mechanical behaviour and in situ observation of shear bands in ultrafine

grained Pd and Pd–Ag alloys,” *Acta Mater.*, vol. 58, no. 3, pp. 967–978, Feb. 2010.

[142] L. Kunz, “Mechanical Properties of Copper Processed by Severe Plastic Deformation,” in *Copper Alloys - Early Applications and Current Performance - Enhancing Processes*, InTech, 2012.

[143] I. Sabirov, Y. Estrin, M. R. Barnett, I. Timokhina, and P. D. Hodgson, “Tensile deformation of an ultrafine-grained aluminium alloy: Micro shear banding and grain boundary sliding,” *Acta Mater.*, vol. 56, no. 10, pp. 2223–2230, Jun. 2008.

[144] D. Taylor, “Geometrical effects in fatigue: a unifying theoretical model,” *Int. J. Fatigue*, vol. 21, no. 5, pp. 413–420, May 1999.

[145] W. D. Pilkey and D. F. Pilkey, *Peterson’S Stress Concentration Factors*. John Wiley & Sons, Inc., 2008.

[146] M. Lederer and G. Khatibi, “On the relation between the energy of a distorted crystal lattice and the bending modulus of strain gradient elasticity,” *J. Phys. Conf. Ser.*, vol. 790, no. 1, p. 012019, Jan. 2017.

[147] P. P. Bathias C, Field D, Antolovich S, “Microplasticity, microdamage, microcracking in ultrasonic fatigue,” in *Int. Conf. on Fract. ICF 13*, 2013, pp. M04-03.

[148] M. Goto, T. Yamamoto, H. Nisitani, T. Sakai, and N. Kawagoishi, “Effect of grinding on the fatigue strength of a bearing steel in the the super long-life field,” *Thirteen. Eur. Conf. Fatigue*, 2000.

[149] C. R. Sohar, A. Betzwar-Kotas, C. Gierl, B. Weiss, and H. Danninger, “Influence of surface residual stresses on gigacycle fatigue response of high chromium cold work tool steel,” *Materwiss. Werksttech.*, vol. 39, no. 3, pp. 248–257, Mar. 2008.

List of abbreviations

CRSS	Critical resolved shear stress
FWHM	Full width at half maximum
MWH	Modified Williamson-Hall
MXPA	Multireflection X-ray profile analysis
WAXS	Wide angle X-ray scattering
WH	Williamson-Hall
XLPA	X-ray Line profile analysis
SPD	Severe plastic deformation
UFG	Ultrafine-grained
CG	Conventional grained
HPT	High pressure torsion
EDM	Electro discharge machining
RT	Room temperature
EP	Electropolishing
LCF	Low cycle fatigue
HCF	High cycle fatigue
VHCF	Very high cycle fatigue
ECAP	Equal-channel angular pressing
ARB	Accumulative rolling bonding
HE	Hydrostatic extrusion
CEC	Cyclic extrusion compression
RCS	Repetitive corrugation and straightening
HHE	Hot hydrostatic extruded

CCDF	Cyclic closed-die forging
SSMR	Super short multi-pass rolling
CMWP	Convolutional multiple whole profile
EBSD	Electron backscatter diffraction
SEM	Scanning electron microscopes
TEM	Transmission electron microscopy
XRD	X-ray diffraction

List of symbols

T	Temperature
σ_y	Yield stress
G	Shear modulus
τ_{max}	Maximum shear stress
f_t	Tabor factor
τ_r	Resolved shear stress
τ_{CRSS}	Critical resolved shear stress
ε_m	Mean strain
ε_{max}	Maximum strain
λ	Wavelength
σ_m	Mean stress
σ_{max}	Maximum stress
σ_{min}	Minimum stress
R	Stress ratio
K_t	Theoretical stress concentration factor
σ_y	Yield strength
σ_{UTS}	Ultimate tensile strength
σ	Applied stress
ρ	Dislocation density
f_S	Schmid factor
E	Young’s modulus
ν	Poisson’s ratio
F	Force
H	Indentation hardness

List of figures

List of tables

Acknowledgments

I would like to express my sincere and deepest gratitude to my supervisors Dr. Golta Khatibi, Research Group of Mechanical Response of Materials, Institute of Chemical Technologies and Analytics, Faculty of Technical Chemistry, Vienna University of Technology, for her continuous help and valuable comments and suggestions for this study and fruitful discussion on the interpretations of the results and Prof. Herbert Danninger, Research Group of Powder Metallurgy Institute of Chemical Technologies and Analytics, Faculty of Technical Chemistry, Vienna University of Technology, for his constant encouragement and kind support as well Prof. Michael Zehetbauer, Physics of Nanostructured Materials, Faculty of Physics, University of Vienna, for his support in many aspects of this thesis.

I am extremely thankful to Dr. Martin Lederer, Research Group of Mechanical Response of Materials, Institute of Chemical Technologies and Analytics, Faculty of Technical Chemistry, Vienna University of Technology, which part of the thesis was carried out in a close collaboration with him to do FEM analysis.

I would like to thank Prof. Erhard Schafler, Physics of Nanostructured Materials, Faculty of Physics, University of Vienna, for his help concerning the X-ray experiments.

I wish to express my cordial gratitude to Mr. Ahmad Hashemi, Institute of Chemical Technologies and Analytics, Faculty of Technical Chemistry, Vienna University of Technology, who helped me how to work with SEM microscopy.

I would like to acknowledge all members of the research group of Mechanical Response of Materials.

Most importantly I would like to thank my family, my parents and my husband Mohammad for their support and love in all situations. Without their encouragement, I would not have finished this thesis. I would like to extend my warmest thanks to my dear son, Adrian.